Device and Dielectric Engineering for Low Voltage Polymer Transistors

A Thesis Submitted in Partial Fulfillment for the Requirement of the degree of

Doctor of Philosophy

by

Swathi

Chemistry and Physics of Materials Unit,
Jawaharlal Nehru Centre for Advanced Scientific Research
(A Deemed University)
Bangalore - 560 064
India.

MARCH 2018

Dedication

To Pati whom I idolized for her dedication towards work

To Thatha who showed me perseverance by example

To Mama who always guided me to be steadfast

To Mummy who instilled hope in me everyday

To Sai, my guiding light

Declaration

I hereby declare that the matter embodied in the thesis entitled "***Device and Dielectric Engineering for Low Voltage Polymer Transistors***" is the result of investigations carried out by me at the Chemistry and Physics of Materials Unit, Jawaharlal Nehru Centre for Advanced Scientific Research, Bangalore, India under the supervision of Prof. K. S. Narayan and that it has not been submitted elsewhere for the award of any degree or diploma.

In keeping with the general practice in reporting scientific observations, due acknowledgment has been made wherever the work described is based on the findings of other investigators.

Swathi

JAWAHARLAL NEHRU CENTRE FOR ADVANCED SCIENTIFIC RESEARCH
Jakkur, Bangalore 560064, India

K. S. NARAYAN
Professor and Dean (R&D)
PHONE: 91 80 22082822
FAX: 91 80 22082766
e-mail: narayan@jncasr.ac.in URL: www.jncasr.ac.in/narayan

March 23rd, 2018

Certificate

I hereby certify that the matter embodied in this thesis entitled "***Device and Dielectric Engineering for Low Voltage Polymer Transistors***" has been carried out by Ms. Swathi at the Chemistry and Physics of Materials Unit, Jawaharlal Nehru Centre for Advanced Scientific Research, Bangalore, India under my supervision and that it has not been submitted elsewhere for the award of any degree or diploma.

Prof. K. S. Narayan
(Research Supervisor)

Acknowledgements

An endeavor such as research cannot be achieved by lone effort. Several wonderful people have contributed in many different perspectives towards this piece of research which is documented as this thesis. I take this opportunity to express my sincere gratitude to all these people for their support and encouragement.

I will remain forever grateful to Prof. K. S. Narayan, my research supervisor, for introducing me to the field of Organic Electronics when I came as a summer intern to JNCASR. Prof. Narayan has a keen eye for detail which combined with his analytical approach left me positively enriched after every discussion. I received a lot of encouragement to think individually and was given complete freedom to implement my ideas. I honestly cannot envision a better intellectually stimulating atmosphere compared to the one he created for me. During the last six years, Narayan sir has played a pivotal role in my growth, both personally and professionally and I thank him for the sort of individual I have developed into.

I am thankful to the JNC faculty: Dr, Ranjani Vishwanatha, Dr. T Govindraju Dr. Sundaresan and Dr. Subi George, for openness in discussion and their friendly attitude where I learnt a lot of interesting science. I also acknowledge their students for enriching collaborations which taught me various aspects of materials chemistry.

I am thankful to all my collaborators Dr. Satish Patil, IISc Bangalore, Asha S. K., NCL Pune and Dr. Sanjayan, NCL Pune for all the help in terms of new materials and wonderful scientific discussions which greatly enhanced my knowledge in the field of organic electronics.

My special thanks to Dr. Vipul Singh who hosted me in IIT Indore for Silvaco training. His students require special mention as they went out of their way to make me feel at home and ensured that I had a pleasant stay in Indore.

The courses I studied in my first year has helped me throughout my research in some form or the other. I thank all the faculty members in CPMU and TSU for their

wonderful teaching. My special thanks to Prof. Balasubramanian Sundaram and Prof. S. M. Shivaprasad for all the things I learnt.

I feel very honored and thankful to share the same intellectual environment as Prof. C. N. R Rao. His lectures and words of encouragement have inspired my research outlook throughout my stay here.

I would like to acknowledge Department of Science and Technology for the funding support in terms of fellowships and a travel grant.

JNC has been a very fulfilling experience on all fronts and I have made some excellent friends while here. This list is far from comprehensive but I have had the best times with some of them. I thank my lab seniors: Manohar, Monojit, Sabyasachi, Anshuman, Poonam, Kishore, Murthy, Vini, Satya, Ravi, Prashant and Suman. Going to be Drs. Ashar, Krishna, Nisha, Raaghesh, Rishav, Ganesh, Deepak, Anaranya, Sumukh, Azeez and Sukanya. Special thanks to Sumukh and Anaranya who always helped in my experiments when I had to meet deadlines.

I will always cherish the time spent with Manoj, whose enthusiasm and inquisitiveness I found quite contagious. Sharing opinions and arguments with him has made my outlook more comprehensive and positive. To complete my pillars of friendly support are Susheela and Shashi who were there always to help me and share my joys and sorrows. These three listened to me patiently for hours and left me feeling more positive and happy every time.

I thank all my teachers from my school and college days who are wonderful physicists and have played a key role in my choice for research. Special thanks to Shastri sir who got me excited about research and showed me the means to pursue it.

I will always cherish the time I spent outdoors in the evenings playing volleyball, badminton and doing yoga. Those one and half hours were truly stress busting and all the team members made me more confident, competitive and happy.

My spiritual mentor, Sri Sathya Sai Baba, has played a key role in the sort of individual I have grown up to become. His message of the five human values; Truth,

Righteous Conduct, Peace, Love and Non-Violence continue to guide my personal decisions. I thank him with utmost gratitude for my upbringing.

Last but not the least I can never complete my story without thanking my girls who have shared my life from childhood. Nishita, Kala, Sai Shree, Sai Latha and Smriti have been family outside my home and I will forever be thankful to them for making everyday living so lively.

Finally, I am ever grateful to my mother, uncles and grandparents for having filled my life with inexpressible joy and happiness. Having such a close-knit and loving family is the greatest blessing I have been bestowed with.

Swathi

JNCASR, Bangalore

Synopsis

Organic electronic devices offer several advantages in terms of device fabrication, scalability and cost. Organic light-emitting diodes (OLEDs) and organic photodiodes (OPDs) which have already carved a niche in mainstream electronics need driver circuits preferably consisting of organic/polymer field-effect transistors (PFETs) for integrated circuit applications. Consequently, PFETs must have low turn-on voltage, operate at high speed and must be scalable. This thesis addresses some of these PFET requirements by a) dielectric engineering to obtain ultra-thin organic/organic-inorganic hybrids with low turn-on voltage, which is then utilized in conjunction with a solution processed photodiode b) composites of organic dielectrics for low leakage PFETs and c) studying an alternate, scalable 3D vertical transistor architecture to reduce the channel length, increase the device density and improve switching speed.

The section on dielectric engineering is structured in three parts. In the first part of the studies, techniques for forming a self-assembled monolayer (SAM) of a surfactant on a high k oxide layer are used to obtain ultra-thin, pin-hole free dielectrics with d $<$ 10 nm and high specific capacitance of 0.3 $\mu F/cm^2$. PFETs fabricated using this hybrid dielectric operate at -2 V and demonstrate a p-type mobility of 0.35 $cm^2/V.s$.

In the second part, a new molecular dielectric 4,5,6,7-tetrabromo-2-(2,5-di-tert-butylphenyl)isoindoline-1,3-dione (TBD) is utilized as a single step, solution processable dielectric layer for PFETs. The dielectric properties of a thin film of TBD reveal a low loss tangent and a very small dipolar relaxation time. PFETs fabricated using TBD as the dielectric and a low bandgap p-type polymer operate in saturation at -5 V with a mobility of 0.1 $cm^2/V.s$ and a near-zero threshold voltage which implies low interfacial disorder.

The small size and high polarizability of TBD also makes it favorable as an additive in a semi-crystalline ferroelectric polymer matrix of poly[(vinylidenefluoride-co-trifluoroethylene] P(VDF:TrFE). AFM morphology and capacitance measurements suggest closer chain packing resulting in larger oriented ferroelectric regions thereby

resulting in increased P(E) magnitude as compared to the pristine P(VDF-TrFE) film. Temperature dependent dielectric spectroscopy of the composite reveals signatures of TBD and P(VDF-TrFE) relaxations giving rise to a frequency and temperature dependent relaxation generally seen in relaxor ferroelectric films. PFETs fabricated from the composite dielectric yield an order of magnitude higher mobility over pristine PVDF devices suggesting lower interfacial disorder due to better lamellar packing in the dielectric film.

In the next section, a PFET using the oxide-SAM hybrid dielectric is integrated with an OPD as a pixel addressable optical sensor. The integrated PFET-OPD structure demonstrates a reasonable light dependence of up to four orders of incident power and a minimum sensitivity of 10 $\mu W/cm^2$. Thickness variations of the OPD in the integrated structure is studied to optimize the linear dynamic range of the sensor. Secondly, a monolithic structure of the two components is also fabricated.

The final section addresses the capability of organic transistors to be used in high density and high-speed circuits. A vertical organic transistor configuration is realized using a porous alumina membrane as a template to demonstrate massively parallel organization (10^9 transistors/mm^2) of connected three-terminal devices called the organic nano-triode array. Charge transport in this device is governed by space charge limited current which is modulated by a porous, sandwiched base (similar to gate) electrode to give transistor-like characteristics. The response characteristics of this novel structure are studied to indicate the key parameters involved in the underlying mechanism. Device operation at single transistor level is verified by conductive atomic force microscopy, and the inherent short switching time scales of the vertical transistor is also demonstrated.

Charge transport models such as Poole-Frenkel behavior, Langevin recombination and defect models are introduced in a 2-D simulation procedure to observe the relation of material specific characteristics with the output current of the integrated PFET-OPD structure and the organic nano-triode array. Based on the output, additional parameters which affect the device performance such as device

dimensions, trap density and the electrode-semiconductor interfaces have been studied to predict figure of merit parameters for fabricating devices with optimal performance.

The combination of experimental and simulation approaches to improve solution processable transistor characteristics provides a possible route to implement organic devices for variety of applications.

List of Publications

- **Swathi, K**., Vajjiravel Murugesan and Narayan, K. S., Solution Processed Molecular Dielectric and Ferroelectric-Molecule Blends for Polymer Field-Effect Transistors. *Manuscript Under Preparation.*

- **Swathi, K**. and Narayan, K. S., 2017. Self-Assembled Porous Alumina Based Organic Nanotriode Arrays. *Nano letters*, 17(12), pp.7945-7950.

- **Swathi, K**. and Narayan, K. S., 2016. Image pixel device using integrated organic electronic components. *Applied Physics Letters*, *109*(19), p.193302.

- **Swathi, K**. and Narayan, K. S., 2016, September. Solution processed integrated pixel element for an imaging device. In *Organic Sensors and Bioelectronics IX* (Vol. 9944, p. 99440T). International Society for Optics and Photonics.

- Shivakumar, K. I., **Swathi, K**., Patil, G., Das, T., Kumar, A., Makde, R., Vanka, K., Babu, S. S., Narayan, K. S. and Sanjayan, G. J., 2017, Mixed-Stack Charge Transfer Crystals of Pillar [5] quinone and Tetrathiafulvalene Exhibiting Ferroelectric Features. *Chemistry-A European Journal*, 10.1002/chem.201702577.

- Vijayan, R., **Swathi, K**. and Narayan, K. S., 2016. Synergistic Effects of Electric-Field-Assisted Annealing and Thermal Annealing in Bulk-Heterojunction Solar Cells. *ACS Applied Materials & Interfaces*, 9(23), pp.19436-19445.

- Avinash, M.B., **Swathi, K**., Narayan, K. S. and Govindaraju, T., 2016. Molecular architectonics of naphthalenediimides for efficient structure–property correlation. *ACS Applied Materials & Interfaces*, 8(13), pp.8678-8685.

- Dhar, J., **Swathi, K**., Karothu, D. P., Narayan, K. S. and Patil, S., 2014. Modulation of Electronic and Self-Assembly Properties of a Donor–Acceptor–Donor-Based Molecular Materials via Atomistic Approach. *ACS Applied Materials & Interfaces*, 7(1), pp.670-681.

- Grandhi, G. K., **Swathi, K**., Narayan, K. S. and Viswanatha, R., 2014. Cu doping in ligand free CdS nanocrystals: conductivity and electronic structure study. *The Journal of Physical Chemistry Letters*, 5(13), pp.2382-2389.

Conference Presentations

- Oral Presentation – 2015, *11th JNC Chemistry of Materials Conference*, Alleppy, Kerala
- Poster Presentation – Solution Processed Integrated Pixel Element for an Imaging Device. 2016, *SPIE International Symposium on Organic Electronics + Photonics,* San Diego, California
- Oral Presentation - Solution Processed Integrated Pixel for an Imaging Device. 2016, *In House Symposium*, JNCASR, Bangalore
- Oral Presentation - TCAD in Organic Electronics. 2017, *Synopsys University Connect*, Bangalore

In the News

- Super-packed organic transistors for flexible devices, 2017. *The Hindu.* http://www.thehindu.com/sci-tech/science/jncasr-super-packed-organic-transistors-for-flexible-devices/article21379987.ece

Table of Contents

Chapter 2: Device Simulations-Theory

Chapter 3: Solution Processable Ultra-Thin Dielectrics

Chapter 5: Porous Alumina Based Organic Nano-Triode Arrays

Chapter 6: Summary and Outlook

Appendices

List of Abbreviations

PFET	Polymer Field Effect Transistor
OPD	Organic Photodiode
HOMO	Highest Occupied Molecular Orbital
LUMO	Lowest Unoccupied Molecular Orbital
BHJ	Bulk Hetero Junction
EQE	External Quantum Efficiency
PVD	Physical Vapor Deposition
AFM	Atomic Force Microscopy
PFM	Piezo-response Force Microscopy
OPA	Octadecyl Phosphonic Acid
SAM	Self-Assembled Monolayer
CMOS	Complementary Metal Oxide Semiconductor
XRD	X-ray Diffraction
DMF	Dimethyl Formamide
MIM	Metal-Insulator-Metal
PPS	Passive Pixel Sensor
ONTA	Organic Nano Triode Array
SCLC	Space Charge Limited Current

Introduction

Chapter 1

1.1 Organic electronics: Overview

Research and development in organic electronics has risen dramatically since the observation of conductivity in doped polyacetylene as shown by Shirakawa, McDiarmid and Alan. J. Heeger[1,2]. Over the last few decades, it has been a vibrant field of research and development encompassing chemistry, physics, materials engineering and even biology. At the core of this field is the interesting interplay of the π-electronic structure in conjugated carbon chains with their chemical nature which has led to the realization of fascinating electronic devices such as organic light-emitting diodes[3], organic field effect transistors[4] and organic solar cells[5].

Organic semiconductors benefit from their ability to be processed from a solution phase at relatively low temperatures in the form of layers/thin films for electronic devices[6]. The ability to deposit organic semiconductors using conventional printing methods has also attracted interest in them. Organic electronic devices are not designed to replace conventional silicon-based technology, but can offer complementary manufacturing and form-factor options to suit applications where the use of silicon is not possible. Two demonstrated examples of such applications are large area displays based on organic light emitting diodes (OLEDs) like LG's 77-inch Ultra HD curved OLED TV[7] and flexible electronic skin meshed with embedded sensors and actuators[8].

This chapter gives a brief introduction to the nature of organic semiconductors and fundamental topics of material and device characteristics which are used to realize novel and complex device architectures for integrated electronics. The choice of topics introduced are particularly relevant to the results and discussions in the following chapters.

1.2 Organic Semiconductors

Organic semiconductors comprise a class of carbon-based molecules and polymers with alternating double bonds. Of prime importance to the performance of organic

semiconductors is their property of π-conjugation which characterizes these materials. They are essentially formed by carbon atoms which are sp^2-hybridized having the sp^2-orbitals in a trigonal planar configuration with the pz-orbitals perpendicular to the plane. Such a configuration forms a conjugated system with delocalized π-electrons due to resonating alternate double (σ + π) and single bonds (σ) in the molecule. The conjugation planarizes the molecule, which allows delocalization of π/π*-states over many carbon atoms. The symmetric (π) configuration is stabilized by significant electron density present between neighboring carbon atoms as opposed to the anti-symmetric (π*) one. Consider a simple two-carbon system. From molecular orbital theory, the two unpaired $2p_z$ electrons occupy the two spin-allowed π states as it is a stable configuration, leaving the π* states unoccupied above a forbidden energy gap E_g: the difference between the highest occupied molecular orbital (HOMO) and lowest unoccupied molecular orbital (LUMO) which is analogous to the bandgap in a crystalline material. sp^2-hybridised molecules can therefore act as semiconductors and the HOMO and LUMO levels are but the bonding and anti-bonding orbitals of the π-conjugated cloud. The scheme of molecular orbital formation is shown in Figure 1.1.

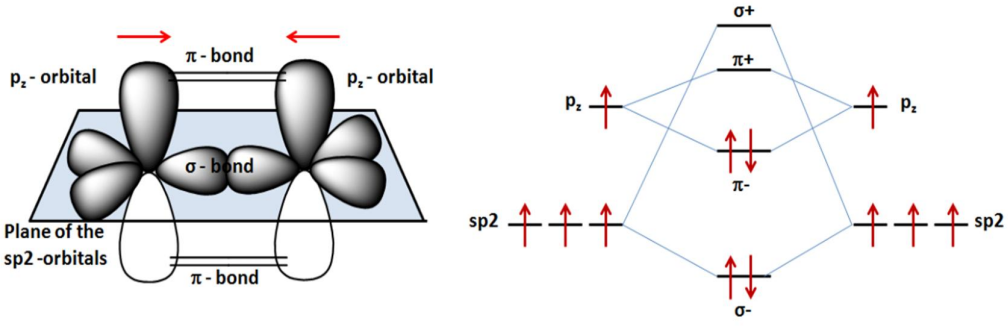

Figure 1.1: Molecular bond and orbital formation scheme in conjugated systems.

Although the bonds along the polymer chain are covalent, multiple chains are linked only by weak Van der Waal's forces. As a result, three-dimensional long-range order is seldom observed although they can be crystalline over a short range (semi-crystalline polymers). This categorizes polymer semiconductors as disordered materials and any perturbation along the conjugation of the polymer backbone

changes the HOMO and LUMO levels locally. Localization of states due to this disorder generates a set of energy levels (as opposed to a continuum in inorganic semiconductors) close enough to each other and tailing into the bandgap energies (trap sites) to facilitate charge carrier hopping between them at ambient temperatures.

Various approaches have been suggested to explain the hopping nature of charge transport in polymeric materials. These transport models can be classified as microscopic transport models which consider atomic levels with first principle modeling and the macroscopic transport models where the device parameters can be directly mapped.

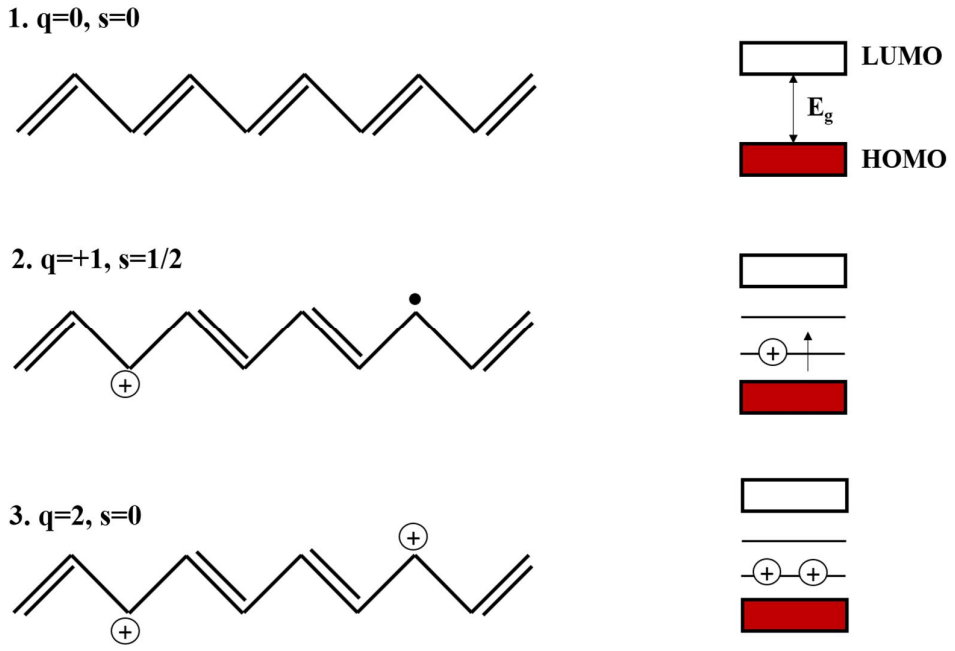

Figure 1.2: Types of polarons along with their spin state and charge

The widely accepted microscopic model is based on the motion of charges through trap sites with the assistance of the molecular distortion (phonon) within the conjugated framework[1,2,9,10]. When the electronic transfer energy is small, a localized charge carrier can cause a significant displacement of its surrounding atoms from their equilibrium positions. The displacement of the surrounding atoms creates a potential well in which the localized charge carrier gets 'self-trapped'. Such a composite quasiparticle self-trapped charge carrier when taken together with the polarization

cloud that its presence induces on its surrounding can be defined as a polaron[11-13]. The strength of the electron-phonon coupling decides the radius of the polaron and the activation energy required for the charge to hop. The presence of polarons creates additional levels symmetrical to the Fermi level. Typical energy levels and types of polarons are shown in Figure 1.2. The location of the energy levels is dependent on the length of the polymer chain and the transition between the polaronic levels is governed by selection rules which require parity transformation. Polarons were first modeled by Holstein in a simplistic 1D molecular crystal[14] and the presence of polarons is evident from experiments involving electron spin resonance and transient absorption[15,16].

1.2.1 p-type Semiconductors

1.2.1.1 P3HT

P3HT belongs to the group of alkyl-substituted poly-thiophene, commonly known as poly(3-alkyl-thiophene) (P3AT) which has been a model system for polymer electronics. The chemical structure of P3HT is shown in Figure 1.3. Based on the position of the alkyl chains in consecutive thiophene units, the polymer chains can be categorized into different conformations: head-to-head (HH) or head-to-tail (HT) or tail-to-tail (TT) combinations which yield different conjugation lengths and hence charge transport properties[17]. Poly alkyl thiophenes can also be categorized as regio-random polymers which have randomly distributed conformations and regio-regular polymers containing only one of the conformations. Typically, field-effect transistor (FET) mobility (μ_{FET}) increases with increase in the degree of regio-regularity which is highly desired and falls by orders of magnitude for regio-random films[18,19]. The HOMO level of P3HT being -5.2 eV w.r.t the vacuum level gives it a p-type character for an active layer material in FETs. It has a bandgap of 2.1 eV, making it a visible-range absorber (~300-600 nm) and is widely used as a donor material for photovoltaic and photoconductive device applications.

1.2.1.2 PBDTTT-C-T

The commercially available benzodithiophene co-polymer with thienothiophene polymer known as poly[4,8-bis-(2-ethylhexyloxy)-benzo[1,2-b:4,5-b']dithiophene-2,6-diyl-alt-4-(2-ethylhexyloxy-1-one)thieno[3,4-b]thiophene-2-yl)-2-ethylhexan-1-one] (PBDTTT-C-T)[20] is used extensively as a low bandgap p-type amorphous semiconductor for bulk heterojunction (BHJ) based photodiodes (Figure 1.3). The low bandgap is achieved by donor-acceptor co-polymerization for better solar spectral matching. In the donor-acceptor co-polymer approach, the electron-rich monomers and electron-deficient monomers are fused alternately along the backbone of the polymer. The quinodal form is stabilized along the alternating structure of monomers due to the charge-separated resonance structure. This approach offers to tune individually the HOMO and LUMO level of the polymer because of their different locations on the polymer-backbone. It was shown that, the LUMO level is observed to be exclusively on the acceptor unit whereas the HOMO level is more delocalized but predominantly observed on the donor unit[21]. The bandgap of PBDTTT-C-T is measured to be ~ 1.58 eV and its absorption extends to the near infrared region (~800 nm) making it a highly desirable material for photovoltaic and photoconductive devices.

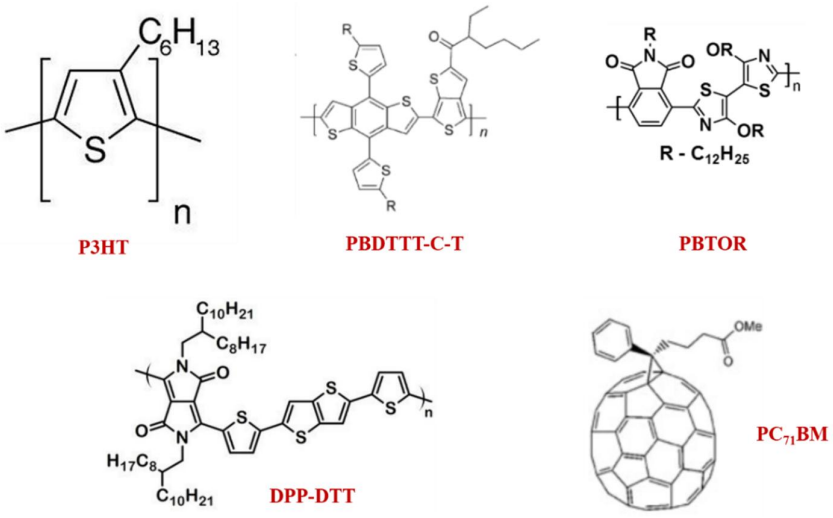

Figure 1.3: Chemical structures of semiconducting p-type polymers and n-type $PC_{71}BM$ used in this thesis.

1.2.1.3 PBTOR

Polymer chain conjugation length and co-planarity plays a critical role in enhancing the charge transport properties[22]. One of the strategies to enhance the co-planarity of the conjugated core is by using secondary forces like Van der Waals interactions to obtain a rigid structure[23]. Understanding these effects, the polymer with repeat unit 4,4'-dialkoxy-5,5'-bithiazole (BtzOR) is designed. This polymer takes advantage of secondary forces like the S(thiazolyl)···O(alkoxy) originating from the intramolecular interactions to obtain extended π-π conjugation and high crystallinity. XRD measurements performed on the polymer films demonstrate lamellar packing with diffraction pattern corresponding to the backbone length and π–π stacking. The higher degree of crystallinity can also be attributed to the backbone co-planarity induced by the C–H···H–C repulsions between the phthalimide and thiazole units (Figure 1.3) which ultimately enhances carrier mobility[23]. Typical absorption spectrum of the polymer indicates a broad absorption throughout the visible region with optical band-gap of 1.6 eV. PBTOR was procured from Polyera ActivInk Inc. and its unique chain arrangement enables high mobility (up to 2 $cm^2/V.s$) in an FET device[24].

1.2.1.4 DPP-DTT

Diketopyrrolo-pyrrole-dithiophene-thienothiophene (DPP-DTT) also follows the donor-acceptor copolymer approach as explained above to obtain a bandgap of ~1.3 eV. A copolymer comprising both 1,4-diketopyrrolo[3,4-c]pyrrole (DPP) and thieno[3,2-b]thiophene (TT) is synthesized to have large intermolecular overlapping through π–π stacking. The electron-donating TT and the electron-accepting DPP also strengthen intermolecular interactions through the donor-acceptor interaction to shorten the distance between polymer chains which result in more crystalline structures, both of which would facilitate charge carrier transport. 2D x-ray diffractometry measurements of a stack of polymer thin films revealed that this polymer formed a lamellar crystalline structure in the thin film with an edge-on

stacking which isolates the conjugated core from the dielectric in an FET device[25]. This polymer chain alignment is ideal for obtaining large μ_{FET} as high as 10 $cm^2/V.s$[26].

1.2.2 n-type Semiconductors

1.2.2.1 PCBM

Fullerene derivatives have been used as electron acceptors since the earliest reports on organic photovoltaics. Among these, [6, 6]-phenyl C61-butyric acid methyl ester ($PC_{60}BM$)[27] has been used most widely, with its variant [6, 6]-phenyl C71-butyric acid methyl ester ($PC_{71}BM$)[28] showing enhanced optical absorption and device characteristics. The main characteristics which make them ideal as acceptors in BHJ devices is their ability to form a favourable nanoscale morphology forming a continuous network with the donor polymers in the films, 3D nature of the molecule for ultra-fast charge extraction and a low-lying LUMO level (E_g ≈ -2.2 eV) which enables energy level alignment in a BHJ based photodiode configuration.

1.3 Organic Dielectric Materials

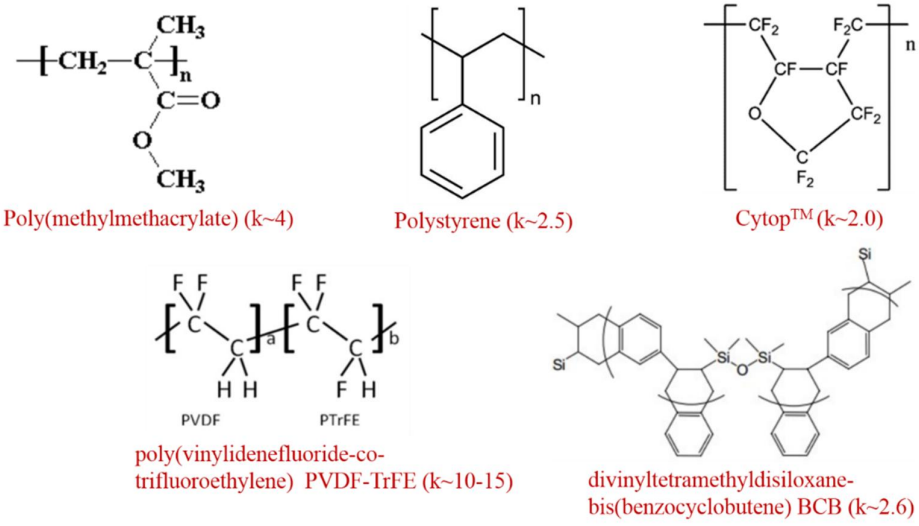

Figure 1.4: Commonly used polymer dielectrics

Polymers which do not exhibit conjugation (hence, no electron delocalization) are inherently insulating materials. Several classics examples such as teflon, polyethylene and polyester can be recalled gauging the impact they have in the

industrial and consumer market today. They are also indispensable in the microelectronics industry and their uses vary depending upon the dielectric constant of the material. The class of organic materials with $\varepsilon' > 2.5$ are extremely useful as dielectrics in metal-insulator FETs or MISFETs. Dielectrics classified as high-k and low-k in effect are cast as layers to isolate the metal gate from the semiconductor. The value of ε' is determined by the polarization strength of an atomic dipole in the polymer backbone and the polymer chain conformation. In a PFET, charge accumulation/inversion and subsequently charge transport in the semiconductor occurs in a narrow channel (3-4 nm) close to the semiconductor-dielectric interface because of molecular dipole polarization in the dielectric as effected by the gate. A list of commonly used low-k and high-k dielectrics are shown in Figure 1.4. The class of organic dielectrics have since emerged not only as thin film polymers but also as self-assembled monolayers (SAMs), molecular dielectrics and hybrids which consist of a bilayer of inorganic and organic dielectrics. Compared to SiO_2, an organic dielectric interface with an organic semiconductor minimizes charge trapping and improves the overall mobility of the FET[29]. As seen with most organic materials, the ability to process them at low temperatures on varied substrate form factors also makes organic dielectrics attractive for use in FETs.

1.3.1 Ferroelectric Dielectrics

Ferroelectric (FE) polymers are a unique class of dielectrics whose nature of ferroelectricity arises from chain conformations rather than ionic-crystal nature as seen in ceramic/inorganic ferroelectric materials. FE materials possess a polar structure which enables spontaneous polarization. This gives rise to high values of ε' which also makes them useful as dielectrics for FETs. In this class of dielectrics, PVDF and its copolymers are well-known semi-crystalline polymers with a degree of crystallinity that can range from 45% to 60% and exhibit strong electromechanical properties. PVDF is a linear chain polymer that has a permanent electric dipole moment approximately perpendicular to the direction of the chain (Figure 1.5(a))[30,31]. The dipoles are due to the difference in electronegativity between the atoms of

hydrogen and fluorine with respect to carbon[32,33]. It is capable of crystallizing in several phases (α, β, γ and δ) and morphologies depending on the processing conditions[34] of which the β phase or the *all-trans* phase is known to exhibit the highest FE and piezoelectric properties. In pure PVDF, an ordered β phase is obtained by either thermal annealing, mechanical rolling, stretching[35] or application of a very strong electric field[36]. A simpler method to ensure ferroelectricity is by introducing a copolymer structure with varying ratios of trifluoroethylene (TrFE) to PVDF. P(VDF-TrFE) readily crystallizes into the β phase upon casting from solution and annealing it between the Curie transition temperature (T_c) and the melting temperature (T_m)[37].

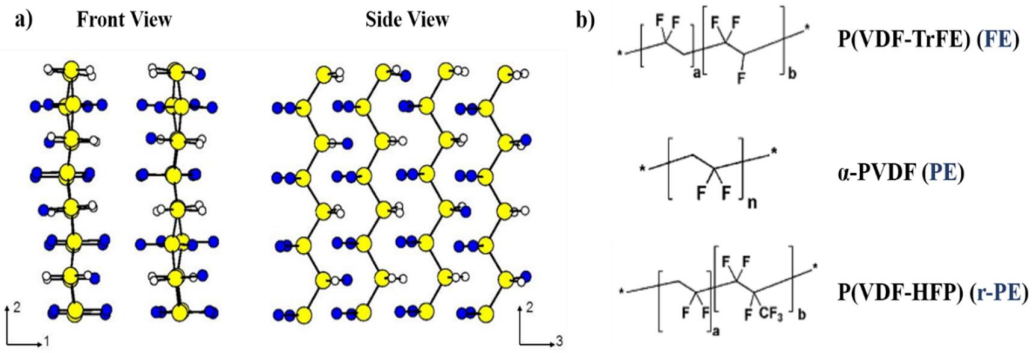

Figure 1.5: a) all-trans conformation showing permanent electric dipoles of P(VDF-TrFE) which gives rise of FE behavior[38], and b) three copolymers of PVDF which can be structurally modified to exhibit FE/PE behavior.

In semi-crystalline P(VDF-TrFE), the β phase is responsible for FE whereas the amorphous region does not contribute significantly. Therefore, FE is intimately dependent upon both the crystal structure and the crystalline-amorphous interaction (or the nanoconfinement effect[39]). The free volume available in the disordered regions of the polymer matrix can be utilized to study the dependence of the FE property of P(VDF-TrFE) on its structural composition. P(VDF-TrFE) composites consisting of a small molecule or polymer secondary component have been studied widely to enhance the dielectric constant as well as the ferroelectric response of the polymer[40,41].

When a homogenous blend of P(VDF-TrFE) and a small molecule is cast into a film, the ensuing thermodynamic and free volume conditions enable the small molecules to get distributed in the amorphous regions upon annealing the cast film. Based on the concentration of the small molecule used, the inter-dependence of the local electric field of the P(VDF-TrFE) grains on the additive molecules[42] and the lamellar organization of the polymer chains[43] can be evaluated for enhanced electrical characteristics. Recently, novel ferroelectric behaviors have also emerged for P(VDF-TrFE) and its copolymers which has resulted in huge enhancement in its dielectric constant and electrostrictive properties[44,45] which enables more efficient electric energy storage[46,47] and makes them attractive for novel applications such as electrocaloric cooling[48,49]. Apart from the broad FE hysteresis loops (Figure 1.6(a)), narrow single (Figure 1.6(b)) and double (Figure 1.6(c)) hysteresis loop behaviors have been obtained by tuning the structure and degree of crystallinity.

In summary, P(VDF-TrFE) being the only high-k polymer dielectric provides an interesting morphology to study several phenomena which have resulted in high performing polymer FETs, transducers and memory devices.

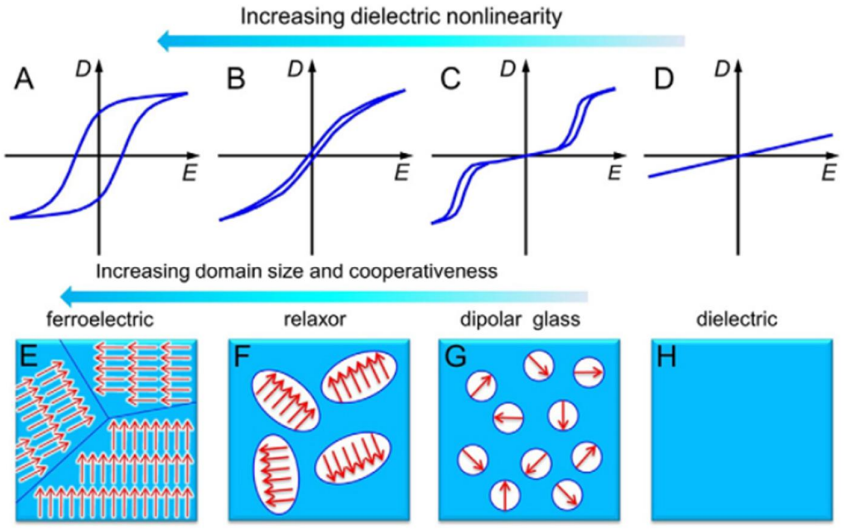

Figure 1.6: Illustrations of hysteresis loops for (A) normal FE, (B) paraelectric/dipolar glass/relaxor FE, (C) antiferroelectric, and (D) normal dielectric. From (D) to (A) the dielectric nonlinearity gradually increases. The bottom panel illustrates ferroelectric domain structures of (E) normal FE, (F) relaxor FE, (G)

dipolar glass, and (H) dielectric polymers. From (H) to (E) the domain size gradually increases. Reproduced with permission[50].

1.3.2 Dielectric Constant as a Complex Quantity

The dielectric constant (ε) which classifies insulators relates directly to the permittivity of the material. It expresses the ability of a material to polarize in response to an externally applied electric field. Physically it means, the greater the polarization in a material in an applied field of given strength, the greater the ε. During the polarization process, the system also undergoes macroscopic changes. This behavior is described by *relaxation*—the phenomenon related to the time taken for recovery of the equilibrium state within a system after removing an external perturbation. It is associated with a time constant τ which in dielectric systems is related to the relaxation of the oriented dipoles when the AC field is removed. However, the orientational motion (or the resistance to motion) of the dipoles also gives rise to an internal friction resulting in dielectric-energy losses. The loss gives an estimate of the breakdown of the material beyond which the current through the dielectric exponentially rises. The dielectric constant ($\epsilon_r^*(\omega)$) is a complex quantity with the magnitude expressed by the real part ($\epsilon_r'(\omega)$) and the energy loss in the material expressed as the imaginary part ($\epsilon_r''(\omega)$).

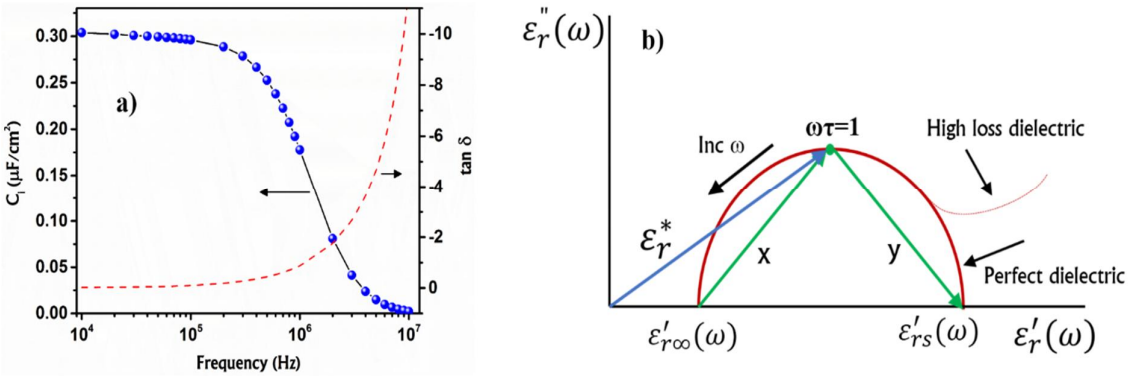

Figure 1.7: a) Representation of a C(f) curve showing capacitance of a thin film dielectric w.r.t frequency. The right y-axis shows the loss tangent as a function of frequency, and b) Cole-Cole plot description.

ε as a function of frequency can be obtained by measuring a material's parallel plate capacitance at varying frequencies. The relation of capacitance with ε is given in equations 1.1-1.3.

$$\varepsilon_r^*(\omega) = \varepsilon_r'(\omega) - i\varepsilon_r''(\omega) \tag{1.1}$$

$$\varepsilon_r'(\omega) = \frac{C(\omega)}{C_0} \; where \; C_0 = \frac{\varepsilon_0 A}{d} \tag{1.2}$$

$$\varepsilon_r''(\omega) = \varepsilon_r'(\omega) tan\delta \tag{1.3}$$

Capacitors using organic dielectrics are generally fabricated by sandwiching a thin film of the dielectric material between two metal electrodes. Figure 1.6(a) shows a representative capacitance vs. frequency curve along with the loss tangent. The energy losses in the system given by tanδ increase with frequency due to the inability of the dipoles to orient at high AC fields. For small AC signal amplitudes (~30 mV), the magnitude of the output signal (C(ω)) and conductance (G(ω)) is directly proportional to the ε' and ε" respectively.

1.3.3 Dielectric Spectroscopy

The evolution of the charge storage distribution in dielectric materials: in other words, the evolution of the materials' polarization (P) when subjected to an external electric field or once this electric field has been removed can be studied by Dielectric Spectroscopy (DS). From the values of ε' and ε", the characteristic relaxation time(s) can be extracted. Temperature dependent studies reveal a thermally-activated behavior $\tau = \tau_0 \exp(\frac{\Delta E_a}{kT})$ where, ΔE_a is the activation energy of the process. Magnitude of ΔE_a yields significant information of the molecular relaxation processes in the dielectric.

Figure 1.7(b) illustrates a simple schematic of the Cole-Cole plot obtained from a DS measurement. The theoretical basis of DS in its simplest form can be explained by Debye's theory[51,52]. It assumes a system of non-interacting fluctuating dipoles whose relaxation (decay) function is exponential in nature once the electric field is removed. The dielectric dispersion for such a system is given by equation 1.4 below.

$$\varepsilon_r^*(\omega) = \varepsilon_{r\infty} + \frac{\varepsilon_{rs} - \varepsilon_{r\infty}}{1 + i\omega\tau} \tag{1.4}$$

where, the real and imaginary parts are, respectively,

$$\varepsilon_r'(\omega) = \varepsilon_{r\infty} + \frac{\varepsilon_{rs} - \varepsilon_{r\infty}}{1 + \omega^2\tau^2} \tag{1.5}$$

$$\varepsilon_r^{"}(\omega) = \frac{\varepsilon_{rs} - \varepsilon_{r\infty}}{1 + \omega^2\tau^2}\omega\tau \tag{1.6}$$

ε_{rs} is the static-asymptotic, low frequency-permittivity, $\varepsilon_{r\infty}$ is the high frequency limit and τ refers to a single relaxation time. When $\varepsilon_r'(\omega)$ is plotted against $\varepsilon_r^{"}(\omega)$, the locus of points traces a perfect semicircle with the maximum corresponding to $\omega\tau = 1$. The Debye theory can explain the molecular relaxations of small molecules which do not contain bulky side groups or intermolecular interacting side chains[53]. When long-chain polymers such as shown in Figure 1.4 are considered, several relaxation phenomena have been observed[54-56] which are associated with multiple relaxation times. For example, a schematic of the α, β and γ relaxations of PMMA is shown in Figure 1.8 which involves polymer backbone (α), side-chain (β) and C-C bond (γ) relaxations which occur at different temperatures and time-scales. A temperature dependence of ε' and ε" at different frequencies yields characteristic peaks which can be traced to phase transitions associated with the respective relaxation phenomena.

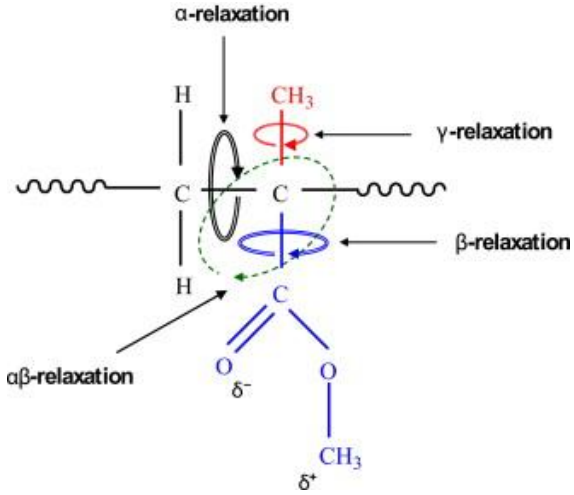

Figure 1.8: Relaxation phenomena in PMMA. Reproduced with permission from [55].

Such systems deviate from the semi-circle plot and are defined by a more general Havriliak-Negami equation (1.7)[57].

$$\varepsilon_r^*(\omega) = \varepsilon_{r\infty} + \frac{\varepsilon_{rs} - \varepsilon_{r\infty}}{[1 + (i\omega\tau)^{1-\alpha}]^{\beta}} \quad (1.7)$$

The parameters α and β ($\alpha \geq 0$, $\beta \leq 1$) are related to the distribution of relaxation times. The Debye ($\alpha = 0$, $\beta = 1$, a semicircle plot) and the Cole –Davidson ($0 < \alpha < 1$, $\beta = 1$, a circular arc plot) expressions are special cases of the Havriliak–Negami relation.

1.3.4 The Dielectric-Semiconductor Interface

The morphological homogeneity and molecular nature of the organic dielectric is of fundamental interest to realize high performance PFET devices. Since charge transport in the PFET occurs within 3-4 nm in the semiconductor at the dielectric-semiconductor interface, obtaining an optimum interface between the dielectric and the semiconductor is critical. The interaction between the semiconductor and the dielectric is mainly Van der Waal's in nature. It has been observed that the polarity of the dielectric layer affects the density of states (DOS) in the semiconductor[58]. The surface bonds of a polar dielectric constitute random dipoles which lead to broadening of the DOS at the interface. This leads to increase in interfacial disorder which hinders charge transport and it is observed that $\mu_{FET} \propto 1/\varepsilon$[59]. Thus, dipolar induced broadening of DOS is related to the nature of the dielectric material and not on the dielectric constant alone[60]. Several approaches have been studied to isolate the conjugated semiconductor core from the dielectric such as developing new active materials[61] and by introducing self-assembled monolayers at the interface[62-64]. Nevertheless, efficient charge transport affects the operation voltage, saturation current, speed of response and device stability of PFETs[24]. A combination of strategies must be utilized to obtain an optimum transport interface for high performing PFETs.

1.4 Organic Field Effect Transistor

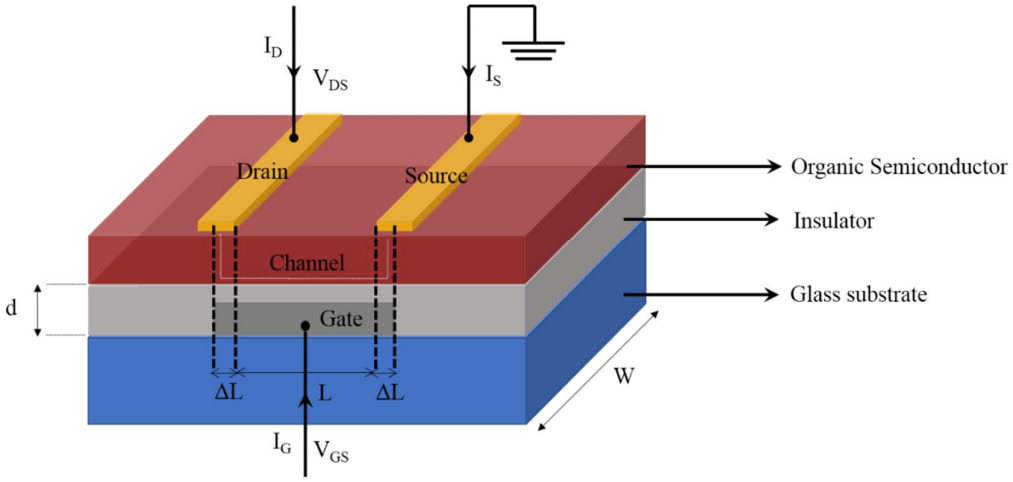

Figure 1.9: Schematic of a bottom-gate top-contact organic FET

Charge carrier mobility of semiconducting polymers and small organic molecules is obtained using the FET geometry[6,65]. Figure 1.9 shows the schematic of a typical bottom-gate top-contact FET, the architecture used throughout this thesis. The organic semiconductor layer is electrically insulated from the gate by a polymer or oxide insulator. On application of a voltage at the gate electrode, a conductive channel is created at the interface between the organic semiconductor and the gate dielectric. Under the influence of both a source-drain and gate bias, charge carriers follow the course marked by the white line in Figure 1.9. It is of significance to stress that organic semiconductors work in an accumulation mode, where the channel of charge carriers formed at the interface under a gate field are injected from the metal source and drain electrodes. Unlike MOSFETs, organic FETs do not work in an inversion mode owing to the absence of band transport and favorable band bending at the metal-semiconductor interface. The presence of traps at the interface hinders free flow of charges which results in selective carrier trapping and thus an absence of inversion[66]. The source and drain injectors in organic FETs are normally chosen depending on their Fermi level and how closely it matches with either the LUMO or the HOMO level of the semiconductor. If the Fermi level of the metal is close to the HOMO level of the organic semiconductor, holes can be injected into the organic semiconductor

with ease. If the Fermi level of the metal is close to the LUMO level of the organic semiconductor, electrons can be injected with ease. If the organic semiconductor has a narrow band-gap and the work-function of the electrodes lies midway between the HOMO and the LUMO, both electrons and holes can be injected into the organic semiconductor depending on the polarity of the gate voltage and the source-drain voltage and the barriers associated. Ambipolarity of polymer FETs thus boils down to having a narrow band-gap, ~1 eV, with an optimally chosen work-function of the source and drain electrodes[67].

The current-voltage characteristics of organic FETs are analyzed using the same formalism that governs charge transport in conventional MOSFETs based on silicon. As shown in Figure 1.10(a), when the transverse gate electric field V_{GS} is much larger than the longitudinal source-drain field (V_{DS}), the accumulated carrier concentration at the interface can be considered uniform. This requires the channel length to be much larger compared to the insulator thickness which is referred as gradual channel approximation. A typical channel length should be about four times the dielectric thickness for observation of proper saturation behavior[68]. This is called the triode regime, where the current is directly proportional to the source-drain (S-D) voltage. In this so called linear regime, from the gradual channel approximation, the current through the channel is given by

$$I_{DS,lin} = \frac{W \mu_{lin} C_i}{L} (V_{GS} - V_T) V_{DS} \tag{1.8}$$

where, W is the channel width, L is the channel length, C_i is the area-normalized dielectric capacitance, μ_{lin} is the linear regime mobility and V_T is the threshold voltage of the device. It is customary to apply voltages V_{GS} and V_{DS} with reference to the source that is kept common (ground). The threshold voltage V_T accounts for the onset of charge accumulation in the channel. When the applied gate voltage $V_{GS} - V_T$ is equal to V_{DS}, the effective voltage between the gate and channel at the drain is zero thus implying zero charge density at this point. The voltage at the source on the other hand is maximum within the channel, thus ensuring the highest charge accumulation

there. The point of zero accumulation of charge carrier density is called the pinch-off point shown as P in Figure 1.10(b).

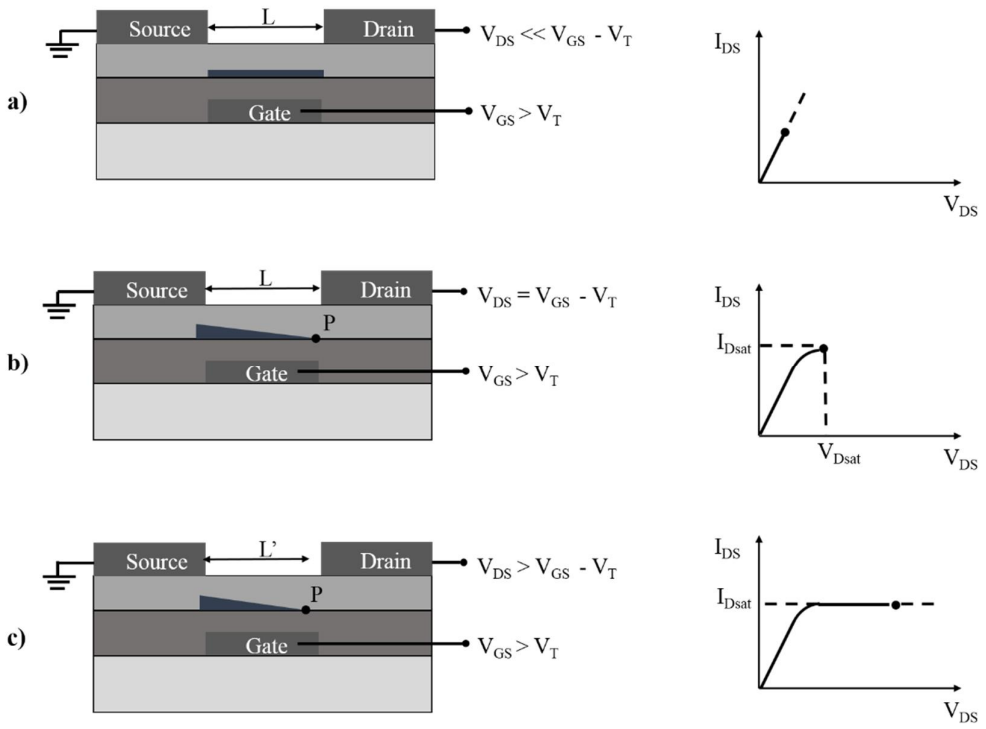

Figure 1.10: Charge distribution within an FET channel under different operating regimes of the device. (a) the linear regime, (b) at the start of saturation, i.e., pinch-off, and (c) the saturation regime.

As long as the applied V_{DS} is larger than $V_{GS} - V_T$, the channel remains pinched-off and the current within the channel remains constant. This transport regime is called the saturation regime. Typical I_{DS} vs V_{DS} characteristics measured under the above circumstances are shown as accompanying figures on the right-hand column of Figure 1.10. In saturation, the current through the channel is given by

$$I_{DS,sat} = \frac{W \mu_{sat} C_i}{2L} (V_{GS} - V_T)^2 \tag{1.9}$$

In most disordered materials, charge carriers do not move in delocalized energy bands as Bloch waves. Rather, owing to the presence of disorder, they hop between localized sites with an average energy known as the activation energy. Among other parameters, the magnitude of the activation energy is an important metric in ascertaining the

nature of charge transport within an organic semiconductor. The mobility derived from FETs can be measured at various temperatures to extract the activation energy responsible for charge transport.

1.5 Other Organic Transistor Architectures

Printable coplanar PFETs can be fabricated with channel lengths of up to 20 µm. Following standard thin-film transistor theory[69], as seen from the previous section, the performance of PFETs largely depends on transistor geometry and material parameters, in particular the channel length L and the charge carrier mobility µ. The saturation current increases linearly with the ratio µ/L and the transit frequency scales with μ/L^2 [70]. Much progress has been made in developing novel organic semiconductors with charge carrier mobilities above 5 $cm^2/V.s$[71,72] with the highest mobility so far measured in a thin-film transistor reported by Yuan et. al. (average mobility of 25 $cm^2/V.s$)[73]. Still, this mobility is significantly lower than charge carrier mobility in silicon—by a factor of approximately 18 compared to the hole mobility of silicon and by a factor of 56 compared to the electron mobility. Besides the comparatively low charge carrier mobility, PFETs are severely limited by their large channel length. Downscaling the channel length of PFETs into the 100 nm regime, as usually done for silicon transistors, seems to be prohibitive considering that organic electronics is a low-cost technology. Furthermore, contact resistances at the source and drain hinder the improvement of device performance as a result of downscaling[74]. The combination of a low charge carrier mobility and large channel lengths leads to low switching frequencies of PFETs. Best organic circuits only reach an operational frequency in the lower MHz range[74], and often have to be operated at several tens of volts to reach higher frequencies[75], which is incompatible with modern low-voltage device applications. Therefore, several forms of vertical FETs (VFETs) that circumvent these issues have gained importance. Some of the novel device architectures to realize high density FETs are shown in Figure 1.11.

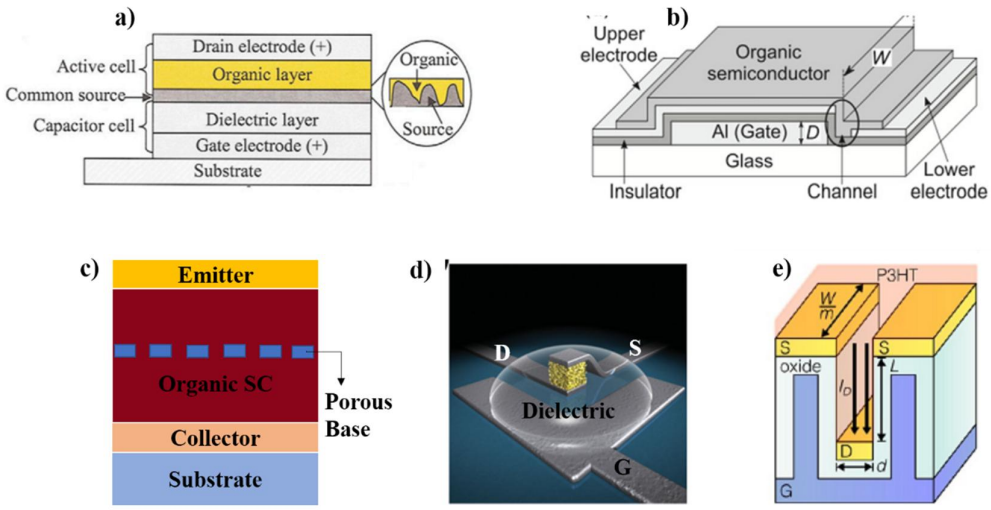

Figure 1.11: Alternate transistor architectures for high density and high-speed applications. (a) organic Schottky barrier transistor (Reproduced with permission from [76]), (b) step-edge VFETs (Reproduced with permission from [77]), (c) organic static induction transistors, (d) VFETs using porous frameworks of semiconductors (Reproduced with permission from [78]), and (e) vertical channel FETs (Reproduced with permission from [79]).

The underlying charge transport mechanism for most vertical transistors is by space-charge current in the bulk of the semiconductor (equation 1.10).

$$J_{on} = \frac{9}{8}\varepsilon_0\varepsilon_r\mu\frac{V_{DS}^2}{L^3}[f(d,l,w)] \tag{1.10}$$

where, *f(d,l,w)* is a function dependent on the geometrical parameters of the channel. Since the ON current depends inversely on the length of the semiconducting channel, thicknesses of the order of 100 nm which can be easily achieved by solution processing improves J_{on} by $>10^3$ times as compared to conventional PFETs. However, a combination of low temperature fabrication along with retaining the simplicity of fabrication to obtain high density organic transistors remains a challenge and is the central focus of many research studies. The mechanism of vertical conduction with gate dependent behavior will be discussed in more detail in Chapter 5.

1.6 Organic Photodiodes

Photodiodes are two-terminal architectures which typically consist of a photoactive layer sandwiched between two metal electrodes and exhibit rectification characteristics. Photodiodes are extremely useful for color imaging due to their light response and are routinely fabricated as 1D and 2D arrays of image sensors[80-82]. Their light sensing feature classifies them into two broad categories: broadband detectors which are mostly utilized for image sensors and narrowband detectors more suitable for sensing monochromatic light or a narrow range of wavelengths. Although silicon dominates the market in visible light sensing and lead sulfide (PbS) detectors for the infra-red (IR) region, they have many limitations such as poor mechanical flexibility, cross-talk between neighboring pixels and wavelength purity to name a few that restrict their application. The emergence of organic semiconductors as an alternative photodiode material has opened the field of photodetection and imaging to a new set of possibilities. They can be processed in vacuum, from solution or by commercial techniques such as inkjet-printing[83] and spray coating[84]. One of the major advantages that has boosted research in organic photodiodes (OPDs) for image sensing is in the capability of OPDs to control the spectral response without the need for color filters or additional optics[85,86]. Emergence of OPDs has been timely given the rise in demand for new PD designs and pixel-cell architectures to serve applications outside traditional digital camera technologies, e.g., in machine vision or the medical arena such as large-area, flexible X-ray imagers or for endoscope-based imaging. The properties of organic semiconductors used for OPDs in this thesis are explained in Section 1.2.1 and the chemical structures are shown in Figure 1.3.

1.6.1 Device Operation

In OPDs, as with organic solar cells (OSCs), incident light photons are absorbed as they travel through the organic semiconductor layer, provided they are of equal or greater energy than the optical gap. Unlike OSCs which work in the photovoltaic mode, OPDs can use an external electric field to assist free charge carrier extraction (photoconductive mode). Since organic semiconductor materials are

generally low dielectric constant media (static $\varepsilon \approx 3$–4), the excitation leads to the formation of a neutral bound state called an exciton (essentially a bound electron-hole pair) rather than free charges. The lack of direct separation of the exciton into free charges is due to the weak screening of the Coulomb interaction of the generated electron-hole pair. For this reason, the free charge generation quantum yield in a homojunction (single material active layer) is low, which causes the maximum external quantum efficiency (EQE) at short-circuit voltage (V = 0) to be ≈1% [87]. Thus, strategies to overcome the exciton binding energy, usually of the order of 0.3-0.5 eV, i.e., >>kT at room temperature[88], are essential for high EQEs. The widely used and successful approach to obtaining improved free charge generation in OPDs (as with OSCs) is to combine an electron 'donor' (D) with an electron 'acceptor' (A) while maintaining a D-A energy offset that is greater than the exciton binding energy to enable electron or hole transfer[89,90] (Figure 1.12). This has been achieved in two ways: by forming a D/A planar heterojunction or a 'bilayer'[91], or by mixing the donor and acceptor in a blend to form a distributed heterojunction across the bulk of the thin solid film (a bulk heterojunction (BHJ) layer)[92]. However, the optimized thickness of the active layers in the bilayer OPD is higher than the exciton diffusion length (usually ≈10-20 nm). Consequently, the excitons' recombination coefficient is higher which results in low extraction and photocurrent. Therefore, BHJ based OPDs are more widely used for photocurrent detection and optimization of device parameters like thickness of the active layer, BHJ components and buffer layers can help realize narrowband or broadband detection[93,94]. Strict requirements are applied to OPDs to utilize/integrate them for photodetection. These are defined as figure of merit parameters and are briefly outlined below.

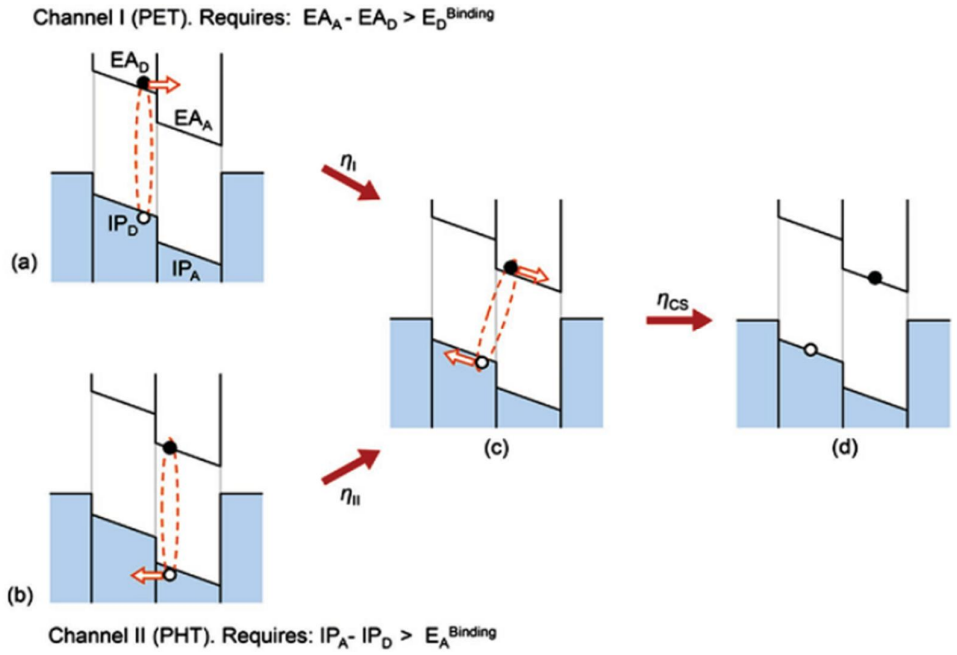

Figure 1.12: Photoexcitation of the electron a) donor and b) acceptor showing exciton dissociation at the organic donor–acceptor interface in each case. Electron affinity (EA) [often equated to the LUMO energy], and ionization potential (IP) [often equated to the HOMO energy]. (a) to (c) electron transfer, and (b) to (c) hole transfer are shown in the figure where ED(A)$^{\text{binding}}$ denotes the binding energy of the excitons. These two charge generation pathways result in interfacial charge transfer (CT) states (c) that dissociate to separated charges (d). Reproduced with permission from [95].

1.6.2 EQE and Responsivity

The EQE also known as the incident photon-to-current efficiency (IPCE) of an OPD is defined as the ratio of extracted electrons to the number of incident photons. It is also very common to express the EQE in a more practical format: the responsivity (R), which is essentially the ratio between the output current and the input light power (units = Amperes/Watt (A/W)). The responsivity and EQE can be calculated as $R = \frac{J_{ph}}{P_{in}}$ and $EQE = \frac{Rh\nu}{e}$ respectively. J_{ph} is the photocurrent density, P_{in} is the incident light power, e is elementary electron charge and hν is the energy of the incident photon, respectively. Assuming a constant light source and therefore a fixed number of photons per unit time, it is the photocurrent that determines the EQE.

Thickness of the active layer strongly influences the EQE as it is directly related to the mobility-lifetime product ($\mu\tau$) of charge carriers. However, a trade-off between the dark current and EQE determines the optimized thickness to improve the OPD performance[93,96]. Responsivity should not be confused with sensitivity, which refers to the lowest detectable light level of a PD, which is related to the signal/noise (S/N) ratio and is therefore heavily influenced by the detection bandwidth[97].

1.6.3 Dark Current and Noise

Dark current is primarily determined by the electronic properties of the device such as trap densities, doping concentrations and work function of the electrodes[98]. Organic semiconductors typically act as intrinsic semiconductors. Since their optical gap is relatively large (>1.5 eV), the thermally generated free charge carrier density is expected to be $<10^5$ cm^{-3}. However, this ideal condition is never achieved and a finite doping density of $>10^{14}$ cm^{-3} is often observed[99,100]. The actual dark current is always larger than what is potentially predicted due to physical defects such as spikes in the Indium Tin Oxide (ITO) substrate, cracks and dust particles, which decrease the shunt resistance. One common way to decrease the dark current is to use thick BHJ layers and good blocking buffer layers with which values as low as 10^{-9} A/cm^2 have been achieved[94,101].

Any current generated in the absence of light defines the noise signal. Noise current, i_{noise} (in units of A), is the root mean square of the random fluctuations in the dark current at a detection bandwidth, B. These fluctuations include shot noise, which is due to the random arrival of quanta of the electric current, Poissonian-distribution of electrons and thermal fluctuations in the charge density in the semiconductor[102]. The experimentally measured noise current in OPDs is shown to be frequency dependent[94] and precise measurement of the 1/f noise has been employed to obtain information about percolation pathways in disordered semiconductors[103,104].

1.6.4 Specific Detectivity

The importance of noise current becomes clear while studying the signal to noise ratio or the minimum detected signal of an OPD. Noise equivalent power (NEP) is defined as the minimum signal obtained when S/N=1 and the measured electrical bandwidth B=1. From the equation of responsivity, we can therefore, obtain the NEP as $\frac{i_{noise}}{R\sqrt{B}}$. The reciprocal of the NEP is the detectivity, D. The detectivity can be normalized to the square root of the device area, A, to obtain the specific detectivity with units of cm $Hz^{1/2}W^{-1}$ or Jones (J) as $D^* = \frac{\sqrt{A}}{NEP} = \frac{R\sqrt{AB}}{i_{noise}}$. To evaluate D* of an OPD, the noise power spectral density must be quantified. D* can be increased by either reducing the noise or by increasing the EQE as seen from the equation. Specific detectivities as high as 10^{13} J in the visible have been reported using organic semiconductors by suppressing the dark current and employing hole blocking layers[105].

1.6.5 Linear Dynamic Range

The linear dynamic range (LDR) is the operational region of a photodetector/sensor. It is expressed as the ratio of the maximum (I_{max}) and minimum detectable current (I_{min}), where I_{min} is limited by the noise current of the photodetector. For practical applications, the LDR must be linear which means that the responsivity in this region is constant. The LDR is calculated as $20*\log\frac{I_{min}}{I_{max}}$ and defined as an order of magnitude of current over which the response is linear. At low light intensities where the bimolecular recombination (i.e., when the recombination is quadratically proportional to the carrier density) is negligible compared to charge extraction, the photocurrent is linear with respect to the light intensity. After a certain light intensity is reached, depending on the charge mobility of the active materials and recombination rate coefficient, the photocurrent deviates from linearity and the responsivity begins to decrease[106]. This deviation is predominantly due to the formation of space charges when the charge carrier concentration increases, resulting in a lowering of the bimolecular lifetime with respect to the charge carrier transit time[106,107]. The lower current limit of the linearity range I_{min} is theoretically i_{noise}. To

improve the LDR, the noise level needs to be lowered to decrease I_{min}. Increasing the space charge formation threshold will result in higher I_{max}. In OPDs this has been done by increasing the slower carrier mobility[106], decreasing the junction thickness[106], minimizing the series resistance[106], and employing BHJ systems with suppressed bimolecular recombination[107].

1.6.6 Speed of Response

The speed of response in an OPD is expressed as the time taken to extract the photo-generated electron and hole carriers. For imaging applications, the photodetector response should be fast enough to capture all levels of light variation in the scene. The temporal bandwidth is a combination of two terms: bandwidth limited by the transit time of the charge carriers and bandwidth limited by the RC time constant. In OPDs, reducing the thickness of the active layer can effectively decrease the carrier transit time as: $t_{tr} = d^2/\mu V$, where, d is the thickness of the active layer, μ charge carrier mobility and V the applied voltage. However, decreasing the thickness also results in increasing the capacitance and therefore the RC time. In general, the temporal bandwidth should be optimized by balancing the thickness, mobility and applied voltage.

1.7 Integrated Organic Devices

The ease of layer by layer processing of organic materials at low temperatures has enabled complex printed components of organic devices combining different classes of devices to obtain printed radio frequency identification (RFID) tags, smart labels and cards, smart packaging and sensors. The PFET forms the most basic driving circuit component for digital applications due to its fundamental performance as a switch which emphasizes its research towards low operating voltage, ambient stable and printable PFETs. Figure 1.13 shows some basic circuit components (single pixel) for integrated circuit applications. Fabricating an (2D) array comprising several such pixels enables serial/parallel addressing with in-pixel charge to voltage conversion with

high signal to noise ratio. The image sensor pixel comprising of a PFET and OPD is considered in detail in chapter 4.

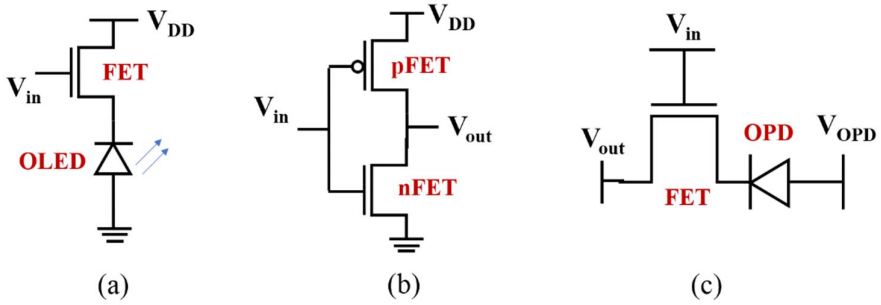

Figure 1.13: a) OLED pixel, b) CMOS logic pixel and c) image sensor pixel showing FET as the building block for digital technology.

1.8 Thesis Outline

The inherent property of facile fabrication and low cost of organic devices have enabled their application in the niche area of flexible and disposable technology[108]. The present thesis comprises largely of experimental studies of three important device systems. A brief introduction and discussion of device simulation is presented in chapter 2. A comprehensive description of the different devices is obtained in chapters 3, 4 and 5. Chapter 6 summaries this thesis and discusses further studies along the lines of the work presented.

In Chapter 3, two strategies to obtain a dielectric layer and a dielectric semiconductor interface are studied for realizing PFETs with low operating voltage, high saturation current and high switching speeds. The first strategy combines the use of self-assembled monolayers (SAMs) with high k oxides to form an ultra-thin hybrid dielectric. The SAM reduces leakage through the oxide and provides a trap-free interface with the organic semiconductor. In the second strategy, a new small molecule organic dielectric is modified synthetically to obtain amorphous, thin films with low leakage which are compatible for PFET fabrication. Novel properties of a composite of the small molecule with high k P(VDF-TrFE) are studied to obtain trap-free dielectric layers for PFETs.

In Chapter 4, the characteristics and efficiency of the low power PFET are studied by integrating it with an OPD for a pixel addressable optical sensor. The integrated PFET-OPD structure operates at < 3 V and yields a reasonable light dependence of up to four orders of incident power. The facile fabrication process of organic layers also enabled us to realize a monolithic structure of the two components which are vertically stacked. This quasi 3D structure reproduced the sensor's light response and the fundamental charge extraction dynamics are verified using a 2D device simulation package Atlas by Silvaco, Inc.

Chapter 5 addresses the capability of organic transistors to be used in high density and high-speed circuits. A vertical organic transistor configuration is realized using a porous alumina membrane as a template to demonstrate massively parallel organization (10^9 transistors/mm^2) of connected three-terminal devices called the organic nano-triode array (ONTA). 2D device simulation of a single pore showed classical transistor operation for a pore dimension of 100 nm. Each pore in the array is also addressable individually using a conducting cantilever which makes the ONTA suitable for high density miniaturized integrated circuits.

Chapter 6 summarizes the results obtained and the major contributions to this field. A brief outline of essential, possible as well as innovative studies which should be pursued is also presented as the outlook of this thesis work.

1.8 References

1 Chiang, C. K. *et al.* Electrical conductivity in doped polyacetylene. *Physical review letters* **39**, 1098 (1977).

2 Shirakawa, H., Louis, E. J., MacDiarmid, A. G., Chiang, C. K. & Heeger, A. J. Synthesis of electrically conducting organic polymers: halogen derivatives of polyacetylene,(CH) x. *Journal of the Chemical Society, Chemical Communications*, 578-580 (1977).

3 Burroughes, J. *et al.* Light-emitting diodes based on conjugated polymers. *nature* **347**, 539 (1990).

4 Koezuka, H., Tsumura, A. & Ando, T. Field-effect transistor with polythiophene thin film. *Synthetic Metals* **18**, 699-704 (1987).

5 Sariciftci, N. S., Smilowitz, L., Heeger, A. J. & Wudl, F. Photoinduced electron transfer from a conducting polymer to buckminsterfullerene. *Science* **258**, 1474-1476 (1992).

6 Sirringhaus, H. Device physics of solution-processed organic field-effect transistors. *Advanced Materials* **17**, 2411-2425 (2005).

7 Albanesius, C.

8 Sekitani, T. & Someya, T. Stretchable, large-area organic electronics. *Advanced Materials* **22**, 2228-2246 (2010).

9 Coropceanu, V., Li, H., Winget, P., Zhu, L. & Brédas, J.-L. Electronic-structure theory of organic semiconductors: charge-transport parameters and metal/organic interfaces. *Annual Review of Materials Research* **43**, 63-87 (2013).

10 Roncali, J. Conjugated poly (thiophenes): synthesis, functionalization, and applications. *Chemical Reviews* **92**, 711-738 (1992).

11 Bässler, H., Borsenberger, P. & Perry, R. Charge transport in poly (methylphenylsilane): The case for superimposed disorder and polaron effects. *Journal of Polymer Science Part B: Polymer Physics* **32**, 1677-1685 (1994).

12 Parris, P. E., Kenkre, V. M. & Dunlap, D. H. Nature of charge carriers in disordered molecular solids: Are polarons compatible with observations? *Physical review letters* **87**, 126601 (2001).

13 Fishchuk, I., Kadashchuk, A., Bässler, H. & Nešpůrek, S. Nondispersive polaron transport in disordered organic solids. *Physical Review B* **67**, 224303 (2003).

14 Holstein, T. Studies of polaron motion: Part I. The molecular-crystal model. *Annals of physics* **8**, 325-342 (1959).

15 Deng, Y. Y. & Sirringhaus, H. Optical absorptions of polyfluorene transistors. *Physical Review B* **72**, 045207 (2005).

16 Capone, M., Stephan, W. & Grilli, M. Small-polaron formation and optical absorption in Su-Schrieffer-Heeger and Holstein models. *Physical Review B* **56**, 4484 (1997).

17 McCullough, R. D. The chemistry of conducting polythiophenes. *Advanced Materials* **10**, 93-116 (1998).

18 Sirringhaus, H. *et al.* Two-dimensional charge transport in self-organized, high-mobility conjugated polymers. *Nature* **401**, 685-688 (1999).

19 Zen, A. *et al.* Effect of Molecular Weight and Annealing of Poly(3-hexylthiophene)s on the Performance of Organic Field-Effect Transistors. *Adv. Funct. Mater.* **14**, 757-764, doi:10.1002/adfm.200400017 (2004).

20 Huo, L. *et al.* Replacing Alkoxy Groups with Alkylthienyl Groups: A Feasible Approach To Improve the Properties of Photovoltaic Polymers. *Angewandte Chemie International Edition* **50**, 9697-9702, doi:10.1002/anie.201103313 (2011).

21 Zhou, H., Yang, L., Stoneking, S. & You, W. A weak donor− strong acceptor strategy to design ideal polymers for organic solar cells. *ACS applied materials & interfaces* **2**, 1377-1383 (2010).

22 Noriega, R. *et al.* A general relationship between disorder, aggregation and charge transport in conjugated polymers. *Nat Mater* **12**, 1038-1044, doi:10.1038/nmat3722

http://www.nature.com/nmat/journal/v12/n11/abs/nmat3722.html#supplementary-information (2013).

23 Guo, X. *et al.* Dialkoxybithiazole: A New Building Block for Head-to-Head Polymer Semiconductors. *Journal of the American Chemical Society* **135**, 1986-1996, doi:10.1021/ja3120532 (2013).

24 Senanayak, S. P. *et al.* Self-Assembled Nanodielectrics for High-Speed, Low-Voltage Solution-Processed Polymer Logic Circuits. *Advanced Electronic Materials* **1** (2015).

25 Li, Y., Singh, S. P. & Sonar, P. A High Mobility P-Type DPP-Thieno [3, 2-b] thiophene Copolymer for Organic Thin-Film Transistors. *Advanced Materials* **22**, 4862-4866 (2010).

26 Li, J. *et al.* A stable solution-processed polymer semiconductor with record high-mobility for printed transistors. *Scientific reports* **2**, 754 (2012).

27 Hummelen, J. C. *et al.* Preparation and Characterization of Fulleroid and Methanofullerene Derivatives. *The Journal of Organic Chemistry* **60**, 532-538, doi:10.1021/jo00108a012 (1995).

28 Wienk, M. M. *et al.* Efficient Methano[70]fullerene/MDMO-PPV Bulk Heterojunction Photovoltaic Cells. *Angewandte Chemie International Edition* **42**, 3371-3375, doi:10.1002/anie.200351647 (2003).

29 Todescato, F. *et al.* Correlation between dielectric/organic interface properties and key electrical parameters in PPV-based OFETs. *The Journal of Physical Chemistry B* **112**, 10130-10136 (2008).

30 Nalwa, H. S. *Ferroelectric Polymers: Chemistry, Physics and Applications.* (Taylor & Francis: New York, USA, 1995).

31 Lovinger, A. J. *Poly(vinylidene fluoride).* 1st ed. edn, 1982 (Springer Netherlands).

32 Lovinger, A. J., Furukawa, T., Davis, G. & Broadhurst, M. Crystallographic changes characterizing the Curie transition in three ferroelectric copolymers of vinylidene fluoride and trifluoroethylene: 1. As-crystallized samples. *Polymer* **24**, 1225-1232 (1983).

33 Gregorio, R. & Ueno, E. Effect of crystalline phase, orientation and temperature on the dielectric properties of poly (vinylidene fluoride)(PVDF). *Journal of Materials Science* **34**, 4489-4500 (1999).

34 Nalwa, H. S. Recent developments in ferroelectric polymers. *J. Macromol. Sci. Part C* 341–432 (1991).

35 Imamura, R., Silva, A. & Gregorio, R. $\gamma \rightarrow \beta$ Phase Transformation Induced in Poly (vinylidene fluoride) by Stretching. *Journal of applied polymer science* **110**, 3242-3246 (2008).

36 Lovinger, A. J., Furukawa, T., Davis, G. & Broadhurst, M. Crystallographic changes characterizing the Curie transition in three ferroelectric copolymers of vinylidene fluoride and trifluoroethylene: 2. Oriented or poled samples. *Polymer* **24**, 1233-1239 (1983).

37 Furukawa, T., Date, M., Fukada, E., Tajitsu, Y. & Chiba, A. Ferroelectric behavior in the copolymer of vinylidenefluoride and trifluoroethylene. *Japanese Journal of Applied Physics* **19**, L109 (1980).

38 Serge Nakhmanson, M. B. N., Jerry Bernholc. First principles studies of self-polarization in electroactive polymers. *APS March Meeting* (2005).

39 Guan, F. *et al.* Confinement-Induced High-Field Antiferroelectric-like Behavior in a Poly (vinylidene fluoride-co-trifluoroethylene-co-chlorotrifluoroethylene)-graft-polystyrene Graft Copolymer. *Macromolecules* **44**, 2190-2199 (2011).

40 Zhou, T. *et al.* Improving dielectric properties of BaTiO3/ferroelectric polymer composites by employing surface hydroxylated BaTiO3 nanoparticles. *ACS applied materials & interfaces* **3**, 2184-2188 (2011).

41 Valiyaneerilakkal, U., Singh, K. & Varghese, S. Device level optimization of poly (vinylidene fluoride-trifluoroethylene)–zinc oxide polymer nanocomposite thin films for ferroelectric applications. *Journal of Applied Physics* **118**, 204102 (2015).

42 Chellappan, K. V., Kandappa, S. K., Rajaram, S. & Narayan, K. Ferroelectric polymer matrix for probing molecular organization in perylene diimides. *The journal of physical chemistry letters* **6**, 224-229 (2014).

43 Capsal, J.-F., Galineau, J., Lallart, M., Cottinet, P.-J. & Guyomar, D. Plasticized relaxor ferroelectric terpolymer: Toward giant electrostriction, high mechanical energy and low electric field actuators. *Sensors and Actuators A: Physical* **207**, 25-31 (2014).

44 Zhang, Q. *et al.* An all-organic composite actuator material with a high dielectric constant. *Nature* **419**, 284 (2002).

45 Xia, F. *et al.* High electromechanical responses in a poly (vinylidene fluoride–trifluoroethylene–chlorofluoroethylene) terpolymer. *Advanced Materials* **14**, 1574-1577 (2002).

46 Zhu, L. & Wang, Q. Novel ferroelectric polymers for high energy density and low loss dielectrics. *Macromolecules* **45**, 2937-2954 (2012).

47 Zhou, X., Chu, B., Neese, B., Lin, M. & Zhang, Q. Electrical energy density and discharge characteristics of a poly (vinylidene fluoride-chlorotrifluoroethylene) copolymer. *IEEE transactions on dielectrics and electrical insulation* **14** (2007).

48 Neese, B. *et al.* Large electrocaloric effect in ferroelectric polymers near room temperature. *Science* **321**, 821-823 (2008).

49 Lu, S. *et al.* Organic and inorganic relaxor ferroelectrics with giant electrocaloric effect. *Applied physics letters* **97**, 162904 (2010).

50 Yang, L. *et al.* Novel polymer ferroelectric behavior via crystal isomorphism and the nanoconfinement effect. *Polymer* **54**, 1709-1728 (2013).

51 Debye, P. *Z. Phys* **13** (1912).

52 Debye, P. *Polar Molecules.* (Dover Press, 1945).

53 Cole, K. S. & Cole, R. H. Dispersion and absorption in dielectrics I. Alternating current characteristics. *The Journal of chemical physics* **9**, 341-351 (1941).

54 Yagi, T., Tatemoto, M. & Sako, J.-i. Transition behavior and dielectric properties in trifluoroethylene and vinylidene fluoride copolymers. *Polymer Journal* **12**, 209 (1980).

55 Sengwa, R. & Choudhary, S. Dielectric properties and fluctuating relaxation processes of poly (methyl methacrylate) based polymeric nanocomposite electrolytes. *Journal of Physics and Chemistry of Solids* **75**, 765-774 (2014).

56 Seki, Y., Kita, R., Shinyashiki, N., Yagihara, S. & Yoneyama, M. in *AIP Conference Proceedings.* 466-469 (AIP).

57 Havriliak, S. & Negami, S. A complex plane representation of dielectric and mechanical relaxation processes in some polymers. *Polymer* **8**, 161-210 (1967).

58 Veres, J., Ogier, S. D., Leeming, S. W., Cupertino, D. C. & Mohialdin Khaffaf, S. Low-k insulators as the choice of dielectrics in organic field-effect transistors. *Advanced Functional Materials* **13**, 199-204 (2003).

59 Hulea, I. *et al.* Tunable Fröhlich polarons in organic single-crystal transistors. *Nature materials* **5**, 982 (2006).

60 Senanayak, S. P., Guha, S. & Narayan, K. Polarization fluctuation dominated electrical transport processes of polymer-based ferroelectric field effect transistors. *Physical Review B* **85**, 115311 (2012).

61 Yan, H. *et al.* A high-mobility electron-transporting polymer for printed transistors. *Nature* **457**, 679 (2009).

62 Klauk, H., Zschieschang, U., Pflaum, J. & Halik, M. Ultralow-power organic complementary circuits. *Nature* **445**, 745-748 (2007).

63 Labram, J., Wöbkenberg, P., Bradley, D. & Anthopoulos, T. Low-voltage ambipolar phototransistors based on a pentacene/PC61BM heterostructure and a self-assembled nano-dielectric. *Organic Electronics* **11**, 1250-1254 (2010).

64 Halik, M. *et al.* Low-voltage organic transistors with an amorphous molecular gate dielectric. *Nature* **431**, 963 (2004).

65 Horowitz, G. Organic field-effect transistors. *Advanced materials* **10**, 365-377 (1998).

66 Brondijk, J., Spijkman, M., Van Seijen, F., Blom, P. & De Leeuw, D. Formation of inversion layers in organic field-effect transistors. *Physical Review B* **85**, 165310 (2012).

67 Sirringhaus, H. Organic semiconductors: An equal-opportunity conductor. *Nature Materials* **2**, 641 (2003).

68 Noh, Y.-Y., Zhao, N., Caironi, M. & Sirringhaus, H. Downscaling of self-aligned, all-printed polymer thin-film transistors. *Nature nanotechnology* **2**, 784 (2007).

69 M Riede, B. L. a. K. L. Organic semiconductors. *Comprehensive Semicond. Sci. Technol.* **4**, 448–507 (2011).

70 Senanayak, S. P. & Narayan, K. Strategies for Fast-Switching in All-Polymer Field Effect Transistors. *Advanced Functional Materials* **24**, 3324-3331 (2014).

71 Kang, M. J. *et al.* Alkylated Dinaphtho [2, 3-b: 2′, 3′-f] Thieno [3, 2-b] Thiophenes (Cn-DNTTs): Organic Semiconductors for High-Performance Thin-Film Transistors. *Advanced Materials* **23**, 1222-1225 (2011).

72 Hofmockel, R. *et al.* High-mobility organic thin-film transistors based on a small-molecule semiconductor deposited in vacuum and by solution shearing. *Organic Electronics* **14**, 3213-3221 (2013).

73 Yuan, Y. *et al.* Ultra-high mobility transparent organic thin film transistors grown by an off-centre spin-coating method. *Nature communications* **5**, 3005 (2014).

74 Ante, F. *et al.* Contact resistance and megahertz operation of aggressively scaled organic transistors. *small* **8**, 73-79 (2012).

75 Kitamura, M. & Arakawa, Y. Current-gain cutoff frequencies above 10 MHz for organic thin-film transistors with high mobility and low parasitic capacitance. *Applied Physics Letters* **95**, 023503 (2009).

76 Ma, L. & Yang, Y. Unique architecture and concept for high-performance organic transistors. *Applied physics letters* **85**, 5084-5086 (2004).

77 Uno, M. *et al.* High-Speed Flexible Organic Field-Effect Transistors with a 3D Structure. *Advanced Materials* **23**, 3047-3051 (2011).

78 Baby, T. T. *et al.* Sub-50 nm Channel Vertical Field-Effect Transistors using Conventional Ink-Jet Printing. *Advanced Materials* **29** (2017).

79 Johnston, D. E., Yager, K. G., Nam, C.-Y., Ocko, B. M. & Black, C. T. One-volt operation of high-current vertical channel polymer semiconductor field-effect transistors. *Nano letters* **12**, 4181-4186 (2012).

80 Ng, T. N., Wong, W. S., Chabinyc, M. L., Sambandan, S. & Street, R. A. Flexible image sensor array with bulk heterojunction organic photodiode. *Applied Physics Letters* **92**, 191 (2008).

81 Yu, G., Wang, J., McElvain, J. & Heeger, A. J. Large-area, full-color image sensors made with semiconducting polymers. *Advanced Materials* **10**, 1431-1434 (1998).

82 Lavery, L. L., Whiting, G. L. & Arias, A. C. All ink-jet printed polyfluorene photosensor for high illuminance detection. *Organic Electronics* **12**, 682-685 (2011).

83 Azzellino, G. *et al.* Fully Inkjet-Printed Organic Photodetectors with High Quantum Yield. *Advanced Materials* **25**, 6829-6833 (2013).

84 Tedde, S. F. *et al.* Fully spray coated organic photodiodes. *Nano letters* **9**, 980-983 (2009).

85 Satoshi Aihara, M. K. in *Broadcast Technology* Vol. No. 49 (NHK Science and Technology Research Laboratories, 2012).

86 Seo, H. *et al.* in *Proc. 2011 International Image Sensor Workshop (IISW2011).* 236-239.

87 Hedley, G. J. *et al.* Determining the optimum morphology in high-performance polymer-fullerene organic photovoltaic cells. *Nature Communications* **4**, 2867 (2013).

88 Knupfer, M. Exciton binding energies in organic semiconductors. *Applied Physics A* **77**, 623-626 (2003).

89 Coffey, D. C. *et al.* An optimal driving force for converting excitons into free carriers in excitonic solar cells. *The Journal of Physical Chemistry C* **116**, 8916-8923 (2012).

90 Bakulin, A. A. *et al.* Charge-transfer state dynamics following hole and electron transfer in organic photovoltaic devices. *The journal of physical chemistry letters* **4**, 209-215 (2012).

91 Kudo, K. & Moriizumi, T. Spectrum-controllable color sensors using organic dyes. *Applied Physics Letters* **39**, 609-611 (1981).

92 Yu, G., Gao, J., Hummelen, J. C., Wudl, F. & Heeger, A. J. Polymer photovoltaic cells: enhanced efficiencies via a network of internal donor-acceptor heterojunctions. *Science* **270**, 1789-1791 (1995).

93 Armin, A., Jansen-van Vuuren, R. D., Kopidakis, N., Burn, P. L. & Meredith, P. Narrowband light detection via internal quantum efficiency manipulation of organic photodiodes. *Nature communications* **6**, 6343 (2015).

94 Lyons, D. M. *et al.* Narrow band green organic photodiodes for imaging. *Organic Electronics* **15**, 2903-2911 (2014).

95 Ohta, J. *Smart CMOS Image Sensors and Applications*. Vol. Ch. 3 (CRC Press, 2007).

96 Moulé, A. J., Bonekamp, J. B. & Meerholz, K. The effect of active layer thickness and composition on the performance of bulk-heterojunction solar cells. *Journal of applied physics* **100**, 094503 (2006).

97 Konstantatos, G., Clifford, J., Levina, L. & Sargent, E. H. Sensitive solution-processed visible-wavelength photodetectors. *Nature photonics* **1**, 531 (2007).

98 Wetzelaer, G., Kuik, M., Lenes, M. & Blom, P. Origin of the dark-current ideality factor in polymer: fullerene bulk heterojunction solar cells. *Applied physics letters* **99**, 153506 (2011).

99 Armin, A. *et al.* Doping-Induced Screening of the Built-in-Field in Organic Solar Cells: Effect on Charge Transport and Recombination. *Advanced Energy Materials* **3**, 321-327 (2013).

100 Morfa, A. J., Nardes, A. M., Shaheen, S. E., Kopidakis, N. & Van de Lagemaat, J. Time-of-Flight Studies of Electron-Collection Kinetics in Polymer: Fullerene Bulk-Heterojunction Solar Cells. *Advanced Functional Materials* **21**, 2580-2586 (2011).

101 Gong, X. *et al.* Semiconducting polymer photodetectors with electron and hole blocking layers: High detectivity in the near-infrared. *Sensors* **10**, 6488-6496 (2010).

102 Martin, T. & Landauer, R. Wave-packet approach to noise in multichannel mesoscopic systems. *Physical Review B* **45**, 1742 (1992).

103 Carbone, A. & Mazzetti, P. Current noise spectroscopy of deep energy levels in photoconductors. *Journal of applied physics* **80**, 1559-1566 (1996).

104 Bag, M., Vidhyadhiraja, N. & Narayan, K. Fluctuations in photocurrent of bulk heterojunction polymer solar cells—A valuable tool to understand microscopic and degradation processes. *Applied Physics Letters* **101**, 043903 (2012).

105 Guo, F., Xiao, Z. & Huang, J. Fullerene Photodetectors with a Linear Dynamic Range of 90 dB Enabled by a Cross-Linkable Buffer Layer. *Advanced Optical Materials* **1**, 289-294 (2013).

106 Stolterfoht, M. *et al.* Photocarrier drift distance in organic solar cells and photodetectors. *Scientific reports* **5**, 9949 (2015).

107 Jin, H. *et al.* Bulk heterojunction thickness uniformity–a limiting factor in large area organic solar cells? *physica status solidi (a)* **212**, 2246-2254 (2015).

108 Zirkl, M. *et al.* An All-Printed Ferroelectric Active Matrix Sensor Network Based on Only Five Functional Materials Forming a Touchless Control Interface. *Advanced Materials* **23**, 2069-2074 (2011).

Device Simulations-Theory

Chapter 2

2.1 Introduction

Numerical simulations are a useful way to understand semiconductor device operation especially where unconventional materials and complex fabrication processes are involved. Under the broad term of technology computer-aided design (TCAD), 2D finite-element based simulations have acquired mainstream importance to understand concepts ranging from device physics to process flows. Numerical simulations in this thesis were performed by a commercially available 2D device simulation package called Atlas by Silvaco, Inc[1]. The use of TCAD software for organic semiconductor devices has only recently gained importance in research by incorporating organic materials specific models for transport[2,3]. Atlas is a materials'-based device simulator which utilizes inputs defined for material specific parameters to solve for the electrical characteristics of a device. Physically-based simulation is advantageous for two important reasons. Firstly, it is almost always quicker and cheaper than performing experiments. Secondly, it provides information that is difficult or impossible to measure. As a result, the predictability of the output is not only realistic but also insightful which provides a rulebook for fabricating complex device structures with optimal performance. The drawback of a physically-based simulation is that all the relevant physics need to be incorporated into the simulator implying that some experimental data is required for accurate parameter extraction through simulation. Moreover, numerical procedures must be implemented to solve the associated semiconductor equations which requires prior know-how of the charge transport processes in the material.

2.2 How a Device Simulator Works

A finite-element simulator calculates a set of physical equations in a user-defined device structure, which is approximated to a 2D mesh (or grid). In Figure 2.1, the function of this type of simulator is illustrated by specifying the information required to run a simulation, and the results obtained for analysis and design. The device dimensions are first specified by the user and the entire device area in the x and y

directions is divided into a grid which consists of a node, mesh and interpolation line. The result of such a division enables the physical equations to be solved at each node point with an interpolation formula to incorporate the dependence of the neighboring points. The mesh size is controlled by the user and finer meshes yield higher accuracy for the desired spatial distributions of charges/dopants in a material or for extremely thin layers of materials.

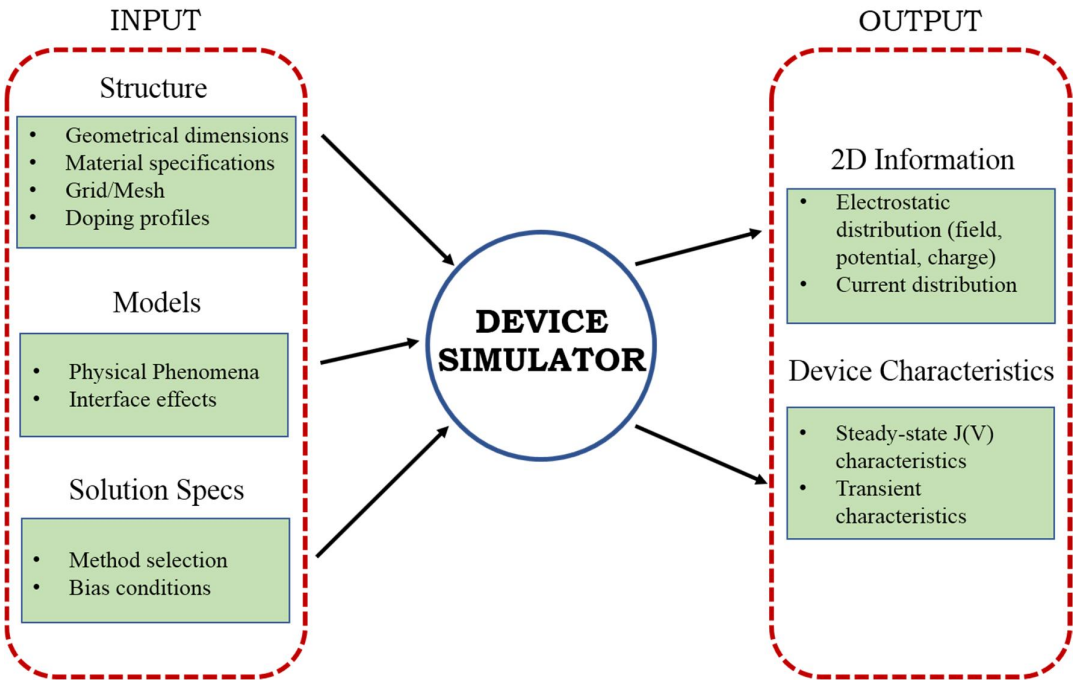

Figure 2.1: Illustration of the working principle and flow of the 2D device simulator.

2.3 Building a Simulation Code

2.3.1 Defining a Mesh

A device simulation by the finite-element method begins with the construction of a mesh which approximates a geometric domain. The mesh discretizes the entire device structure to solve the semiconductor equations. Figure 2.2(a) shows an example 2D output file from Atlas and Figure 2.2(b) is a simplified illustration of the mesh structure. As the figure suggests, the mesh consists of finely interconnected lines forming equilateral triangles. Each node point is attributed with the material parameters and exact solutions are obtained by solving equations which describe the

attributes. Using a fine mesh that contains very closely-defined lines results in more reliable results because it approximates a real continuous medium well. However, the simulation time gets longer as the number of cross-section points is increased. Therefore, it is reasonable to define a high-resolution (fine) mesh only within the most important regions where the analysis is to be made, with a relatively coarse mesh elsewhere. An example of this principle of making use of a non-uniform mesh in Atlas, with a significantly improved accuracy at metal/semiconductor interfaces is illustrated in Figure 2.2(a). Atlas provides exact solutions at each node defined by the grid lines, and also calculates interpolation values along the diagonals. A maximum allowed node limit of 106 is capable in Atlas, which is large enough in most cases.

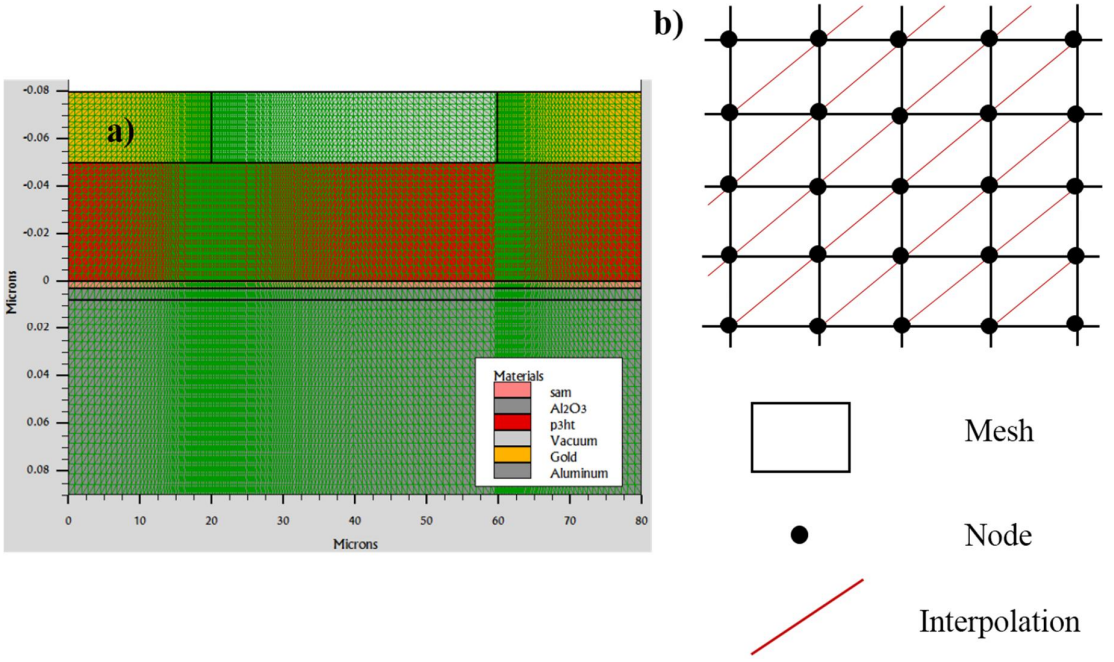

Figure 2.2: a) Non-uniform mesh layout of a typical PFET as defined at the start of the simulation, b) illustration of the mesh layout for better understanding.

2.3.2 Material and Region Specifications

Once the mesh is specified, every region is defined by the material parameters. After X and Y dimensions are assigned, region and material specifications include type: metal, semiconductor or insulator, dopant concentrations, permittivity, electron affinity, bandgap and density of states. Every material belongs to a class provided in

the Atlas database. However, user defined materials can also be defined by using an appropriate syntax. Apart from specifying semiconductor and insulator layers, electrodes are also specified accordingly.

Boundary conditions are specified as contacts which can be Ohmic or Schottky. By specifying the workfunction of the metal, the contact is simply defined as Ohmic or Schottky relative to the semiconductor HOMO/LUMO level. Voltage and current boundary conditions can also be specified when ground and floating contacts, respectively, are specified. Organic materials are generally un-doped materials, however unintentional doping during device processing has been shown to change the device performance[4]. In this thesis, unless otherwise specified, all the simulations have been done without considering any dopant profiles.

Another important factor to consider while defining organic layers is the presence of defect levels mostly in the sub-bandgap energies. The lack of crystallinity in molecular solids such as polymeric semiconductors gives rise to significant disorder in these materials. The disorder materializes as a set of discrete energy levels in the bandgap, which is the primary cause for hopping type transport in the class of amorphous semiconductors[5]. In the hopping regime, charge transport is thermally activated within the manifold of the discrete trap levels. These trap levels generally have a distribution in the form of an exponential, gaussian or a combination of the two functions which has been the center of study by many research groups[6-8]. The output current of a device is strongly affected by the hopping transport and therefore, it is extremely important to define the trap densities during simulation. All simulations performed in this thesis include an exponential DOS from the LUMO/HOMO band edge and an illustration of a typical distribution is shown in Figure 2.3(a) and (b).

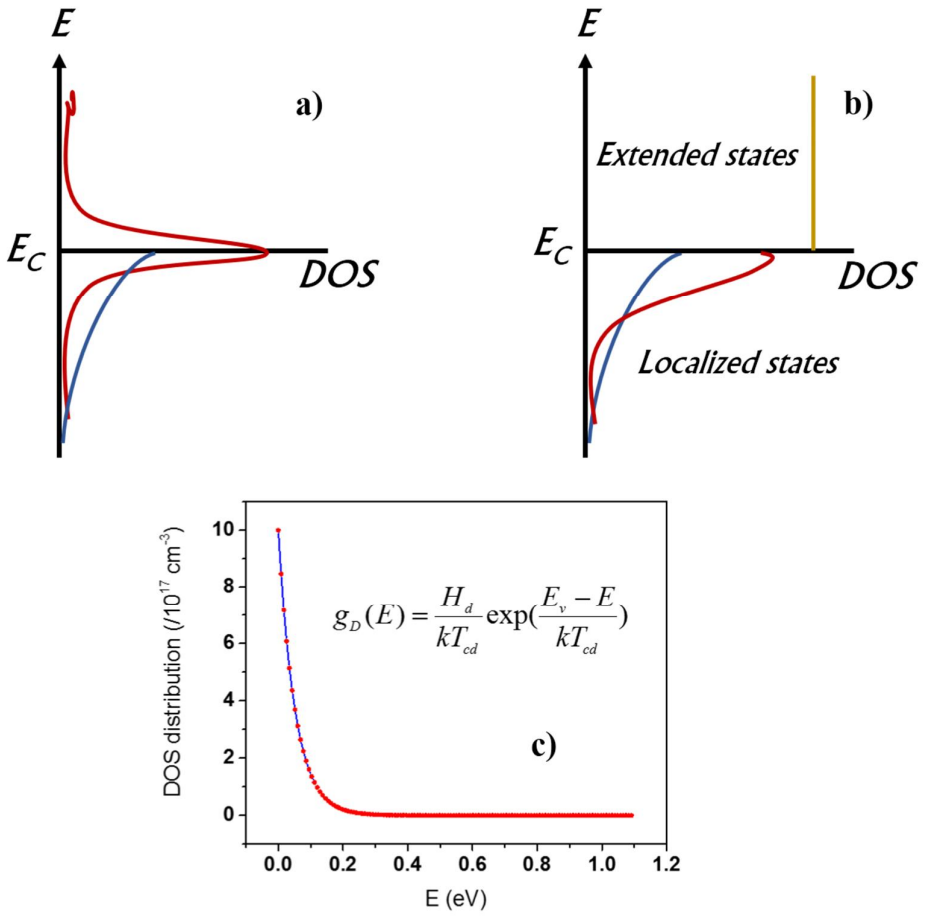

Figure 2.3: a) Illustration of exponential and Gaussian distribution of DOS for a disordered semiconductor, b) difference between discrete energy levels versus the continuum, and c) the exponential DOS modeled in Atlas for organic semiconductors.

The total DOS distribution is given by $g_D(E)$ and is composed of a donor-like band DOS. One of the primary models for organic defects[9] is defined for the defects which have a characteristic trap temperature given by T_{cd}. H_d is the donor trap DOS and E_V signifies the HOMO band edge which is defined at E=0 eV. The trapped state concentrations for holes depends on the donor probability of occupation $f_{tD}(E, n, p)$ and the DOS distribution g_D, and is given by: $p_D = \int_{E_C}^{E_V} g_D(E).f_{tD}(E,n,p)dE$.

2.3.3 Physical Models for Organic Semiconductors

Extensive studies in device physics have resulted in a mathematical model that operates on any semiconductor device[10]. The model consists of a set of fundamental

equations which link together the electrostatic potential and the carrier densities within a simulation domain. These equations, which are solved inside any general-purpose device simulator consist of Poisson's equation, the continuity equations and the transport equations as shown below. The Poisson's equation relates variations in electrostatic potential to local charge densities. The continuity and the transport equations describe the way the electron and hole densities evolve as a result of transport processes, generation processes, and recombination processes. Upon this, a wide variety of models based on the material characteristics should be incorporated during simulation for calculating the steady-state solutions of the device.

$$J_n = qn\mu_n F + qD_n \nabla n$$

$$J_p = qp\mu_p F + qD_p \nabla p$$

$$\frac{\partial n}{\partial t} = \frac{1}{q}\nabla . J_n + G_n - R_n$$

$$\frac{\partial p}{\partial t} = -\frac{1}{q}\nabla . J_p + G_p - R_p$$

$$\nabla . (\varepsilon_0 \varepsilon_r \nabla V) = -q(p - n + N_D - N_A)$$

The simplest model for charge transport is the Drift-Diffusion Model[11]. This model is simple and reliable in the sense that it does not introduce any independent variables in addition to potential and charge carrier concentrations n and p. Until recently, the drift-diffusion model was adequate for nearly all devices that were technologically feasible. However, it should be noted that, with decreasing feature sizes, quantum effects can start dominating thereby rendering the model inadequate. Secondly, the emergence of new classes of materials such as organic semiconductors, 2D Van der Waals' materials and semiconducting quantum dots to name a few have proved the basic models to be significantly inadequate for charge transport. For a time-dependent simulation, the displacement current is calculated along with the steady-state drift-diffusion components and included in the structure and the output

files. The expression for the displacement current is given by: $J_{dis} = \varepsilon\left(\frac{\partial E}{\partial t}\right)$, where E is the effective electric field in the system.

2.3.3.1 Poole-Frenkel Mobility Model

The Poole-Frenkel (PF) effect is explained as the lowering of the potential barrier of an electron in an electronic solid such as the organic semiconductor or an insulator in the presence of an external electric field[12]. This phenomenon is especially seen in disordered solids where the system is not described by free electrons moving in a self-consistent periodic field of force, but simply as a system of neutral atoms to begin with. When an atom is ionized, the electron moves freely in a surrounding medium consisting of neutral polarizable atoms and in the field of the remaining positive ion. Since this field is screened by the polarization of the surrounding atoms, the ionization energy is decreased and is proportional to the dielectric constant of the surrounding medium. In an external field, this energy is further decreased by a mechanism similar to the Schottky effect in the thermionic emission from metals. The lowering of the potential barrier is proportional to the square root of the external electric field and the effective conductivity of the material as a result of this phenomenon is given as $\sigma = \sigma_0 \exp[(e^3E/\varepsilon)^{1/2}/kT]$. The observed field dependence can be incorporated into an empirical relation for the hole or electron mobility of the form:

$$\mu_{npf}(E) = \mu_{n0} \exp\left[-\frac{\left(E_{n0} - \beta_n E^{\frac{1}{2}}\right)}{k_B T_{neff}}\right]$$

$$\mu_{ppf}(E) = \mu_{p0} \exp\left[-\frac{\left(E_{p0} - \beta_p E^{\frac{1}{2}}\right)}{k_B T_{peff}}\right]$$

where $\mu_{npf}(E)$and $\mu_{ppf}(E)$ are the PF mobility for electrons and holes respectively, μ_{n0} *and* μ_{p0} are the zero-field mobility for electrons and holes respectively, and E is the external electric field. E_{n0} and E_{p0} are the activation energy at zero electric field for

electrons and holes respectively. β_n and β_p are electron and hole PF factor respectively[13,14]. Based on the majority charge carrier contribution the PF model can be defined for electrons or holes or both.

2.3.3.2 Singlet and Triplet Exciton Generation

The primary process for generation of photocurrent in an organic photovoltaic device is the generation of bound electron-hole pairs called excitons by absorption of energy from the incoming optical electric field (wavelength ≥ bandgap of semiconductor). Once created, the exciton has a lifetime determined by rate of recombination through radiative (governed by singlet excitons) or non-radiative (governed by triplet excitons) decay or by dissociation into free charge carriers. Charge collection is possible only by the dissociation of the exciton into free charge carriers. The dissociation can be forced by an electric field or by interaction of the excitons with interfaces, impurities, or defects where charge transfer can occur. The diffusion range of the excitons is limited and only those excitons within a diffusion range of the dissociation sites will contribute to the photocurrent. The remaining fraction of excitons recombine via geminate or non-geminate pathways and is governed by the Langevin recombination model which is described in the next section.

Importantly for OLED simulation, continuity equations for singlet and triplet excitons can be solved individually along with the Poisson's and charge-carrier continuity equations to obtain the spatial and temporal distribution of excitons once they are generated[15]. The exciton continuity equations use the Langevin recombination term to include coefficients for radiative (r) and non-radiative (nr) decay, intersystem crossing (ISC), triplet–triplet (TT) annihilation, as well as singlet–singlet (SS), singlet–triplet (ST), singlet–polaron (SP), and triplet–polaron (TP) quenching mechanisms. Alternatively, where solar cell simulations are concerned, exciton dissociation can be included by specifying the singlet dissociation fraction.

Atlas can solve self-consistently the singlet and triplet exciton continuity equations along with the electron and hole drift-diffusion equations[16]. The spatial and

temporal singlet exciton densities are modeled and the equation also takes into account the exciton decay lifetime[17]. Once the exciton is generated, exciton dissociation needs to be modeled to obtain the charge collection efficiency of organic devices. This process is also governed by the Langevin model and considers the exciton binding energy and the electron-hole separation distance. At any given time, the exciton distribution can be obtained based on the charge generation model used. Some examples of the implementation of this approach includes obtaining the external quantum efficiency in organic solar cells[18] and electroluminescent devices[19].

2.3.3.3 Langevin Recombination Model

In dual carrier devices, two major contributions to charge transport study are the presence of recombination and charge neutralization processes. In molecular solids, where charge transport is of a hopping nature, majority of the recombination events proceeds on a time scale less than that of the geminate pair dissociation. This happens because the mean-free path of the generated charges is of the order of the lattice spacing and the exciton is of Frenkel type[20,21]. As a result, the bimolecular recombination process is diffusion controlled as given by the Langevin model[22,23] and follows the equation $\gamma/\mu = e/\varepsilon\varepsilon_0$, where γ is the bimolecular recombination rate constant and μ is the sum of the carrier mobilities. Main examples of this process are trap-assisted recombination, non-geminate recombination and Auger recombination in organic solar cells[24].

The Langevin model is used to account for the recombination of photo-generated charge carriers in organic photodiodes. In Atlas, the Langevin model is defined by two equations:

a) The Langevin recombination rate coefficient is given by:

$$r_L(x,y,t) = A.LANGEVIN\,\frac{q[\mu_n(E) + \mu_p(E)]}{\varepsilon_r\varepsilon_0}$$

b) The Langevin recombination rate is given by:

$$R_L(n,p) = r_L(x,y,t).(np - ni^2)$$

When enabled, the Langevin recombination rate is included in the recombination terms in the carrier continuity equations.

2.3.4 Numerical Methods and Iteration Parameters

Different combinations of models require the simulator to solve up to a maximum of six equations. Three generic numerical methods are present to converge to the required solution based on the nature of the equations: (a) decoupled (Newton), (b) fully coupled (Gummel) and (c) Block, which involves both the previous methods. The Newton method solves for each unknown in turn keeping the other variables constant, repeating the process until a stable solution is achieved. The Gummel method solves the total system of unknowns together. The Block method solves some equations fully coupled while others are de-coupled. All the methods used in Atlas solve by self-consistent iterations which involve initial guesses and have to be chosen based on convergence limitations[25]. Similarly, based on the convergence of a given equation the number of iterations can be varied to obtain the best tolerance limit for the solution.

2.3.5 Light Incidence

Simulations involving optoelectronic properties are solved by the Luminous module in Atlas[26]. It calculates the optical intensity profiles within the semiconductor device. The intensity profiles are then converted into photogeneration rates, which are directly integrated into the generation terms in the carrier continuity equations. The optical source is modeled as a collimated beam either using ray optics or by finite-difference-time-domain (FDTD) techniques. A transfer-matrix method (TMM) which is one of the simplest ways to model the wave-front of electromagnetic radiation is used in this thesis[18]. A file comprising the intensity of photons for visible wavelengths for AM 1.5 radiation is invoked via a function during the program to solve for the photodiode response.

2.3.6 Bias Conditions: Static and Transients

We calculate DC, small signal AC, and transient solutions for the simulated devices. Obtaining solutions is similar to setting up parametric test equipment for device tests. The voltages on each of the electrodes in the device is defined. Atlas then calculates the current through each electrode. It also calculates spatial and temporal internal quantities, such as carrier concentrations and electric fields which are difficult or impossible to measure.

In all simulations, the device starts with zero bias on all electrodes. Solutions are obtained by stepping the biases on electrodes from this initial equilibrium condition.

2.3.7 Reading the Output

Specific to Atlas, the solutions obtained at each voltage bias by solving the semiconductor equations is saved in a *.log file. All the terminal semiconductor characteristics such as J(V) and C(V) can be extracted and plotted in TonyPlot (which is the inbuilt plotting software) from the *.log files. Atlas also stores structure files (*.str) which saves the device structure with all its regions. The *.str file also saves the spatial charge and field distribution characteristics along with user-defined mesh and beam parameters.

2.4 Simulation of Organic Devices: An Example

In this thesis, two main semiconductor devices are considered, the polymer FET (PFET) and the organic photodiode (OPD). As an example of compact numerical simulation in Atlas, the standalone PFET and OPD are considered here before simulating their integrated structure in the form of an image sensor pixel in Chapter 4. Subsequently, a new transistor architecture which is the vertical transistor is simulated for its device characteristics in Chapter 5.

2.4.1 Polymer Field-Effect Transistor

A low voltage operating PFET has been studied in this thesis. The low voltage operation is achieved by making use of high k dielectrics like alumina and hafnia in

conjunction with a self-assembled monolayer which reduces leakage. P3HT is used as the active layer for p-type charge transport. The device structure as simulated in Atlas is shown in Figure 2.4(a). PF model for hopping transport is used in the simulation. The region and model parameters are specified in Table 2.1.

Table 2.1: Simulation parameters for a PFET

Name of the parameter	**Value[27,28]**
N_c, N_v of the P3HT layer	$2.5x10^{19}$ cm^{-3}
Bandgap, affinity of the P3HT layer	1.9 eV, 3.2 eV
Zero field hole and electron mobility	$4x10^{-4}$ $cm^2/V.s$
Field dependent mobility parameter (hole and electron)	0.1 $cm^{0.5}$ $V^{-0.5}$
Characteristic trap temperature	600 K[29]
Total trap density	10^{18} cm^{-3}
Permittivity of P3HT layer	3.3
Permittivity of SAM layer	3
Permittivity of Al_2O_3 layer	9.3
Poole-Frenkel Factor	$4x10^{-4}$ $cm^2/V.s$
Zero field activation energy	0.1 eV

Figure 2.4(d) and 2.4(e) display the output and transfer characteristics respectively of the simulated PFET. J(V) in the PFET is solved by gradual channel approximation which is conventional for channel lengths ~60 µm. The spatial current density is shown in Figure 2.4(b) at -5V (accumulation region of the PFET). The hole concentration which is maximum at 2-3 nm close to the dielectric-semiconductor interface as shown in Figure 2.4(c).

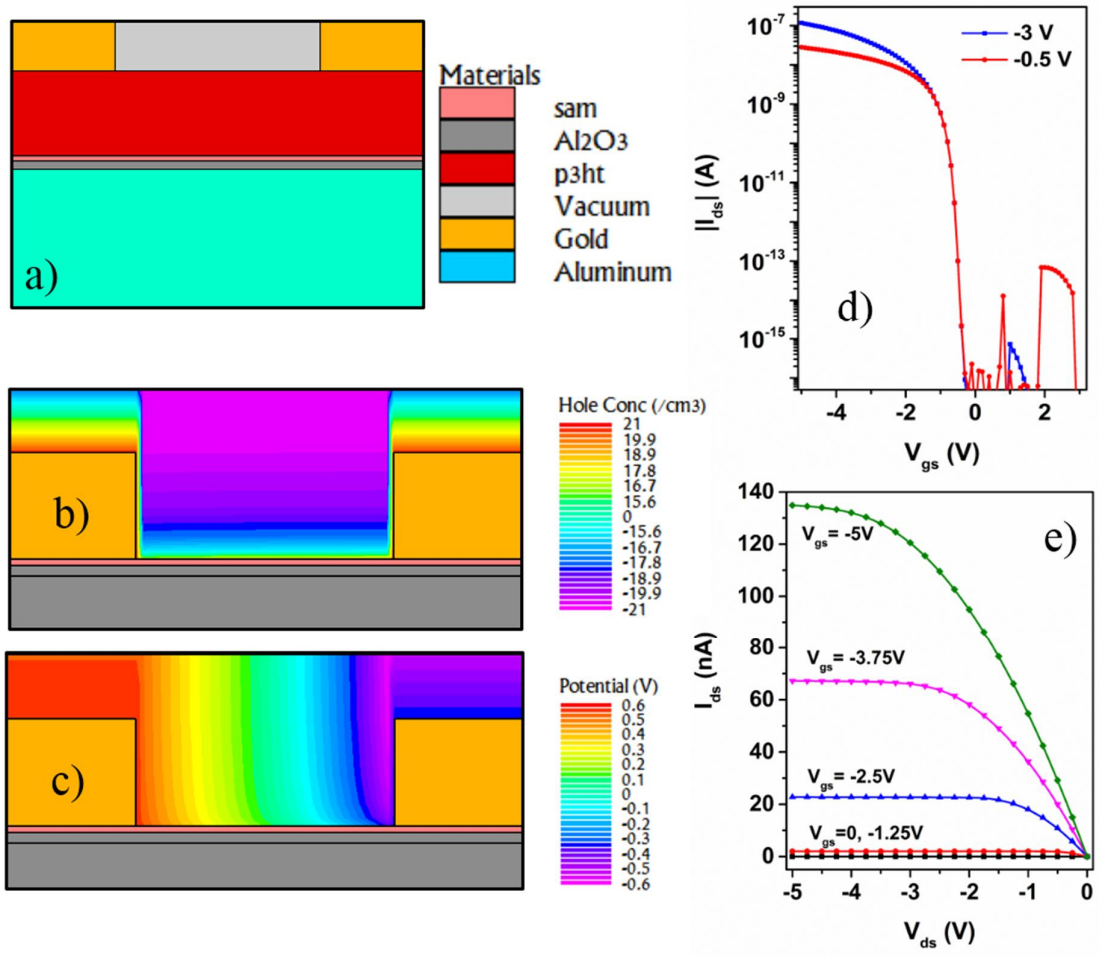

Figure 2.4: a) The PFET structure, b) hole concentration and c) potential distributions in the P3HT channel at V_{GS}= -5 V, V_{DS}= -5 V, d) transfer characteristics and e) output characteristics of the P3HT PFET.

2.4.2 Organic Photodiode

For the OPD, a 400 nm thick P3HT:PCBM bulk heterojunction blend is considered as the active layer. A PEDOT:PSS buffer layer is used for hole carriers and a ZnO buffer layer is chosen for electrons (Figure 2.5(a)). Langevin theory of charge recombination is used to account for the process of formation of excitons to dissociation into free charges. Suitable parameters for the P3HT:PCBM blend are shown in Table 2.2. Simulating a BHJ in Atlas is done via a single layer which includes properties of the hole and electron transporting materials. This is feasible since the variation in the two materials processing parameters is minimal as they are cast from

the same solution. Differences between P3HT and PCBM are only due to mobility parameters which are added individually in the simulation.

Table 2.2: Simulation parameters for an OPD.

Name of the parameter	Value[16,30]
N_c, N_v of the BHJ layer	$1x10^{21}$ cm^{-3}
Bandgap, affinity of the BHJ layer	1.34 eV, 3.3 eV
Zero field hole and electron mobility	$2.5x10^{-3}$, $3x10^{-4}$ $cm^2/V.s$
Permittivity of the organic layer	3.3
Singlet diffusion length	20 nm
Exciton binding energy	0.28 eV
Singlet radiative decay lifetime	10^{20} s
Fraction of singlets formed during Langevin recombination	1.0
Singlet non-radiative decay constant	$1.82694x10^6$

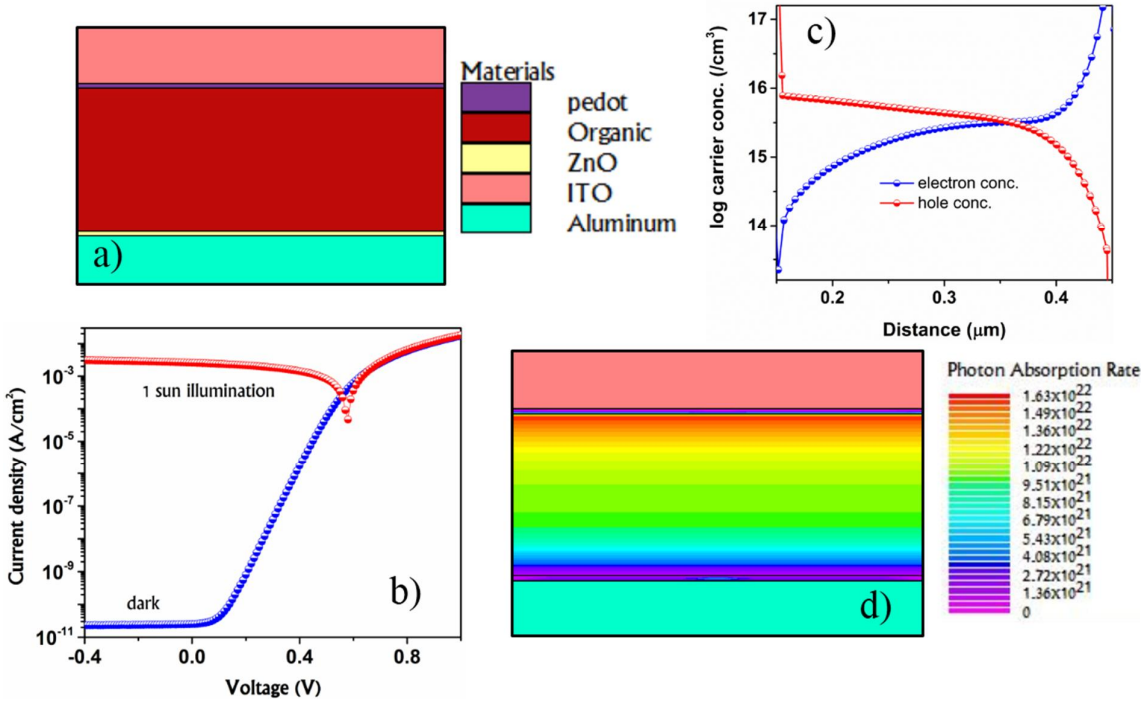

Figure 2.5: a) Structure of an OPD with P3HT:PCBM as the photoresponsive layer, b) Dark and light J(V) characteristics of the OPD, c) charge carrier concentrations in the BHJ after illumination, and d) Photon absorption rate in $/cm^3.s$ in the BHJ upon illumination.

Light is incident on the device from the ITO side. TMM for light propagation through the different layers is utilized to take into account thickness dependent parameters of the layers. The photon absorption rate shows an exponential dependence in the BHJ layer with negligible absorption in the buffer layers. The results of the simulation can be obtained as J(V) characteristics as shown in Figure 2.5(b). Several other parameters such as carrier concentration (Figure 2.5(c)), singlet exciton density and electron/hole quasi fermi levels to name a few can also be extracted from their respective 2D distributions.

2.5 Summary

Atlas forms a strong, supportive tool for semiconductor device research. With the incorporation of material specific models, all charge generation, recombination and transport processes can be quantitatively studied for better understanding of complex, novel structures. Organic models such as Poole-Frenkel and Langevin models provide a strong base to predict properties of organic semiconductor devices so that novel architectures can be realized. Using the reliability of solutions obtained for an OPD and PFET, two hierarchical structures are studied in this thesis: a) a solution processed monolithic organic image sensor pixel in Chapter 4, and b) an organic nano-triode (vertical transistor) in Chapter 5.

2.6 References

1 Silvaco. ATLAS [Online]. http://www.silvaco.com/products/device_simulation/atlas.html.

2 Lui, O. & Migliorato, P. A new generation-recombination model for device simulation including the Poole-Frenkel effect and phonon-assisted tunnelling. *Solid-State Electronics* **41**, 575-583 (1997).

3 Shim, C.-H., Maruoka, F. & Hattori, R. Structural analysis on organic thin-film transistor with device simulation. *IEEE Transactions on Electron Devices* **57**, 195-200 (2010).

4 Deledalle, F. *et al.* Understanding the effect of unintentional doping on transport optimization and analysis in efficient organic bulk-heterojunction solar cells. *Physical Review X* **5**, 011032 (2015).

5 Coropceanu, V. *et al.* Charge transport in organic semiconductors. *Chemical reviews* **107**, 926-952 (2007).

6 Takshi, A., Dimopoulos, A. & Madden, J. D. Simulation of a low-voltage organic transistor compatible with printing methods. *IEEE Transactions on electron devices* **55**, 276-282 (2008).

7 Fung, T.-C. *et al.* Two-dimensional numerical simulation of radio frequency sputter amorphous In–Ga–Zn–O thin-film transistors. *Journal of Applied Physics* **106**, 084511 (2009).

8 Mehraeen, S., Coropceanu, V. & Brédas, J.-L. Role of band states and trap states in the electrical properties of organic semiconductors: Hopping versus mobility edge model. *Physical Review B* **87**, 195209 (2013).

9 Shen, J. & Yang, J. Physical mechanisms in double-carrier trap-charge limited transport processes in organic electroluminescent devices: a numerical study. *Journal of applied physics* **83**, 7706-7714 (1998).

10 Pinto M.R., C. S. R., and Robert W. Dutton. PISCES2 - Poisson and Continuity Equation Solver. (Stanford University, 1984).

11 Neamen, D. *semiconductor physics and devices: basic principles.* 4th edition edn, 201-229.

12 Frenkel, J. On pre-breakdown phenomena in insulators and electronic semiconductors. *Physical Review* **54**, 647 (1938).

13 Horowitz, G. Organic field-effect transistors. *Advanced materials* **10**, 365-377 (1998).

14 Gill, W. Drift mobilities in amorphous charge-transfer complexes of trinitrofluorenone and poly-n-vinylcarbazole. *Journal of Applied Physics* **43**, 5033-5040 (1972).

15 Verlaak, S., Cheyns, D., Debucquoy, M., Arkhipov, V. & Heremans, P. Numerical simulation of tetracene light-emitting transistors: A detailed balance of exciton processes. *Applied physics letters* **85**, 2405-2407 (2004).

16 Koster, L. J., Smits, E., Mihailetchi, V. & Blom, P. Device model for the operation of polymer/fullerene bulk heterojunction solar cells. *Physical Review B* **72**, 085205 (2005).

17 Silvaco, I. in *Atlas User's Manual* 764-770.
18 Pettersson, L. A., Roman, L. S. & Inganäs, O. Modeling photocurrent action spectra of photovoltaic devices based on organic thin films. *Journal of Applied Physics* **86**, 487-496 (1999).
19 Paasch, G. & Scheinert, S. Simulation and modeling of C–V curves of OLEDs with trap states for the holes. *Synthetic metals* **122**, 145-147 (2001).
20 Lidzey, D. *et al.* Mapping the confined optical field in a microcavity via the emission from a conjugated polymer. *Applied physics letters* **71**, 744-746 (1997).
21 Lidzey, D. G. *et al.* Strong exciton–photon coupling in an organic semiconductor microcavity. *Nature* **395**, 53 (1998).
22 Albrecht, U. & Bässler, H. Langevin-Type Charge Carrier Recombination in a Disordered Hopping System. *physica status solidi (b)* **191**, 455-459 (1995).
23 Blom, P., De Jong, M. & Breedijk, S. Temperature dependent electron-hole recombination in polymer light-emitting diodes. *Applied Physics Letters* **71**, 930-932 (1997).
24 Proctor, C. M., Kuik, M. & Nguyen, T.-Q. Charge carrier recombination in organic solar cells. *Progress in Polymer Science* **38**, 1941-1960 (2013).
25 Silvaco, I. in *Atlas User's Manual* 76-79.
26 Silvaco, I. *Atlas User's Manual*. 517-611.
27 Scheinert, S. & Paasch, G. Interdependence of contact properties and field-and density-dependent mobility in organic field-effect transistors. *Journal of Applied Physics* **105**, 014509 (2009).
28 Scheinert, S. *et al.* Contact characterization by photoemission and device performance in P3HT based organic transistors. *Journal of Applied Physics* **111**, 064502 (2012).
29 Kim, C. H. *Physics-based compact modeling of organic electronic devices*, Ecole Polytechnique X, (2013).
30 Tang, Z. *et al.* A New Fullerene-Free Bulk-Heterojunction System for Efficient High-Voltage and High-Fill Factor Solution-Processed Organic Photovoltaics. *Advanced Materials* **27**, 1900-1907 (2015).

Solution Processable Ultra-Thin Dielectrics

Chapter 3

3.1 Introduction

Field effect transistors based on solution processed conjugated polymers/molecules have undergone tremendous progress in the recent years in terms of mobility[1], current amplification[2] and stability[3,4]. As their operational reliability improves, integrated devices such as active matrix backplanes[5,6], sensors[7] and flash memory[8] where FETs are the backbone for functional circuits become more feasible. Correspondingly, it is imperative that PFETs operate at low voltages and exhibit high switching ratios. It is evident that to obtain high-quality FETs, it is not only important to improve the organic semiconductor properties but to also use a gate insulator with high specific capacitance which can induce a substantial charge density at low gate voltages. This can be achieved either by employing a high-k insulator[9] or an ultra-thin, pin-hole free dielectric film[10]. Such materials must also exhibit high breakdown strength, low parasitic current leakage, low trap density, and high thermal stability. However, use of high-k materials results in the broadening of the DOS at the semiconductor-dielectric interface which increases the effective mass of the charge and reduces the mobility[11-13]. Similarly, ultra-thin dielectric layers are prone to high leakage current, easy rupture of films and low device reproducibility[10]. Ion gel dielectrics[14] and electrolytes[15] which constitute high-k dielectrics have been employed to achieve low voltage operation. However, movement of ions within the dielectric and/or electrochemical doping[16] ultimately govern their AC response eventually limiting their speed when they are incorporated into integrated circuits. Non-ionic materials such as amorphous inorganic dielectrics can be an alternative to achieve high performance PFETs. High-k oxides such as HfO_2, Al_2O_3, ZrO_2 and AlPO have seen the most prominent usage[17-20]. They yield high capacitance values even for thick films ($>$ 100 nm) which reduces leakage currents due to physical pin-holes. They also provide an excellent interface with oxide semiconductors as a result of low trap density[20], but a brief analysis of scientific literature in this field shows that high temperatures ($>$ 600 °C) need to be used to obtain defect (vacancy) free and pin-hole free films. As a solution to this, an ultra-thin hybrid dielectric layer was first

demonstrated by H. Klauk *et. al* [21] which used solution processed Al_2O_3 having k=9 in conjunction with a self-assembled monolayer which formed a energetically favorable interface with organic semiconductors. Careful design rationale from then on has led to more robust hybrid dielectrics such as the self-assembled Nano Dielectric (SAND) which enables p and n type FETs with mobility > 2 $cm^2/V.s$[22]. Recently, hybrid dielectrics have also shown promise in large scale circuits[7,8] making them an ideal combination of facile processing and high performance.

In the pursuit of obtaining high performance dielectrics, this chapter details out the work in three sections. The first section outlines a general fabrication process to obtain hybrid dielectrics for low voltage PFETs. In the second section, small molecule dielectrics which have not been explored so far are studied for their potential PFET applications. Finally, we also study the effect of a composite dielectric to improve the dielectric strength, polarization magnitude and mobility of PFETs.

3.2 Device Fabrication

All the devices were fabricated on glass substrates. The substrates were cleaned using wet chemical techniques by the following procedure before any device fabrication.

I. 10 minutes sonication in surfactant and de-ionized water.

II. Rinsing and sonication in di-ionized water for 10 minutes to wash off excess surfactant. This removes dirt and loosely bound contaminants.

III. Sonication in a mixture of acetone, isopropyl alcohol and chloroform for 10 minutes. This removes grease and oil-based contaminants.

IV. RCA treatment: Dipping the substrates in a mixture of ammonia, hydrogen peroxide and water (1:1:4) at 120 °C for 20 minutes. This removes metallic and organic contaminants.

V. Blow drying using compressed air and mild air plasma treatment for 10 minutes. This removes left-over carbon contaminants leaving a clean, contaminant-free (hydrophilic) surface.

3.2.1 Two Terminal Devices

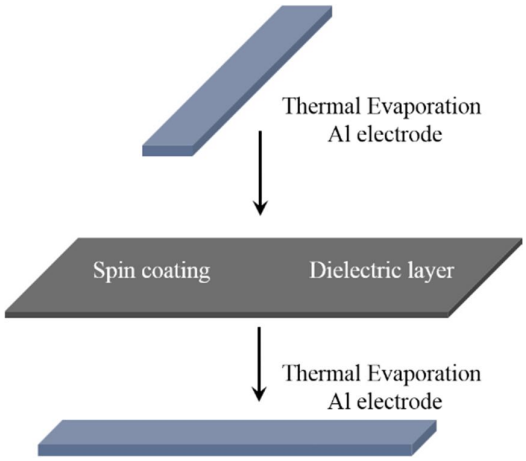

Figure 3.1: Schematic showing MIM structure device fabrication.

For capacitance-voltage and hysteresis measurements, metal-insulator-metal (MIM) devices were fabricated as shown in Figure 3.1 with the dielectric material sandwiched between two aluminum electrodes. The fabrication procedure involved coating of aluminum electrodes (10^{-6} mbar, 1 Å/s, 40 nm thick) on cleaned glass substrates and then introducing the insulator thin films followed by depositing the second aluminum electrode (10^{-6} mbar, 1 Å/s, 40 nm thick) by physical vapor deposition (PVD).

3.2.2 Three Terminal Devices

PFETs were fabricated for charge transport measurements. All the spin coated layers were formed in a N_2-filled glove box whereas the metal electrodes were obtained by physical vapor deposition (PVD). 40 nm thick patterned aluminum bottom gate was coated by PVD on cleaned glass substrates. Subsequently, the dielectric layers were coated by an optimized procedure to obtain the desired phase and thickness. Polymer thin films were then introduced on these substrates and annealed under conditions essential for obtaining ordered and crystalline structures. The FET was completed by coating a 40 nm thick (10^{-6} mbar, 1 Å/s) gold source-drain electrode after carefully aligning the mask on the gate electrode. The experimental results represent typical median responses arrived from measurements on large (~ 20 devices

from each batch) number of devices. An illustration of PFET fabrication is shown in Figure 3.2 alongside an optical image of a completed PFET

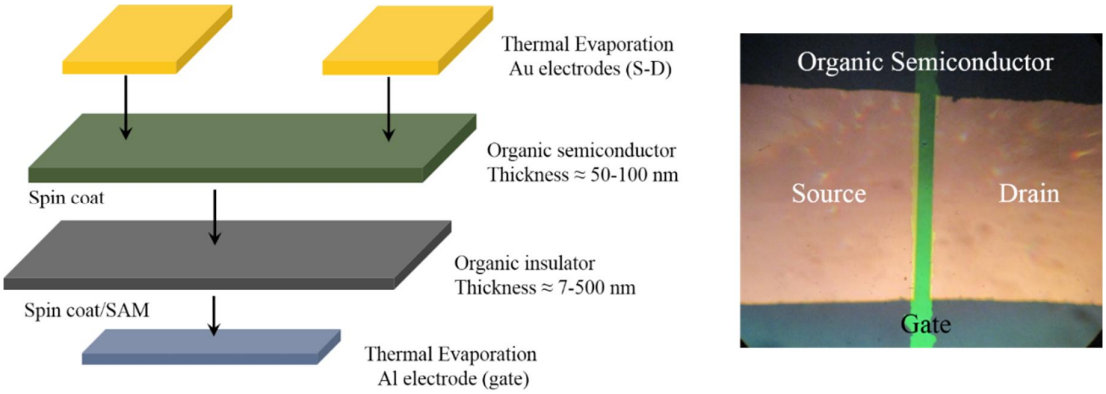

Figure 3.2: Schematic showing PFET fabrication along with an optical image of a completed device.

3.3 Experimental Techniques

3.3.1 X-ray Diffraction Measurement

XRD measurements were performed using Bruker axis D8-Discover with Cu K-α source. Thin films samples were prepared on glass substrates and scans were performed in steps of 0.0045°.

3.3.2 Atomic Force Microscopy

Morphologies of TBD and composite thin film surfaces were obtained using a JPK Nanowizard 3 AFM. A non-contact mode cantilever with resonance ≈300 kHz and force constant ≈ 42 N/m was used to obtain the surface roughness and phase of the thin film.

Piezo response microscopy (PFM) was performed to obtain the local piezo magnitude (amplitude image) and domain nature (phase image) of ferroelectric thin films cast on a metal electrode. An Au/Cr coated cantilever having a nominal spring constant 0.2 N/m and resonance frequency of 13 kHz was used to obtain the vertical piezo response. The samples were grounded during each measurement while a nominal drive voltage of 3 V was applied to the cantilever.

Force modulation AFM was performed using a contact mode cantilever with resonance ≈75 kHz and force constant ≈3 N/m. A modulation drive frequency ≈28 kHz, less than half the free resonance was used to map the changes in the local elastic modulus of the surface.

3.3.3 Electrical Characterization

Capacitance-voltage measurements on MIM devices and FET characterization was performed using a Keithley 2400 Semiconductor Parameter Analyzer (SCS). Switching measurements were performed by applying a pulsed voltage of ΔV_{GS} = -20 V to the gate electrode of the FET using the K-Pulse card in the SCS, while maintaining V_{DS} = -30 V. The output voltage was measured across an external series resistor (10 kΩ) using a Tektronix MDO3024 200 MHz oscilloscope.

Thin film P(E) loop measurements were performed using the Radiant Technologies Precision Feroelectric Tester. Composite and pristine P(VDF-TrFE) films were sandwiched between two aluminum electrodes and the hysteresis curve was measured between +/- 100 V at varying frequencies.

3.4 Hybrid Ultra-Thin Dielectrics

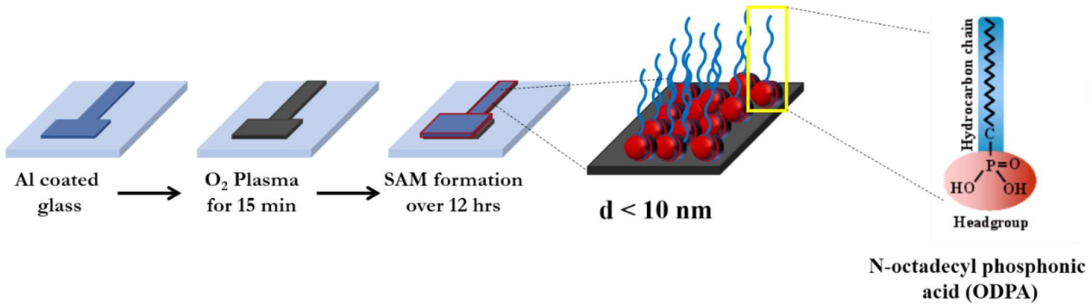

Figure 3.3: Schematic showing hybrid dielectric layer formation.

Solution processed amorphous oxide films are being widely used as thin film dielectrics, however, to utilize an oxide layer as a PFET compatible dielectric, the annealing temperature must be reduced to < 200 °C. An HfO_x dielectric layer, in the presence of a hydrolyzing agent, is obtained from $HfCl_4$ with the removal of HCl during annealing. We observed that formation of the HfO_x layer begins by nucleation

at several sites on the substrate. The presence of oxygen leads to Ostwald ripening of the nuclei leading to a semi-continuous network of HfO_x. It is well known from literature that the reaction to form oxides is highly dependent on the number of –OH groups present on the surface. High temperatures are necessary for the nucleation sites to grow in order to form a continuous layer[20]. We achieved this by annealing the film at a low temperature of 150 °C for one hour in ambient and subsequently exposing it to oxygen plasma for 20 minutes which aided in the growth of interconnected islands of HfO_x. The HfO_x surface morphology and phase scanned in non-contact mode AFM is shown in Figure 3.5(a) and (b) respectively. Alternatively, a self-grown Al_2O_3 layer was also used as an ultra-thin dielectric. A freshly deposited aluminum coated glass substrate was exposed to pure oxygen plasma for 20 minutes to increase the thickness of the nascent oxide layer.

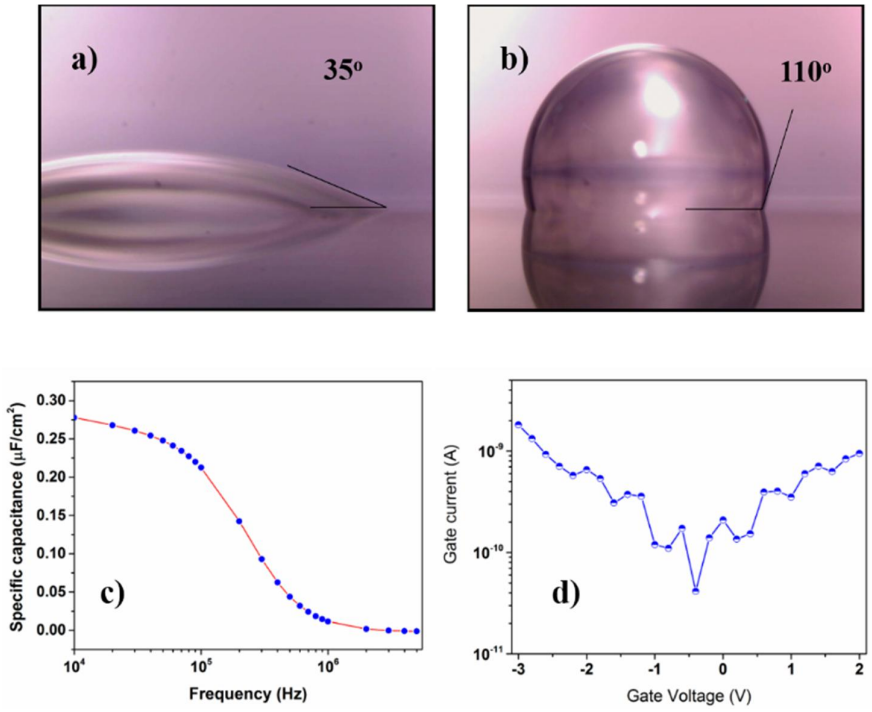

Figure 3.4: Contact angle on a) oxide layer and b) after SAM formation on the oxide layer, c) C(f) measurement and d) leakage current for the hybrid dielectric.

The films formed after low temperature annealing or from oxygen plasma treatment suffer from high trap density and high leakage currents respectively. With

the formation of a dense self-assembled monolayer (SAM) of an organic molecule just a few nanometers in thickness on the oxide layer, the leakage currents can be drastically reduced without compromising on the high capacitance. 3 mM octadecyl phosphonic acid (OPA) was dissolved in an ethanol solution and the oxide coated substrates were immersed in the pre-heated OPA solution for 12 hours at 70 °C. The phosphonic acid head group binds electrostatically to the surface of the dielectric and the octadecyl chain stands vertically due to its hydrophobic nature. The procedure for obtaining the hybrid layer is shown by an illustration in Figure 3.3. A dense monolayer of SAM is formed with a hydrophobic surface as confirmed from the change in contact angle from Figure 3.4(a) to (b). Thus we obtain hybrid layers which provide excellent mechanical, electrical and environmental durability of the inorganic material as well as mechanical flexibility and tenability of organic materials[23,24].

3.4.1 Electrical Characterization

Capacitance-voltage measurement on MIM devices employing the hybrid dielectric layer exhibits high specific capacitance with an effective ε'=3 for an effective thickness of 10 nm and leakage currents in the nA regime (Figure 3.4(c),(d)). Such a magnitude of capacitance is noted only for Debye layers in electrolytes. The roll-off frequency is ~100 kHz which is two orders higher than electrolyte dielectrics (~1 μF/cm^2) and can be improved further if the oxide layer is annealed at higher temperatures.

PFETs were fabricated using the hybrid dielectric. Polymer active layers (50 nm) PBTOR and DPP-DTT were spin coated from a 5 mg/ml solution in chlorobenzene at 1000 rpm for 1 min. The active layers were annealed in nitrogen atmosphere at 110 °C for 30 mins. This was followed by coating gold source-drain electrodes to complete the device fabrication. The channel lengths for the devices were chosen depending on the dimensions of the gate electrode to obtain minimum overlap and extremely low parasitic capacitance (1 pF/cm^2). The channel width (W) was 1 mm for the PFETs. The PFETs with SAM dielectric operate at V_{GS} = -3 V with well-defined linear and saturation characteristics. The performance characteristics obtained from Figure

3.5(c) and (d) give an average hole mobility of 0.8±0.1 cm^2/V.s and a maximum ON-OFF ratio of 10^6.

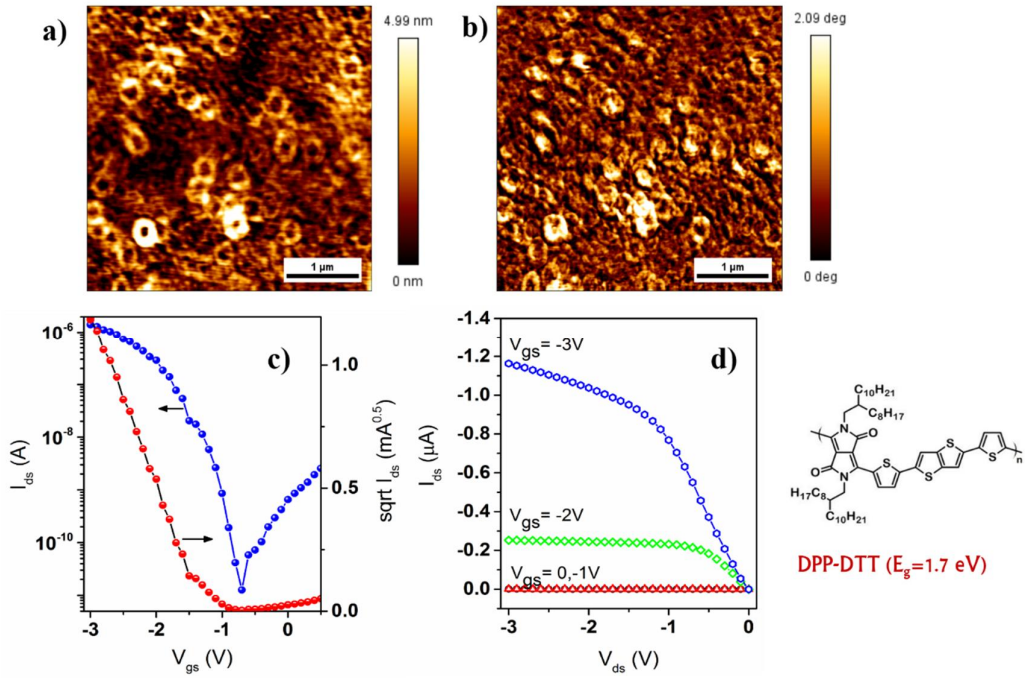

Figure 3.5: a) AFM surface morphology and b) AFM phase image of a spin coated HfO_x surface, c) transfer and d) output characteristics of a PFET using the hybrid dielectric.

3.5 Small Molecule Dielectrics

Another class of materials which can form PFET quality monolayers or thin multilayer dielectric films are small organic molecules[22,25,26]. Small molecules can be tailored more easily to obtain a high dipole moment and thus a high dielectric constant. In the solid state, however, molecular motion is severely restricted due to rigid bonds which limits its contribution to orientational polarization. Consequently, most of the materials tend to exhibit drastic reduction in dielectric constant upon solidification[27] or the crystalline nature of the material is not suitable for thin film applications. Two approaches can be adopted to obtain high-k materials based on their molecular motion. The first approach involves rational design of molecules to yield dense SAMs with precise thickness control as seen in the previous section. In

such films, the trade-off with the dielectric constant of the molecule is compensated by the overall thickness of the dielectric layer. A second technique involves retaining the dielectric constant of the molecule in the solid state so as to obtain high capacitance even at large areas and film thicknesses. In the second scenario, film quality is severely compromised due to crystallite formation (hence cracks) and there is no report to date on PFETs using solution processed, high-k small molecule dielectric thin films. This section focuses on incorporating both the approaches by chemically tailoring a well-known crystalline small molecule tetrabromopthalic anhydride (TBPA) whose structural characteristics is shown in Figure 3.6(a).

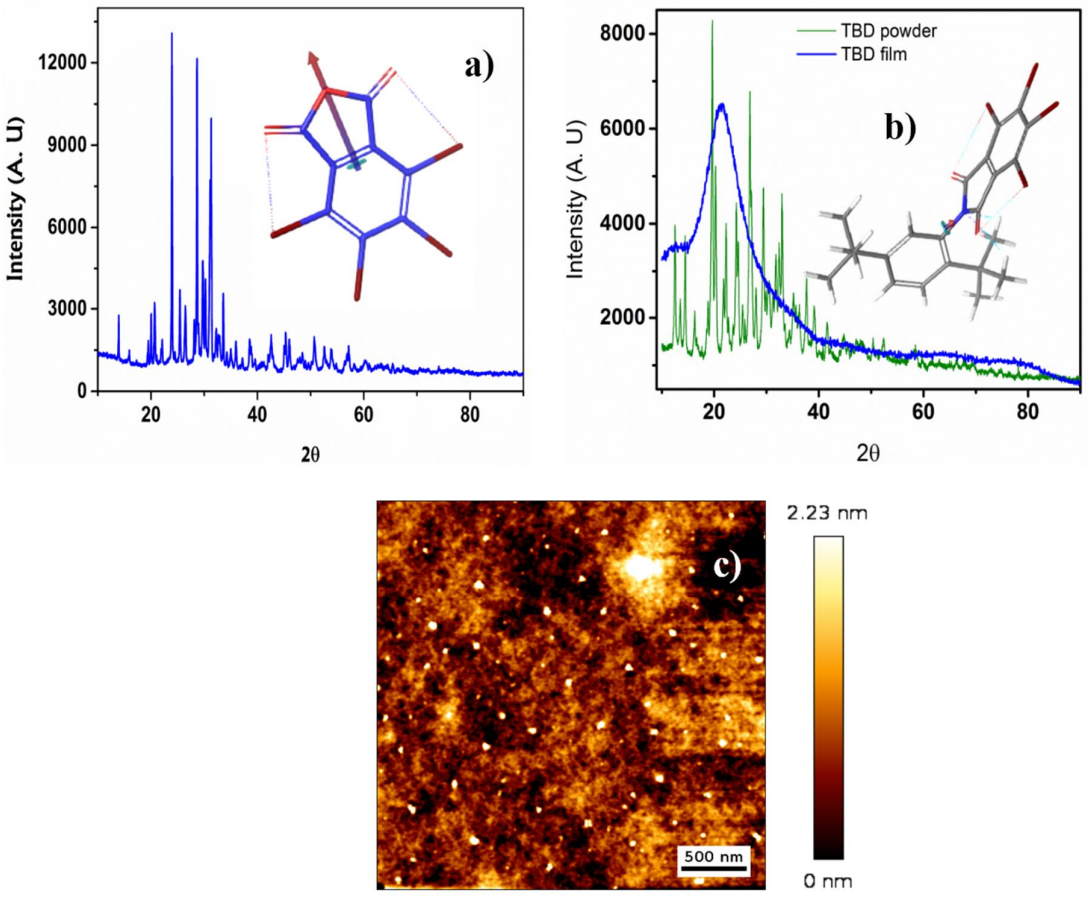

Figure 3.6: a) Powder XRD pattern of TBPA, b) Thin-film XRD (blue) overlaid on the powder XRD pattern (green) of TBD. In the insets of a) and b) are shown the chemical structures of the respective molecules along with the magnitude of their

dipole moment (arrow length). c) Morphology of TBD thin film surface obtained from AFM shows a maximum roughness ~ 2.2 nm.[1]

TBPA is a polar electron accepting molecule with a high dipole moment of 4.5 D[25]. It is a rigid and planar molecule which does not exhibit orientational polarization in its single component crystals. By introducing alkyl and aromatic substituents as a donor at the anhydride position, charge and dipole stabilization is achieved (0.5 D*) making the molecule non-polar. Alkyl chain substitution at the imide position using butyl, octyl and 2(octan-3-yl) groups (chemical structure not shown) improves solubility in common organic solvents with increasing alkyl chain length, however, crystallite formation persists due to the planarity of the overall structure. Imide substitution with 2,5-di-tertiary butyl aniline results in TBD (4,5,6,7-tetrabromo-2-(2,5-di-tert-butylphenyl)isoindoline-1,3-dione) (inset of Figure 3.6(b)) where N-C bond twist is induced due to the stearic hindrance between the tert-butyl moiety and the carbonyl oxygens. This leads to a dihedral angle* of 80° which breaks the rigidity of the imide bond. The intra-molecular non-planarity also disrupts crystal stacking and consequently, we believe, a thin film is obtained by solution processing which is amorphous as seen from the XRD pattern (Figure 3.6(b)) of a spin-coated TBD film. The AFM morphology (Figure 3.6(c)) reveals a continuous film with visibly small grain sizes and a surface that is extremely smooth with an RMS roughness < 0.4 nm which is two orders of magnitude lower than the surface roughness of P(VDF-TrFE) films (d_{rms}=15 nm).

3.5.1 Electrical Characterization of TBD

3.5.1.1 Dielectric Spectroscopy

To evaluate the applicability of TBD as a dielectric material, MIM capacitors were fabricated. The capacitor structure consisted of a TBD thin film (spin-coated from a 20 mg/ml DMF solution at 700 rpm for 1 min and annealed at 140 °C for 1 hour) sandwiched between two aluminum strips (~40 nm) which were coated by PVD.

* Calculations performed in Maestro-Materials Science Suite, Schrodinger Inc.

The effective thickness of the TBD film was ≈120 nm as measured by a Dektak Profilometer. The dielectric response to an external AC field (V_{rms}=30 mV) was studied by measuring its capacitance as a function of frequency.

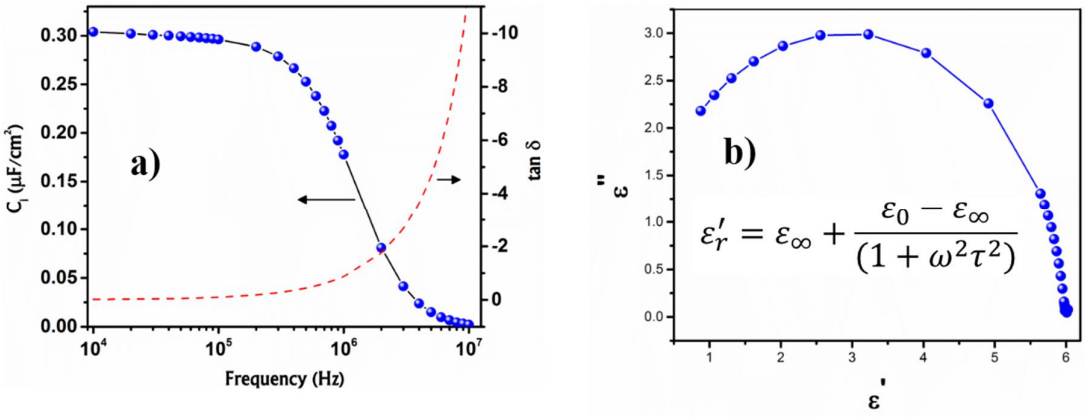

Figure 3.7: a) C(ω) curve of TBD capacitor. Right y-axis gives the dielectric loss of the material, and b) Cole-Cole behavior of TBD which shows a single relaxation time in the polarization process.

From Figure 3.7(a), the C(ω) of the MIM device occurs in the μF range which corroborates to a dielectric constant ε'≈6. It is to be noted that such a magnitude of capacitance is comparable to the Debye layer of electrolytes and is rarely observed in pristine polymer dielectric films. The loss tangent depicted by tanδ in Figure 3.7(a) reveals low dielectric loss implying good dielectric strength up to the MHz region. This is also confirmed by the J(V) plot in Figure 3.9(c) where we observed low leakage currents of the order of 0.1 nA.

The Nyquist plot in Figure 3.7(b) primarily helps in understanding the nature of the relaxation processes at the molecular level. A perfect semi-circle implies that TBD relaxations follow the Debye Model[28,29] which is the simplest model of dielectric relaxation generally observed in systems with non-interacting dipoles such as small molecules with simple/no branched moieties. The maximum value on the semicircle is ωτ=1 where τ is the relaxation time of the induced dipoles. We obtain τ=0.036 μs for the TBD capacitors which implies rapid dipole switching. Signatures of the relaxation process which occur as a peak in the loss ε″ and a step in ε′ show up in both frequency-

and temperature-dependent plots of the complex permittivity in dielectric spectroscopy.

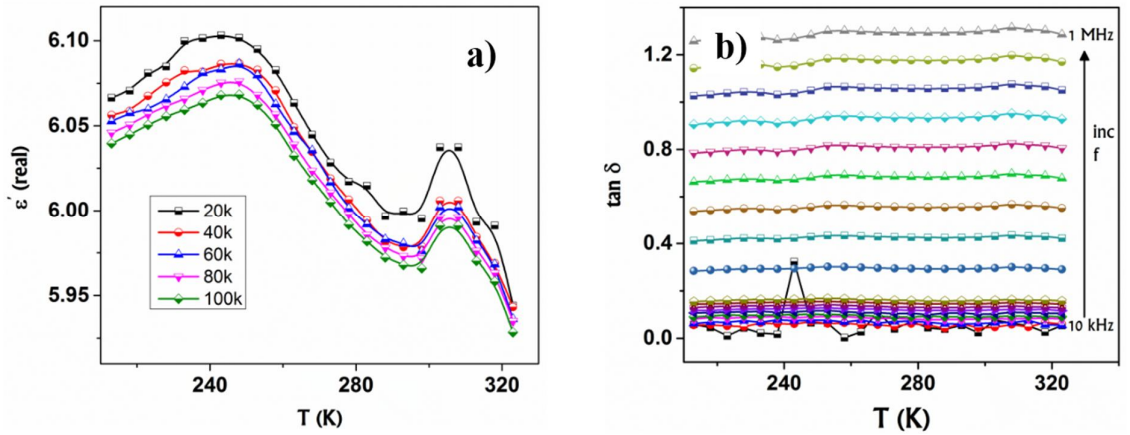

Figure 3.8: Temperature dependent C(ω) response in TBD. a) Dielectric magnitude and b) loss for frequency ranging from 10 kHz to 1 MHz.

At low field frequencies, molecular relaxation is faster than the applied field frequency which gives ε' > ε". Towards higher frequencies, where the AC field reversal and molecular reorientation time are comparable, the molecular dipoles contribute to the dielectric constant with a phase lag between the applied electric field and the induced orientational polarization. The phase lag results in the absorption of energy by the material, which is known as dielectric loss (ε") and the relaxation time at a given frequency and temperature can be obtained from the peak value of ε". From Figure 3.8(a), we observe a broad peak slightly below room temperature which can be assigned to the dipolar relaxation along the plane of the molecule (imide bond rotation) as it requires higher energy for rotation. The second peak observed around 240 K can be attributed to side group such as C-Br or/and C=O relaxations. Although the Debye model yields a single relaxation time, the broad nature of ε' occurs as a result of variations in relaxation times caused by local disorder quite common in molecular solids. Moreover, being in the range of the ambient temperature, the relaxations are also dominated by thermal fluctuations. The dielectric loss as a function of frequency as shown in Figure 3.8(b) does not show any peak in the entire temperature range studied. A linear shift in the loss magnitude with increase in

frequency points to the possibility of increase in random (kT) fluctuations of individual dipoles with frequency which causes the spread in the relaxation times. Measuring ε' and ε" at higher temperatures may shed some light on the relaxation phenomena in more detail. Consequently, by plotting the relaxation times as obtained from the Cole-Cole function at each temperature, the activation energy obtained is 0.025±0.01 eV which is same as the ambient thermal energy suggesting that the dielectric properties of TBD are dominated by fluctuations in the molecular dipoles at room temperature.

3.5.1.2 PFET Measurements

Bottom-gate, top contact PFETs were fabricated using TBD as the dielectric layer and DPP-DTT as the p-type semiconducting layer. TBD was spin-coated from a DMF solution as outlined above on a patterned aluminum (gate electrode) coated glass substrate. A thin layer of HMDS was spin-coated at 1000 rpm and annealed at 120 °C for 1 hour to passivate the surface and make it more hydrophobic. After spin-coating DPP-DTT as the active layer from a 5 mg/ml dichlorobenzene solution, gold S-D electrodes were deposited by PVD to complete the PFET fabrication.

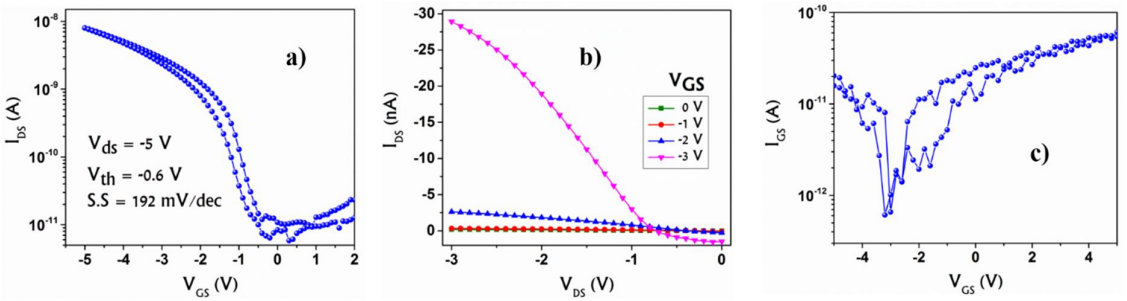

Figure 3.9: a) Transfer and b) output characteristics of a PFET using TBD as the dielectric layer and hole conducting DPP-DTT as the active material, and c) gate current in the PFET showing low leakage values in the PFET operating voltages.

Figure 3.9(a) and (b) shows the transfer and output characteristics respectively of the p-type PFET along with the gate leakage current in Figure 3.9(c). Thin films combined with high dielectric constant results in an operating voltage of V_{GS} = -5 V which is drastically lower as compared to PFETs using polymer dielectrics. The performance characteristics are obtained from the saturation region using the relation:

$\mu_{p,sat} = \frac{2L}{WC_i}(\frac{\partial\sqrt{|I_{ds}|}}{\partial V_{gs}})^2$ applicable at $|V_{GS}\text{-}V_T|<|V_{DS}|$. $\mu_{p,sat}$ obtained for DPP-DTT is 0.1 cm^2/V.s with an ON-OFF ratio of 10^4. A $V_T = |0.6\ V|$ suggests no trapped charges at the interface and a sub-threshold swing of 560 mV/dec implies fast polarization switching at a voltage as low as 1 V making it suitable for logic circuits. More than 20 devices were tested and although we obtained a 70% success rate, the lack of orthogonal solvents for the dielectric and semiconductor layer proved to be a major bottleneck to obtain high device efficiency.

3.6 TBD-P(VDF-TrFE) Composites

P(VDF-TrFE) is one of the most important ferroelectric (FE) polymers and as a typical semi-crystalline polymer, it is well known that the ferroelectric response is obtained mainly from the crystalline β phase whereas the amorphous regions do not contribute to FE significantly[30]. 30 wt% of TrFE in P(VDF-TrFE) results in repeating-unit isomorphism[31] as TrFE is similar to PVDF in chemical structure and size. Therefore, along with increasing the polar nature of PVDF, crystallinity significantly increases to >80 wt% as compared to 50% or less in the pristine PVDF polymer. The free volume available in the disordered regions of the polymer can be utilized to study the dependence of the ferroelectric property of P(VDF-TrFE) on its structural composition. When a homogenous blend of P(VDF-TrFE) and a small molecule is cast into a film, the ensuing thermodynamic and free volume conditions enable the small molecules to get distributed in the amorphous regions upon annealing the cast film. At low concentrations, the additive gets incorporated in between the polymer chains thereby increasing the interchain distance which eases dipole flipping in the presence of an external electric field[32]. As the additive concentration is increased, the aggregation of small molecules and its influence on the local polymer chain conformation and relaxation can be studied. We study the feasibility of high-k polymer composites for organic FETs by introducing TBD in small concentrations in the polymer matrix.

3.6.1 Ferroelectricity Measurements

MIM capacitors were fabricated using the TBD-P(VDF-TrFE) composite as the dielectric layer. Composite solutions were prepared by adding different weight percent (1%, 2%, 4%) of TBD in a 80 mg/ml DMF solution of P(VDF-TrFE) and stirred overnight at 50 °C to obtain a homogenous mixture. 30 µl of this solution was dispensed on Al coated substrates, spin coated at 900 rpm for 1 min and annealed at 140 °C for 2 hours. A minimum of 20 devices were tested for their P(E) and C(ω) characteristics at each TBD concentration in the composite between a voltage range of +/- 100 V at varying frequencies.

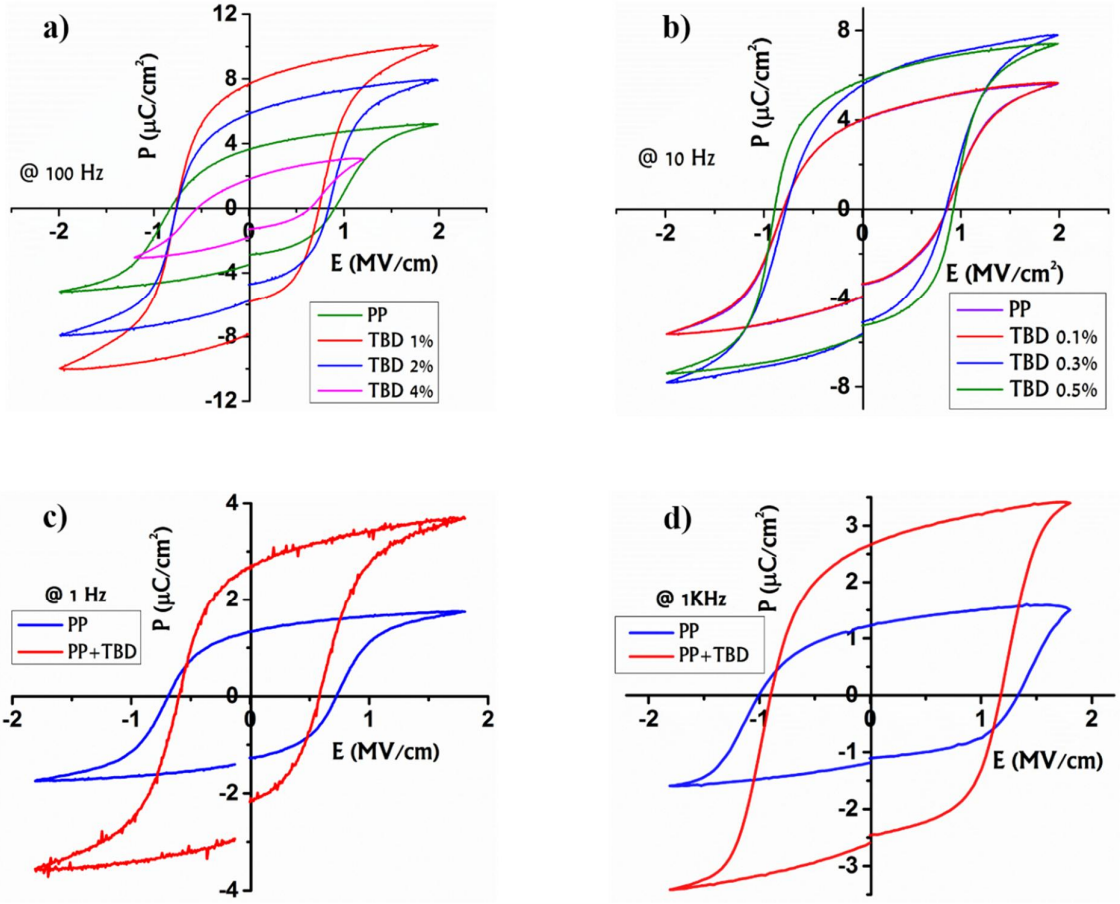

Figure 3.10: a) and b) P(E) loops showing comparison between pristine P(VDF-TrFE) and the composite at varying TBD concentration at 100 Hz, c) and d) P(E) characteristics for 1% TBD composite at 1Hz and 1 kHz respectively.

Hysteresis loops of pristine P(VDF-TrFE) and composites with different concentrations of TBD are shown in Figure 3.10. Instantly we observe that the P(E) magnitude starts increasing in the composite film as compared to the pristine polymer (PP) from 0.3% TBD concentration. The P(E) magnitude goes through a maximum for 1 wt% TBD composite (PV) with a marginal narrowing in the hysteresis loop. As the concentration of TBD increases beyond 1%, the magnitude and loop area decreases until leakage dominates the signal to give a resistive loop (not shown). The trend in P(E) magnitude suggests a strong correlation between the morphology of the composite and its electrical characteristics. In P(VDF-TrFE), the FE signature is a result of flipping of the C-F dipole on the zig-zag chain within a ferroelectric domain. The increased P(E) magnitude should, therefore, be due to increased chain mobility caused by reduction in intermolecular friction from its neighbors. Increase in interchain distance occurs if TBD at low concentrations gets accommodated between the P(VDF-TrFE) chains. Reduction in inter-chain friction also results in a plasticizing effect as seen in commercially viable plasticized polymers such as polyimide[33] and can be verified by comparing the local elastic modulus of PV and PP.

3.6.2 Bilayer Ferroelectric Measurements

Results from P(E) measurements on the composite film make it evident that the presence of TBD is favorable for enhancing the ferroelectric properties of P(VDF-TrFE) due to either morphological or relaxation changes in the composite. To confirm the thermodynamic nature of TBD incorporation in enhancing the P(E) magnitude, bilayer capacitors were fabricated in three structures. The first set of capacitors were fabricated by starting with a thin layer of TBD spin coated from a 15 mg/ml solution in DMF at 900 rpm and annealed at 140 °C for 1 hour on an aluminum electrode. Subsequently, P(VDF-TrFE) was coated from a 80 mg/ml DMF solution at 900 rpm for 1 min and annealed at 145 °C for 2 hours after which the counter aluminum electrode was coated. The second set consisted of capacitors with the polymer layer coated initially followed by the TBD layer using the same conditions as above. In the third set, P(VDF-TrFE) was sandwiched between two TBD layers to constitute the

dielectric layer. In the bilayer fabrication, firstly, the underlying layer dissolves when the second layer is spin coated. As a result, the two layers blend to form a composite layer. The P(E) magnitude for the three capacitor structures with comparison to PP is shown in Figure 3.11.

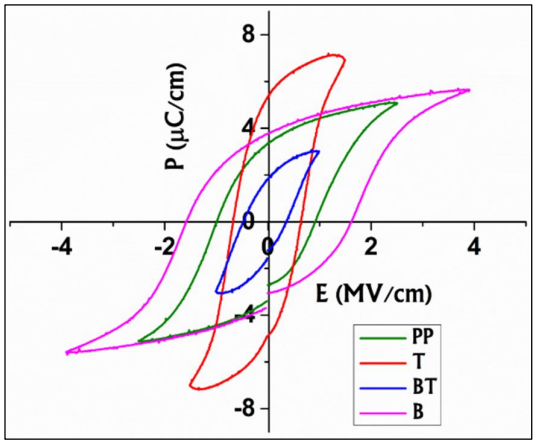

Figure 3.11: Hysteresis plots of bilayer dielectric based MIM capacitors. PP - pristine polymer, T - top TBD bilayer, BT - bottom and top TBD, B – bottom TBD.

From the graph, we see that composite formation from blending increases the saturation polarization magnitude as compared to PP which is observed from single solution blends also. In the sandwiched film, the concentration of TBD is approximately twice as higher compared to the bilayer films. As observed from P(E) loops of composites with high TBD concentration ($> 5\%$), P(E) magnitude drops due to increase in resistive losses in the film. Higher P(E) magnitude for the top TBD bilayer capacitor as compared to bottom TBD can also be speculated as the result of a more homogenous distribution of the TBD in the former composite upon blending. The results obtained from this study is consistent with the previous P(E) results which indicate that TBD is responsible for improved FE characteristics. Micro and macroscopic structural characterizations are performed to relate the structural changes to improved FE behavior in the composite.

3.6.3 Microscopic Characterization of the Composite

3.6.3.1 Surface Morphology

The surface morphologies of PP and the composite at varying TBD concentrations were compared by tapping mode AFM using a 300 kHz silicon cantilever. Representative images of the PP film (Figure 3.12(a)) and PV film (Figure 3.12(b)) surface are shown below. The grain-like morphology is clearly visible in PP and the grain size is calculated as ~85 nm. The RMS roughness of the surface reduced from ~19 nm in PP to ~13 nm in PV. Although the origin of reduction in roughness in PV is not understood as of now, we see from the table in Figure 3.12 that the FE grain size reduces when TBD is introduced even in amounts as small as 1%. Further, the average grain size increases only marginally with an increase in the spread of grain sizes when the concentration of TBD is further increased.

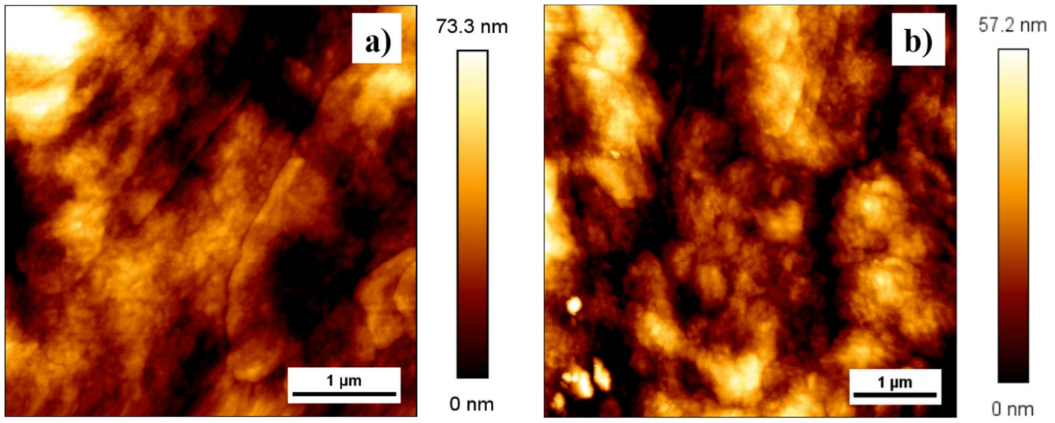

Weight percent of TBD in PVDF:TrFE	Domain size (nm)
0	82 ± 5
1.1	55 ± 6
2.2	62 ± 4
4.4	60 ± 10

Figure 3.12: a) PP and b) PV surface morphology images obtained from a tapping mode AFM height scan. The table gives a comparison of the FE grain size in the composite for varying concentrations of TBD.

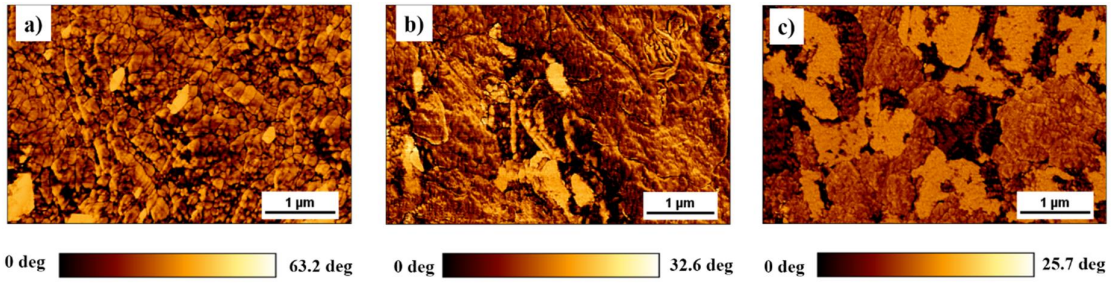

Figure 3.13: Phase images obtained from tapping mode AFM for a) PP, b) PV, and c) composite with 2.2 wt% TBD concentration.

The variations in phase for PP and PV (Figure 3.13(a) and (b)) is minimal with the grain dimensions being replicated from its morphology scan. Upon increase in the concentration of TBD to 2.2%, the phase separation is visible with distinct domains of TBD and P(VDF-TrFE) seen in Figure 3.13(c). It is clear from the large domain sizes of the two phases in Figure 3.13(c) that the eventual breakdown in the capacitor occurs due to pin holes formed at the boundary of the two phases when the pristine component domain size increases at higher TBD concentrations. The phase separation is kinetic in nature during the drying phase of the composite film. This happens due to the semi-crystalline nature of P(VDF-TrFE). If the concentration is kept low enough ($\leq 1\%$), TBD gets accommodated in the amorphous regions of the semi-crystalline matrix. To confirm the aggregation kinetics of TBD in a composite, an amorphous polymer PMMA+1 % TBD composite solution was cast into a film and the morphology obtained using AFM clearly shows a homogenous mixture of the two components (Figure 3.14) as opposed to phase separation in a semi-crystalline matrix.

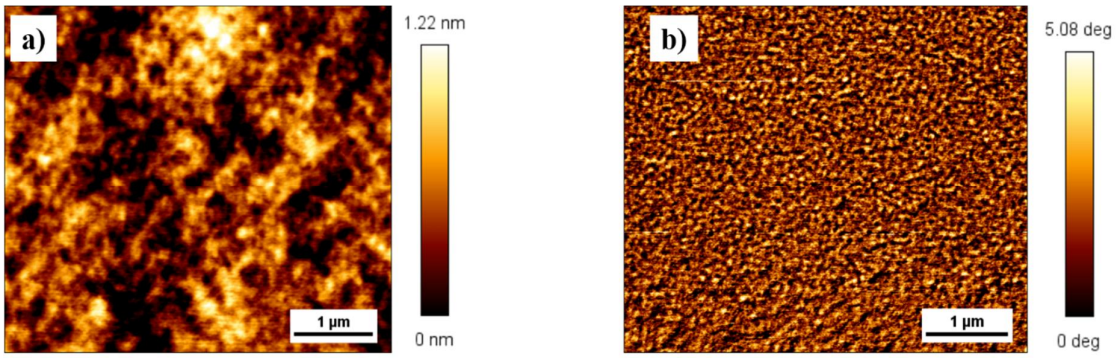

Figure 3.14: a) AFM Morphology and b) phase image of the surface of a PMMA+1% TBD composite

3.6.3.2 Force Modulation Microscopy

The plasticizing effect of TBD molecules at low concentrations is verified by measuring the local elastic properties of the composite surface using force modulation AFM. In this technique, a change in modulation amplitude of a cantilever in contact (Multi75-G cantilever) with the sample surface is recorded. The tip-sample interaction force causes the resonance amplitude to dampen for a soft surface and increase for a relatively hard surface[34]. Figure 3.15 shows the force amplitude images of the pristine polymer surface in comparison with the composite surfaces. We observe a decrease in the voltage amplitude from 10.6 mV in PP to 4.7 mV in PV which implies a decrease in the elastic modulus of the composite surface. For TBD concentrations $\leq 1\%$, all observations suggest a softening of the matrix surface suggesting the intercalation of TBD between the polymer chains. The increase in the voltage amplitude to 7.6 mV in Figure 3.15(c) for the composite surface (TBD concentration = 2%) maybe due to the onset of phase separation as suggested even in the decrease in P(E) magnitude.

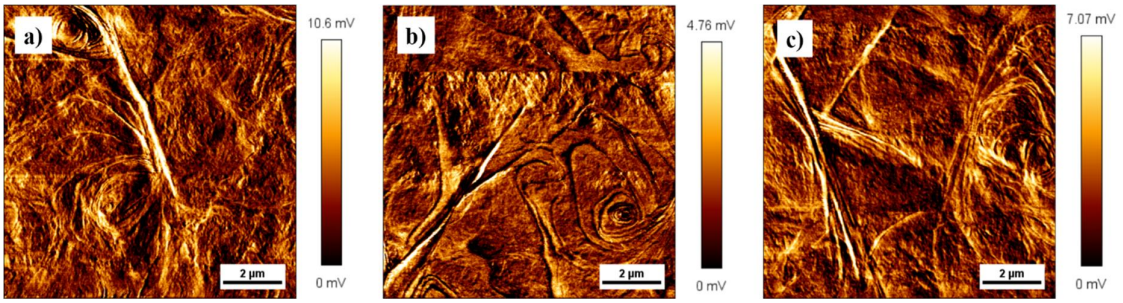

Figure 3.15: Force modulation AFM scans of a) pristine P(VDF-TrFE), b) 1% TBD:P(VDF-TrFE) and c) 2% TBD:P(VDF-TrFE) film surface (on glass substrates).

3.6.3.3 Piezo Response Microscopy

The dependence of P(VDF-TrFE) polymer chain packing and dipole orientation due to the presence of TBD is a clear indicator for the enhancement of the P(E) characteristics in PV. The local piezo response of the PV surface using Piezo

Response Microscopy (PFM) is also measured to observe the ferroelectric domain size in the composite in comparison to pristine P(VDF-TrFE). The vertical PFM amplitude gives a nanoscale insight into the polarization distribution within the FE domains by detecting their mechanical oscillations in response to the applied AC bias. The phase image of a PFM scan qualitatively explains the direction of orientation of the dipoles w.r.t the external field.

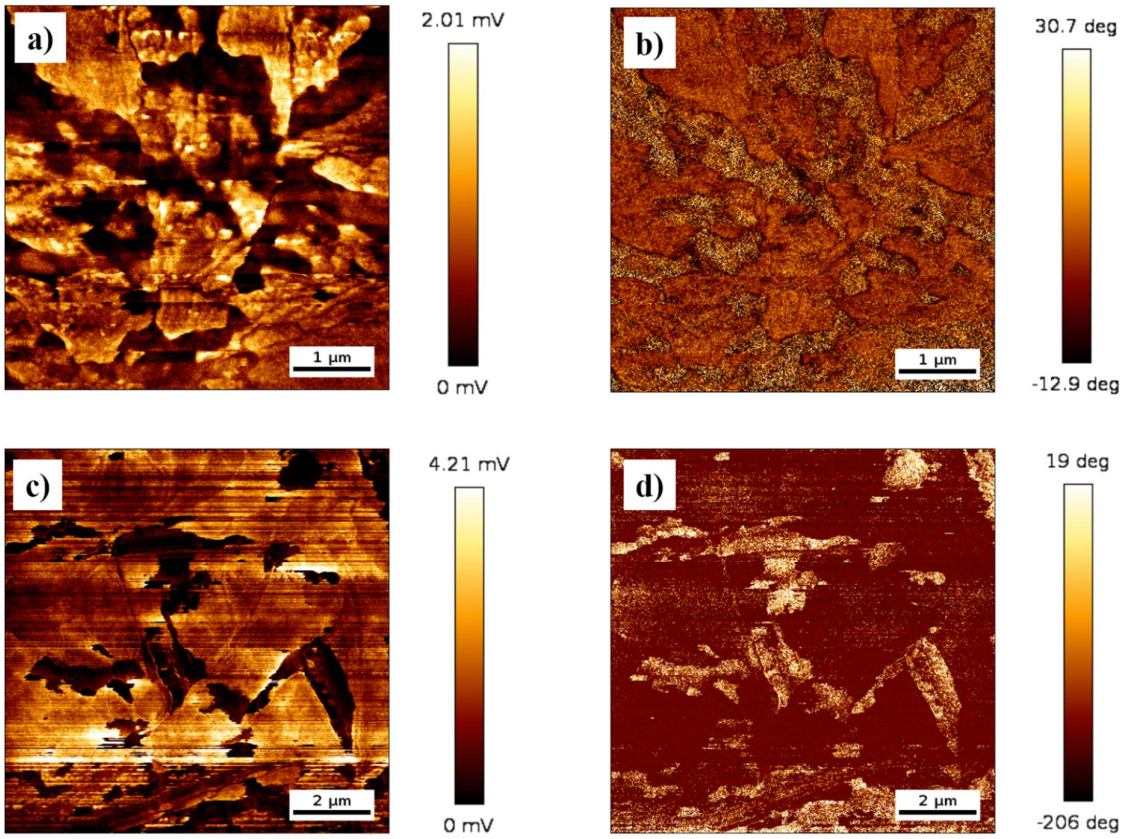

Figure 3.16: a) and c) Vertical PFM amplitude images for PP and PV respectively. b) and d) vertical PFM phase images for PP and PV respectively.

Analysis of the FE domain morphology in the amplitude image of PP (Figure 3.16(a)) shows domain sizes of the order of ~1 µm. Contrast variations in the vertical PFM phase image (Figure 3.16(b)) corroborates to most of the dipoles orienting parallel to the surface/in-plane w.r.t the electric field direction. Correlating the explanation of the plasticizing effect of TBD, the local piezo magnitude in PV in Figure 3.15(c) shows an increase in the FE domain size as a larger fraction of dipoles

are aligned parallelly for a low electric field. The phase image (Figure 3.15(d)) also confirms the dipole orientation in the FE domains with neighboring domains aligning almost 180° out of phase w.r.t each other. To understand the structural changes in more detail, we performed the thin film XRD of pristine FE and the composite with two concentrations of TBD.

3.6.4 X-ray Diffraction

The normalized XRD pattern in the pristine and composite thin film in Figure 3.17 reveals only the *all-trans* β phase peak of P(VDF-TrFE) which corresponds to 2θ=19.5°. XRD pattern analysis of P(VDF-TrFE) thin films has been studied previously and the presence of the obtained 2θ peak presumes the polymer chains to be arranged in a co-planar ziz-zag manner parallel to the substrate[30,35]. Addition of 1% TBD to the pristine polymer does not change the crystallinity of the domains significantly. As the concentration of TBD increases, signatures of TBD are seen in low intensities. There is no change, however, in the degree of crystallinity of the polymer matrix which confirms that TBD occupies the amorphous regions at low concentrations and a uniform blend is obtained. With increase in concentration, the propensity to phase separate can result in multiple low intensity XRD signatures. In summary, TBD does not change the morphology or crystallinity of P(VDF-TrFE).

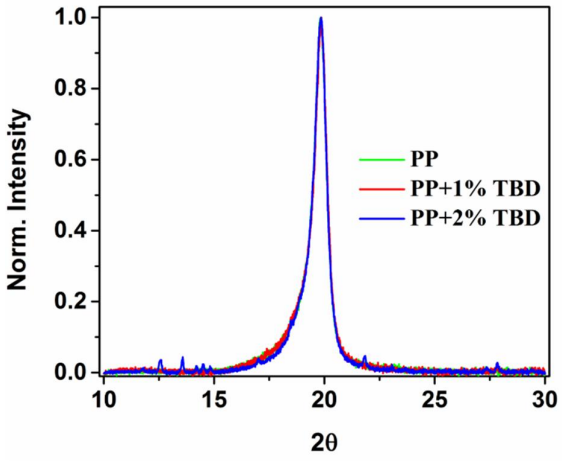

Figure 3.17: Comparison of the thin film XRD spectra of pristine P(VDF-TrFE) and the composite.

3.6.5 Dielectric Spectroscopy

Relaxation dynamics of both the components in the composite is obtained by dielectric spectroscopy. Figure 3.18 compares the Nyquist plots of PP and PV for C(ω) measurements performed at room temperature. PP and PV show a deviation from semi-circle behavior, common in polymers which exhibit multiple relaxation processes due to multiple side-chain and polymer backbone orientations[36,37]. Secondly, the high frequency response is improved in PV as compared to PP suggesting that the molecular dipoles reorient faster than the external alternating field due to freedom of rotation as an effect of increased interchain spacing. Frequency dependent chain relaxation dynamics of the composite can be studied by obtaining the temperature dependent dielectric response of the composite. The outcome of this experiment is shown for ε'(T) and ε"(T) in Figures 3.18(c) and 3.18(d) respectively.

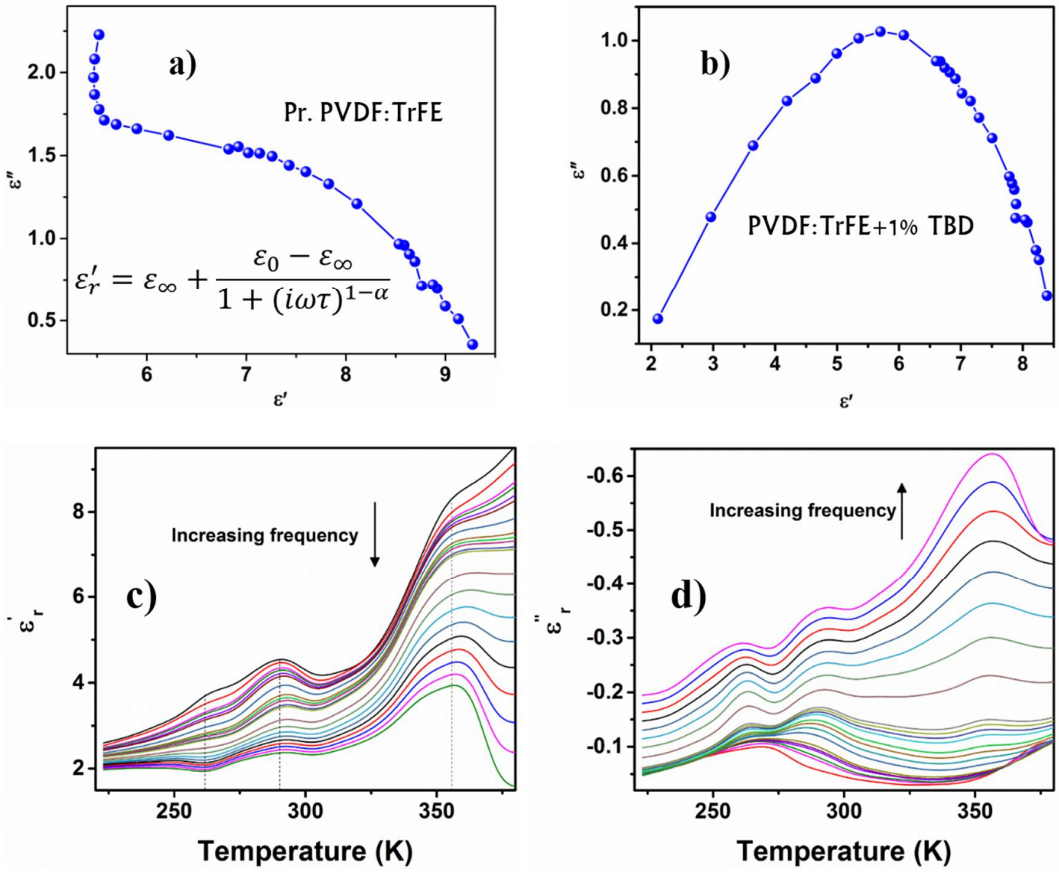

Figure 3.18: a) and b) Cole-Davidson behavior in PP and PV respectively. In the inset of a) is the Cole-Davidson equation, c) temperature dependent dielectric magnitude and d) loss for frequency ranging from 10 kHz to 1 MHz.

We observe three significant peaks in the high and low temperature regime. From the dielectric response of the pristine TBD film explained in the previous section, the low temperature peak which occurs at ~290 K can be assigned to TBD relaxation. This peak overlaps with the β phase transition peak of P(VDF-TrFE) which is known to occur in the 250-270 K temperature range[12,38]. Frequency dispersion in the two peaks indicates the thermal fluctuations in TBD relaxation which is quite pronounced in the pristine films as observed in Figure 3.8(a). The FE transition peak is observed at low frequencies as a shoulder at the Curie temperature (T_c) of P(VDF-TrFE). As the frequency increases, the T_c peak is pronounced. The increase in ε'(T) for low frequencies is attributed to Maxwell-Wagner-Sillars interfacial polarization which explains charge buildup at the interface of the crystalline and amorphous regions[33,39]. The space charge at the interface cannot follow the field frequency as it increases and subsequently in Figure 3.18(c) we see a drop in the ε'(T). The above-mentioned three transitions are also replicated in the ε"(T) graph where each transition becomes more resolved as the frequency increases and is overlaid by a linear shift indicative of thermal fluctuation dominated absorption losses. In PV, the interfacial polarization is suggested to result from the TBD-polymer boundaries and is expected to show a larger deviation in ε'(T) and ε"(T) as the concentration of TBD is increased due to component phase separation. Consequently, for T<Tc, a collective dipole alignment in the composite not only yields higher P(E) magnitude but also results in a favorable dielectric surface morphology for interfacial charge transport in PFETs.

3.6.6 Composite PFETs

PFETs were fabricated using PP and PV to evaluate the effect of TBD in interfacial charge transport. Both the films were spin coated on an aluminum gate electrode using the same procedures as two terminal capacitors. On the annealed dielectric films, a thin layer of HMDS was spin coated at 1000 rpm for 1 min and the

substrates were annealed for 1 hour. This was followed by spin coating DPP-DTT at 800 rpm for 1 min as the active layer from a 5 mg/ml dichlorobenzene solution. After annealing the substrates at 140 °C for 1 hour, gold S-D electrodes were coated to complete the PFET device fabrication. For each dielectric type, > 10 devices were tested to obtain a comparison between pristine and composite characteristics. The output and transfer characteristics of PP and PV are shown in Figure 3.19(a), (b) and (c), (d) respectively.

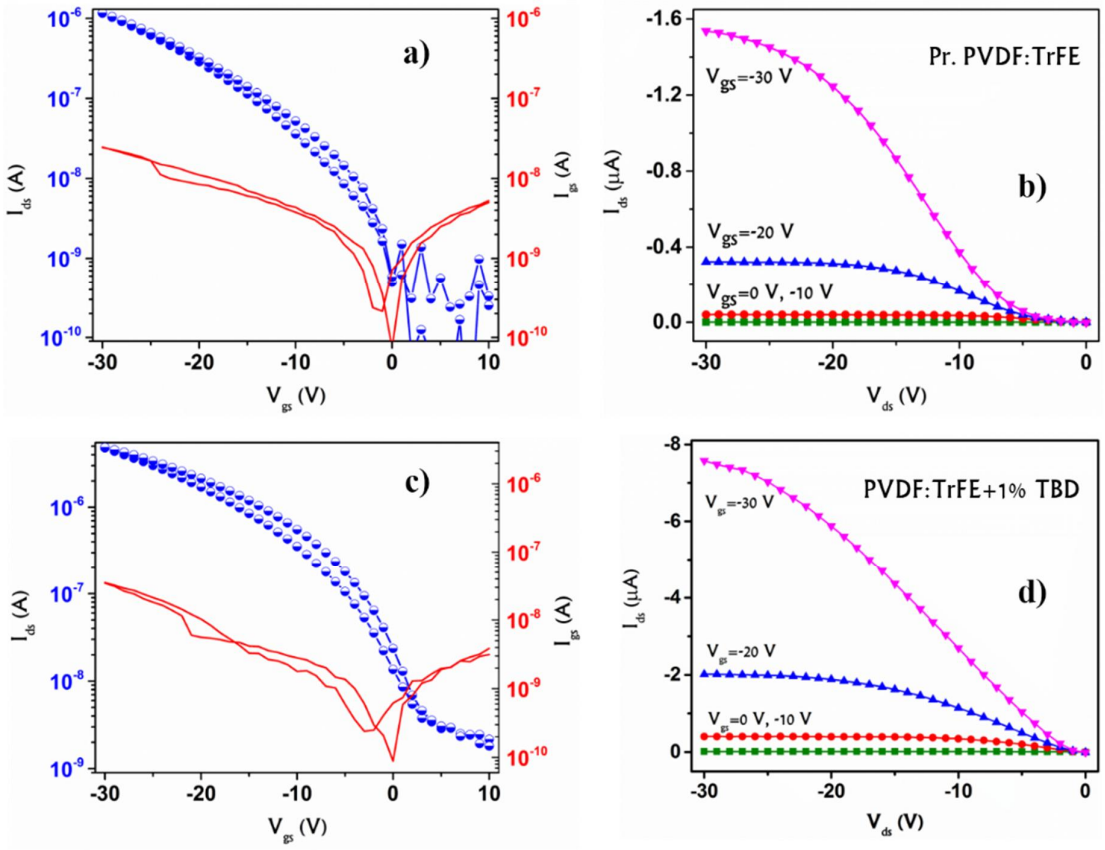

Figure 3.19: a) and b) PFET characteristics of PP, c) and d) PFET characteristics of PV using hole conducting DPP-DTT as the active layer.

PFETs fabricated from both the dielectrics yield similar operating voltage as the effective dielectric constant for PP and PV are of the same order. Difference in characteristics is observed in the $I_{DS,sat}$ of the two PFETs. PV PFETs show nearly one order higher saturation currents as compared to PP PFETs. The V_T of PV is also lower at 2.7 V as compared to -7.6 V in PP. The improvement in the $I_{DS,sat}$ and V_T

for PV can be clearly correlated to the increase of in-plane P(VDF-TrFE) dipoles which reduces disorder (hence narrows interface DOS) at the dielectric-semiconductor interface. Consequently, we also see an increase in the PFET mobility μ_{FET} by one order from 0.005 $cm^2/V.s$ in PV as compared to 0.08 $cm^2/V.s$ in PP. The structural analyses of the composite imply that the two components are non-interacting species and TBD only guides the molecular dipole orientation and FE domain formation. Considering the importance of high-k polymer dielectrics for PFET applications, the presence of TBD in P(VDF-TrFE) is very beneficial as it does not degrade the dielectric characteristics of the pristine polymer but reduces the fraction of random dipoles quite common in high-k polymer dielectrics.

3.7 Summary

Table 3.1: Comparison of commonly used dielectrics for PFETs with the two materials studied in this chapter.

	Material	Dielectric constant (ε')	Leakage current (J_{leak}) (A/m^2)	PFET operation voltage
	BCB	2.5	10^{-10}	80 V
	PMMA	3.6-4.5	10^{-8}	60-80 V
	P(VDF-TrFE)	6-8	10^{-8}	30-40 V
This work	Oxide+SAM	3-5	10^{-8}	< 3 V
This work	TBD	6-8	10^{-7}	< 3 V
This work	Composite	8-9	10^{-10}	< 30 V

This chapter details out strategies to obtain low voltage and high performance PFETs using three dielectric engineering strategies. Table 3.1 shows some basic parameters of commonly used dielectrics for comparison with the results obtained from this chapter. The first necessity to obtain low voltage operation is to use high-k dielectrics. Although, amorphous oxides monopolize this field in the conventional silicon industry, a trap-free interface for PFETs is difficult to achieve without high temperature processing. This was overcome by our first strategy of using a surfactant monolayer whose hydrophilic head passivates the oxide traps and the hydrophobic tail enables better adhesion of the organic semiconductor. PFETs using this hybrid

dielectric were processed at temperatures < 150 °C and operated at -2 V. The second strategy to obtain low V_T PFET operation involved a single-step, low temperature dielectric layer processing by utilizing a small molecule high-k organic dielectric TBD. Chemical modification of TBPA to introduce molecular dipole orientation in the solid state is studied. The resulting molecule, TBD, exhibits rapid dipole switching due to the presence of an intra-molecular twist caused by steric hindrance between the tert-butyl and carbonyl groups. The small size and non-interacting nature of TBD is utilized for enhancing the electrical properties of P(VDF-TrFE) by adding TBD as a plasticizer in the semi-crystalline matrix. The intercalation of TBD in between the polymer chains is shown to enhance C-F dipole switching in response to an external AC field. Reduction in the fraction of randomly oriented dipoles of P(VDF-TrFE) due to the presence of TBD is clearly manifested in two major results: a) higher P(E) magnitude which is confirmed with morphology correlations using PFM and b) higher FET mobility due to reduced semiconductor-dielectric interfacial disorder.

3.8 References

1 Kang, M. J. *et al.* Alkylated Dinaphtho [2, 3-b: 2′, 3′-f] Thieno [3, 2-b] Thiophenes (Cn-DNTTs): Organic Semiconductors for High-Performance Thin-Film Transistors. *Advanced Materials* **23**, 1222-1225 (2011).

2 Uno, M., Tominari, Y. & Takeya, J. Fabrication of high-mobility organic single-crystal field-effect transistors with amorphous fluoropolymer gate insulators. *Organic Electronics* **9**, 753-756 (2008).

3 Jones, B. A., Facchetti, A., Wasielewski, M. R. & Marks, T. J. Tuning orbital energetics in arylene diimide semiconductors. Materials design for ambient stability of n-type charge transport. *Journal of the American chemical society* **129**, 15259-15278 (2007).

4 Sekitani, T., Zschieschang, U., Klauk, H. & Someya, T. Flexible organic transistors and circuits with extreme bending stability. *Nature materials* **9**, 1015 (2010).

5 Prevot, P.-H., Alvares, D., Micolich, A., Lovell, N. & Ladouceur, F. An all-organic active pixel photosensor featuring ion-gel transistors. *Journal of Organic Semiconductors* **3**, 8-13 (2015).

6 Gelinck, G., Heremans, P., Nomoto, K. & Anthopoulos, T. D. Organic transistors in optical displays and microelectronic applications. *Advanced materials* **22**, 3778-3798 (2010).

7 Someya, T. *et al.* Integration of organic FETs with organic photodiodes for a large area, flexible, and lightweight sheet image scanners. *Electron Devices, IEEE Transactions on* **52**, 2502-2511 (2005).

8 Sekitani, T. *et al.* Organic nonvolatile memory transistors for flexible sensor arrays. *Science* **326**, 1516-1519 (2009).

9 Li, J., Sun, Z. & Yan, F. Solution Processable Low-Voltage Organic Thin Film Transistors with High-k Relaxor Ferroelectric Polymer as Gate Insulator. *Advanced Materials* **24**, 88-93 (2012).

10 Noh, Y.-Y., Zhao, N., Caironi, M. & Sirringhaus, H. Downscaling of self-aligned, all-printed polymer thin-film transistors. *Nature nanotechnology* **2**, 784 (2007).

11 Veres, J., Ogier, S. D., Leeming, S. W., Cupertino, D. C. & Mohialdin Khaffaf, S. Low-k insulators as the choice of dielectrics in organic field-effect transistors. *Advanced Functional Materials* **13**, 199-204 (2003).

12 Senanayak, S. P., Guha, S. & Narayan, K. Polarization fluctuation dominated electrical transport processes of polymer-based ferroelectric field effect transistors. *Physical Review B* **85**, 115311 (2012).

13 Hulea, I. *et al.* Tunable Fröhlich polarons in organic single-crystal transistors. *Nature materials* **5**, 982 (2006).

14 Lee, K. H. *et al.* "Cut and stick" rubbery ion gels as high capacitance gate dielectrics. *Advanced Materials* **24**, 4457-4462 (2012).

15 Khodagholy, D. *et al.* High transconductance organic electrochemical transistors. *Nature communications* **4**, 2133 (2013).

16 Herlogsson, L., Crispin, X., Tierney, S. & Berggren, M. Polyelectrolyte-Gated Organic Complementary Circuits Operating at Low Power and Voltage. *Advanced Materials* **23**, 4684-4689 (2011).

17 Peng, J., Sun, Q., Wang, S., Wang, H.-Q. & Ma, W. Low-temperature solution-processed alumina as gate dielectric for reducing the operating-voltage of organic field-effect transistors. *Applied Physics Letters* **103**, 061603 (2013).

18 Meyers, S. T. *et al.* Solution-processed aluminum oxide phosphate thin-film dielectrics. *Chemistry of Materials* **19**, 4023-4029 (2007).

19 Wei, C.-Y. *et al.* Pentacene-based thin-film transistors with a solution-process hafnium oxide insulator. *IEEE Electron Device Letters* **30**, 1039-1041 (2009).

20 Avis, C., Kim, Y. G. & Jang, J. Solution processed hafnium oxide as a gate insulator for low-voltage oxide thin-film transistors. *Journal of Materials Chemistry* **22**, 17415-17420 (2012).

21 Klauk, H., Zschieschang, U., Pflaum, J. & Halik, M. Ultralow-power organic complementary circuits. *Nature* **445**, 745-748 (2007).

22 Senanayak, S. P. *et al.* Self-Assembled Nanodielectrics for High-Speed, Low-Voltage Solution-Processed Polymer Logic Circuits. *Advanced Electronic Materials* **1** (2015).

23 DiBenedetto, S. A., Facchetti, A., Ratner, M. A. & Marks, T. J. Molecular self-assembled monolayers and multilayers for organic and unconventional

inorganic thin-film transistor applications. *Advanced materials* **21**, 1407-1433 (2009).

24 Ha, Y.-G., Everaerts, K., Hersam, M. C. & Marks, T. J. Hybrid gate dielectric materials for unconventional electronic circuitry. *Accounts of chemical research* **47**, 1019-1028 (2014).

25 Harada, J., Ohtani, M., Takahashi, Y. & Inabe, T. Molecular motion, dielectric response, and phase transition of charge-transfer crystals: acquired dynamic and dielectric properties of polar molecules in crystals. *Journal of the American Chemical Society* **137**, 4477-4486 (2015).

26 Heitzer, H. M., Marks, T. J. & Ratner, M. A. Molecular Donor–Bridge–Acceptor Strategies for High-Capacitance Organic Dielectric Materials. *Journal of the American Chemical Society* **137**, 7189-7196 (2015).

27 Wright, J. D. *Molecular Crystals*. 2nd Edition edn, (Cambridge University Press, 1995).

28 Debye, P. *Z. Phys.* **13** (1912).

29 P.Debye. *Polar Molecules*. (Dover Press, 1945).

30 Davis, G., Furukawa, T., Lovinger, A. J. & Broadhurst, M. Structural and dielectric investigation on the nature of the transition in a copolymer of vinylidene fluoride and trifluoroethylene (52/48 mol%). *Macromolecules* **15**, 329-333 (1982).

31 Yang, L. *et al.* Novel polymer ferroelectric behavior via crystal isomorphism and the nanoconfinement effect. *Polymer* **54**, 1709-1728 (2013).

32 Capsal, J.-F., Galineau, J., Lallart, M., Cottinet, P.-J. & Guyomar, D. Plasticized relaxor ferroelectric terpolymer: Toward giant electrostriction, high mechanical energy and low electric field actuators. *Sensors and Actuators A: Physical* **207**, 25-31 (2014).

33 Xu, P. & Zhang, X. Investigation of MWS polarization and dc conductivity in polyamide 610 using dielectric relaxation spectroscopy. *European Polymer Journal* **47**, 1031-1038 (2011).

34 Radmacher, M., Tillamnn, R., Fritz, M. & Gaub, H. From molecules to cells: imaging soft samples with the atomic force microscope. *Science* **257**, 1900-1905 (1992).

35 Lovinger, A. J., Davis, G., Furukawa, T. & Broadhurst, M. Crystalline forms in a copolymer of vinylidene fluoride and trifluoroethylene (52/48 mol%). *Macromolecules* **15**, 323-328 (1982).

36 Seki, Y., Kita, R., Shinyashiki, N., Yagihara, S. & Yoneyama, M. in *AIP Conference Proceedings*. 466-469 (AIP).

37 Boyd, R. H. Relaxation processes in crystalline polymers: molecular interpretation—a review. *Polymer* **26**, 1123-1133 (1985).

38 Furukawa, T. *et al.* Ferroelectric phase transition in a copolymer of vinylidene fluoride and trifluoroethylene. *Ferroelectrics* **32**, 61-67 (1981).

39 Steeman, P. & Maurer, F. Dielectric properties of polyamide-4, 6. *Polymer* **33**, 4236-4241 (1992).

Image Pixel Device Using Integrated Organic Electronic Components

Chapter 4

4.1 Introduction

The previous chapter provided an in-depth study of fabricating low voltage, high performance PFETs by engineering key material characteristics for their incorporation into functional circuits. In this chapter, a proof of concept passive pixel sensor, primarily a photodiode connected in series with an FET which is widely used as the optical sensor in cameras, is fabricated and characterized using a low voltage PFET containing the oxide-SAM hybrid dielectric. The ubiquitous camera-element in mobile phone platforms has undergone a vast transformation over the last decade and has become a major factor in the energy management and pricing of these gadgets. The current standards for complementary metal-oxide semiconductor (CMOS) based image sensing offer pixel densities higher than 20 megapixels per inch, low noise levels and ultra-high definition images[1]. However, apart from the complexities in design and fabrication of high-end CMOS chips, a foreseeable constraint is the necessity for planar, rigid substrates. Solution-processed organic semiconductors enable the use of flexible and conformal substrates in addition to facile integration with optics, and vertical integration of device elements[2,3]. These factors, in principle, can result in higher pixel densities and large spatial fill-factors leading to better image resolution.

There has been a significant development in organic electronics for CMOS-like optical sensors over the last two decades. Structures incorporating many components in a pixel such as the OPD:FET passive pixel sensors (PPS)[4], sheet scanners[5], non-volatile resistive sensors[6], OPD based linear sensor arrays[7] and organic light-dependent resistor based sensors[8] have been explored. The feasibility of printing techniques to fabricate arrays of sensors on varied substrates can potentially overcome form[9], cost and performance barriers. Among organic image sensors, the PPS is most promising for integration into arrays due to high signal to noise ratio, high pixel densities and overall robustness as shown previously[10]. In a PPS, the photocurrent, in addition to the dark current, is integrated over the dynamic capacitance of an illuminated photodiode. The PFET in series with the

OPD modulates the signal during the integration and sampling period. The PFET is used to address individual pixels and acts as a nearly ideal switch which isolates the OPD when it is turned off thereby decreasing the overall dark current in the circuit. The figure of merit for the image sensor pixel is determined by the photocurrent vs. intensity response, which decides the operating regime. A typical sensor relies on the sensor's linear response over several decades of light intensity[11]. While the upper limit of operation is marked by photocurrent saturation, the lower limit of the linear region is determined by the signal-to-noise ratio of the pixel. There are very few examples of solution-processed circuit elements consisting of an OPD and PFET for imaging purposes[12,13]. These devices which resemble conventional image sensors can gain tremendous significance upon introducing fabrication methodologies involving spontaneous assembly of both the diode and FET active layers. For instance, a spontaneous vertical phase-separation of components from a bulk heterojunction (BHJ) mixture[14] can result in a donor-enriched bottom layer (forming the PFET channel) and a bulk/top layer forming the OPD active layer. Simultaneous formation of active layers of PFET and OPD components along with suitable electrode patterning can significantly reduce the manufacturing complexity of large area image sensors.

Organic image sensors are limited by the large turn-on voltage and low PFET mobility resulting in unreliable and low performance values[13]. The use of high mobility polymers with appropriate thin dielectrics[15] provide a viable route to this end. Similarly, photosensitivity can be improved by utilizing BHJ based devices which are the most efficient in the class of solution processed photodetectors[16]. It has been widely observed that the properties of BHJ OPDs are sensitive to the composition, buffer layers, thickness of the BHJ layer and processing conditions[17,18]. It should be mentioned that BHJ based OPDs exhibit high open circuit voltage (V_{oc}) which can enable signal read-out in the photovoltaic mode (PV) of operation also leading to a logarithmic intensity response[19]. In this chapter, we emphasize

vices operating in the photoconductive mode (PC) and demonstrate two material dependent properties which affect the linear regime of operation of the PPS.

4.2 Device Fabrication

Patterned ITO coated substrates were cleaned (details in Chapter 3) and coated with aluminum gate electrodes (not on ITO) by PVD using a shadow mask. The Al coated substrates were immediately exposed to pure oxygen plasma for 15 min which was followed by immersing the substrates in THF:EtOH (1:1) solution containing octadecyl phosphonic acid (OPA) at 60°C for 12 hours for SAM formation. The FET active layer PBTOR was spin-coated from a 7 mg/ml chlorobenzene solution on the SAM functionalized substrates. Gold S-D electrodes (50 nm) were subsequently coated by PVD. The gold electrode was serially connected to the ITO during the evaporation process. This was followed by selectively exposing the ITO coated region to mild air plasma for 5 minutes to clean the surface for OPD fabrication. Zinc Oxide (ZnO) was chosen as the electron transport layer for the OPD. ZnO nanoparticles dispersed in an ethanol solution (Sigma-Aldrich) was spin-coated on the ITO at 3000 rpm by masking the FET and annealed at 70°C for 15 min. Subsequently, without removing the mask, the photodiode active layer (PBDTTT-CT:$PC_{71}BM$) was spin-coated from a 40 mg/ml chlorobenzene solution at 1000 rpm for 60 seconds. Using a shadow mask, the counter electrode MoO_x/Ag (8/100 nm) was evaporated thermally to complete pixel fabrication. MoO_x was chosen as the hole buffer layer for better charge extraction as shown in the band energy diagram of the OPD in Figure 4.2(c). The area of the completed device was 0.17 cm^2.

4.3 Device Characterization

4.3.1 Polymer Field Effect Transistor

High performance PFETs were obtained with typical characteristics as shown in Figure 4.1. The PFET measurements were carried out at room temperature under vacuum using a Keithley 2400 semiconductor parameter analyzer. Saturation

characteristics were obtained under -3 V and the average saturation hole mobility of 0.08 cm^2/V.s with a range from 0.15 to 0.01 cm^2/V.s (measured over 20 devices) was obtained using the equation: $\mu = (L/V_{ds}C_i)\left(\frac{g_m}{W}\right)$. The PFETs exhibited an ON-OFF ratio of 10^4 and a threshold voltage of -1 V.

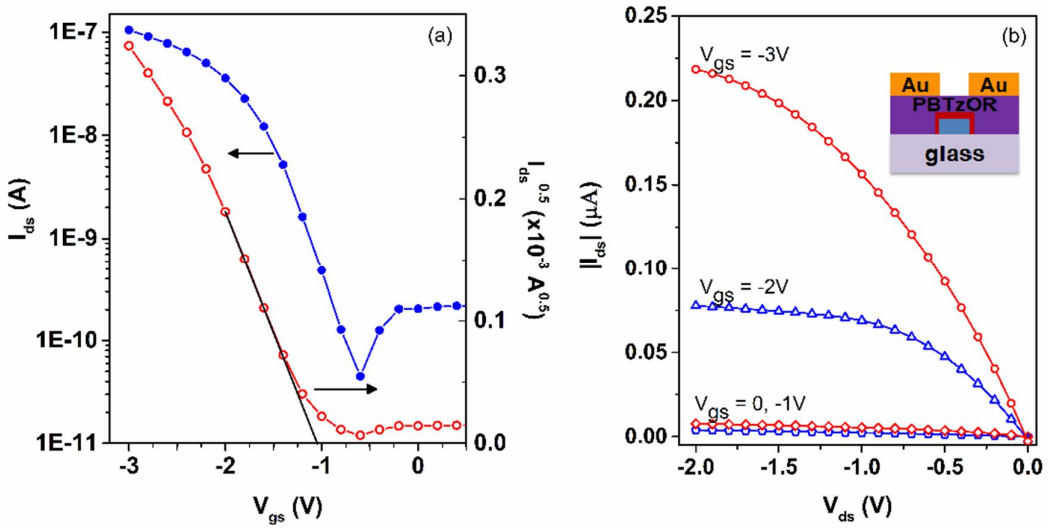

Figure 4.1: (a) Transfer characteristics and (b) output characteristics of a p-type PFET with W/L=17. Inset of (b) shows the PFET device structure.

4.3.2 Organic Photodiode

Steady state current vs. voltage (J(V)) measurements of standalone OPDs was obtained using standard light sources. Figure 4.2(a) shows the J(V) characteristics of discrete OPDs with thicknesses of 200 nm and 500 nm in dark, and under AM 1.5, 1 sun illumination conditions. As the thickness of the BHJ was increased, we obtained a decrease in dark current which is desirable. However, this was accompanied by a decrease in the J(V) characteristics under illumination for the thicker OPD. The reverse saturation current in thicker OPDs was lower in magnitude and also exhibited increased field-dependence or the Poole-Frenkel effect due to space-charge generation in the bulk[20].

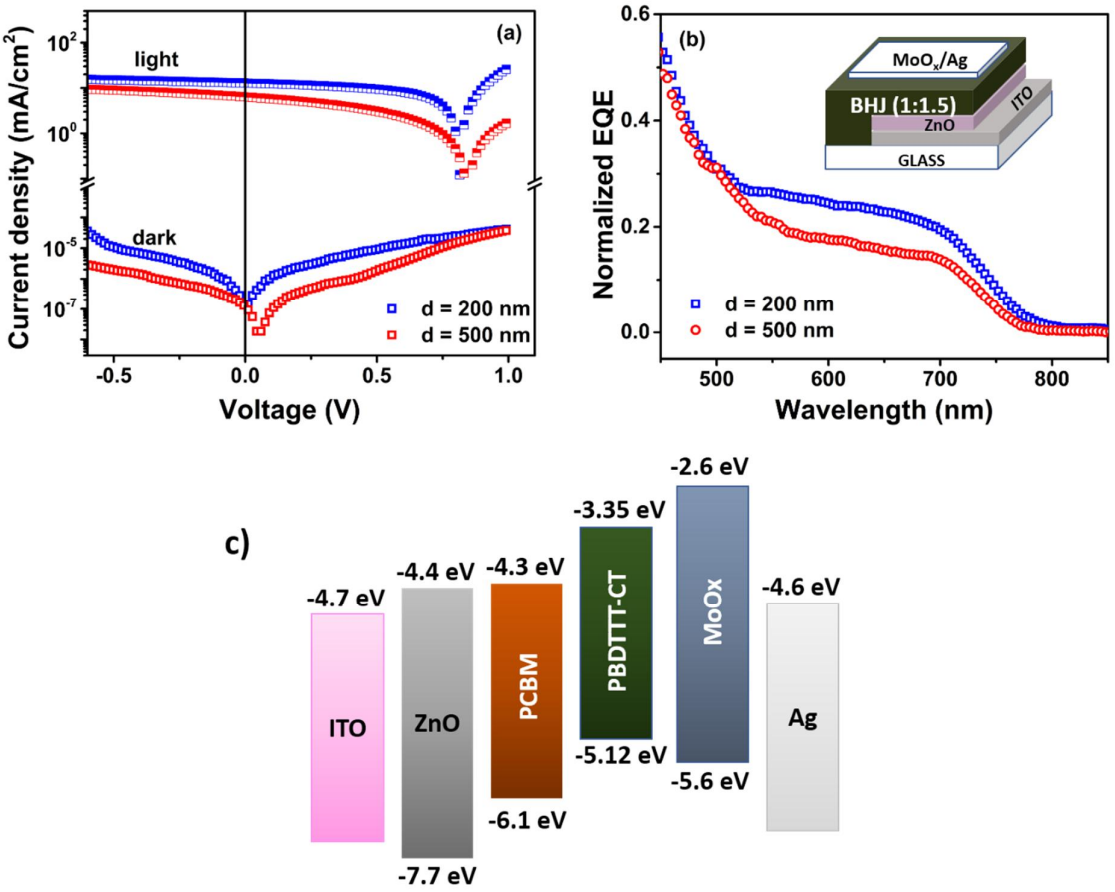

Figure 4.2: (a) J(V) characteristics in dark and under AM 1.5, 1 sun illumination for OPDs of two thicknesses, d=200 nm and d=500 nm, (b) Normalized External Quantum Efficiency (EQE) at 0.4 V reverse bias for OPDs of thicknesses, d=200 nm and d=500 nm. Inset of (b) shows the device structure, c) Energy band diagram of the OPD device architecture.

4.3.3 Integrated Structure

The OPD and PFET were integrated on a single substrate with the anode of the OPD connected serially with the drain of PFET during electrode evaporation. The integrated structure is schematically depicted in Figure 4.3(b). The circuit-equivalent is shown in Figure 4.5(a). Circuit dynamic range measurements were performed with a mercury light source/532 nm laser along with suitable aligned optics. Light pulses were generated using an SRS laser shutter controller and a 1 GHz digital scope (LeCroy WaveRunner) was used to capture the time series data.

Initially, an external reverse bias is applied to the OPD under dark conditions. At this instant (t=0), a light pulse illuminating the pixel is generated for a period t_{int}. The photoresponse of the BHJ layer leads to a charge carrier buildup during the exposure time. Subsequently, during the shutter closure duration, the accumulated charge Q(t_{int}), where Q(t_{int})=(i_{ph}+i_{dc})t_{int} is extracted via the PFET by measuring the current decay $I_{ph}(t)$ across the cathode of the OPD and the source electrode (I_{cs}). The maximum non-saturating photocurrent is given by i_{ph}(max)=(Q_{max}/t_{int})-i_{dc} where, Q_{max} is the charge capacity of the OPD, is obtained at the instant the shutter is closed. A clear photoinduced signal signifying the buildup and decay is observed across the integrated circuit with the two components (Figure 4.3(a)).

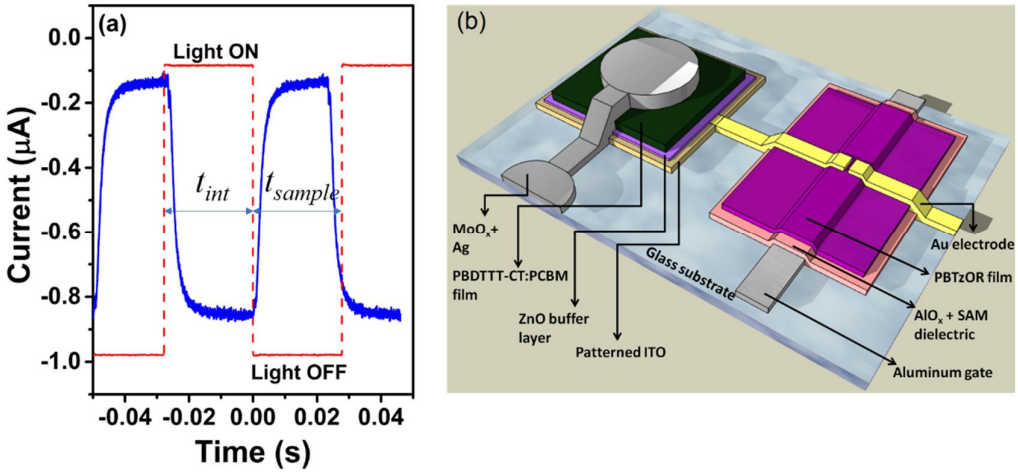

Figure 4.3: (a) Timing diagram for an integrated OPD:PFET pixel showing current measured across the PFET source and OPD cathode (CS current) for a pulsed 1 mW, 532 nm illumination, (b) integrated device structure.

It must be noted here that the PFET functions only as a switch in PPS and hence, the output is a direct outcome of the photo-detected signal from the OPD with similar PFET characteristics reflected in all the pixels. To eliminate the inherent variations in the PFET, two control experiments were performed apart from obtaining results from many devices. Initially, the low power light pulse is directed exclusively on the PFET channel region and the gate transients are

observed. The ON current did not alter significantly during the exposure-scan cycle (Figure 4.4(a)) indicating that stray illumination does not affect the drain-source current during sensor operation.

The absence of PFET contribution is also confirmed from the nature of the decay transient (read-out time) of the integrated structure. The read-out time, measured as the RC time constant of the integrated structure is given by the formula: $\tau = R_{on} * C_{pixel}$. It is obtained by measuring the rate of voltage decay across a 1 MΩ resistance between the source of the PFET and the ground and is represented in the circuit shown as inset of Figure 4.5(b). The dynamic capacitance of the OPD (C_D) in addition to the parasitic gate overlap capacitance of the PFET constitutes the overall capacitance of the circuit (C_{pixel}). The triode resistance of the PFET during accumulation mode operation (switch ON) along with the series resistance of the OPD under illumination constitutes the overall resistance in the circuit (R_{on}). As seen in Figure 4.4(b), a single exponential behavior is obtained for the decay transient which implies that trapping mechanisms in the PFET channel do not play a significant role in charge extraction and transfer[4].

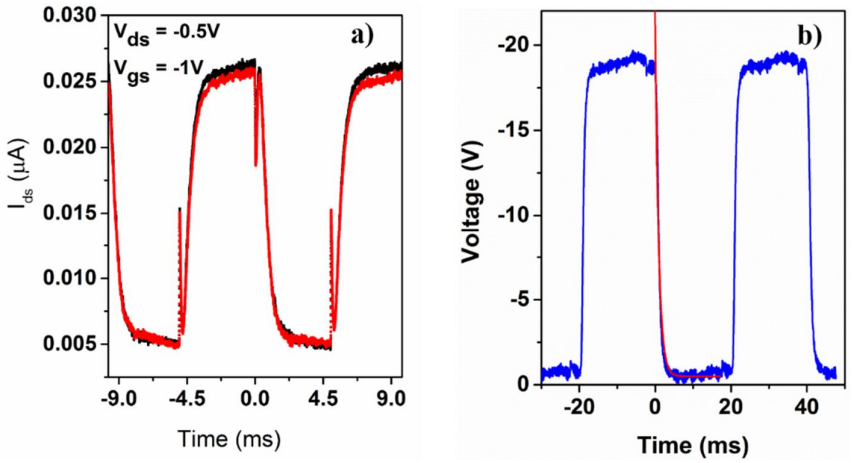

Figure 4.4: (a) CS current upon illuminating the PFET alone, (b) single exponential fit to the output current signal from the PFET.

4.4 OPD Thickness Dependence

Charge transport in amorphous semiconductors is predominantly via hopping due to inherent energetic disorder where the charge carriers undergo multiple and stochastic trap and release events before being collected at the electrodes. In this framework, the photocurrent is dependent on material morphology such as the thickness of the BHJ layer. The photogenerated charge extraction efficiency is represented by the Hecht equation, $\frac{Q(V_{rev})}{Q_0} = \tau_d \mu V_{rev} L^{-2} \left(1 - \exp\left(-\frac{L^2}{\tau_d \mu V_{rev}}\right)\right)$where, Q/Q_0 is the fraction of extracted charge for an externally applied reverse bias V_{rev}, τ_d is the transit time of the charge carriers and μ is the mobility of the charge carriers[21]. As we see from this equation, Q/Q_0 depends on the mobility-lifetime product ($\mu\tau$) of the photoactive layer. If we consider the mobility to be independent of external BHJ parameters such as layer thickness, the charge lifetime which is thickness dependent determines the magnitude of $Q(V_{rev})$. From standard semiconductor theory, it can be derived that the photocurrent is altered by a factor $\frac{\tau_r+\tau_c}{\tau_r}$, where τ_r is the average release time and τ_c is the average capture time of charge carriers[22]. Consequently, the photocurrent alters the signal read-out in the integrated structure as well. Extraction efficiency dependence on thickness of OPD is seen in individual OPDs of two thicknesses 200 nm and 500 nm as J(V) characteristics in Figure 4.2(a) and EQE in Figure 4.2(b). Since the J(V) characteristics of individual OPDs show clear signatures of photocurrent variation in the reverse bias for the two BHJ thicknesses, we examined the effect of thickness on the overall performance of the PPS. The linear dynamic range (LDR) yields the performance parameter of the integrated structure (PPS) and variations in the OPD and PFET are directly translated in the extent of the linear regime in the LDR characteristics.

To obtain the LDR, the PPS was subjected to a constant bit line voltage (V_{GS}) of -0.5 V and word line voltage (V_{CS}) of -2 V to measure the photocurrent transient. Various neutral density filters along with focusing optics were used to

measure the light intensity-dependence. However, it should be noted that all the figure of merit parameters are not translated to the integrated structure due to additional losses emerging from the PFET output current (I_{DS}).

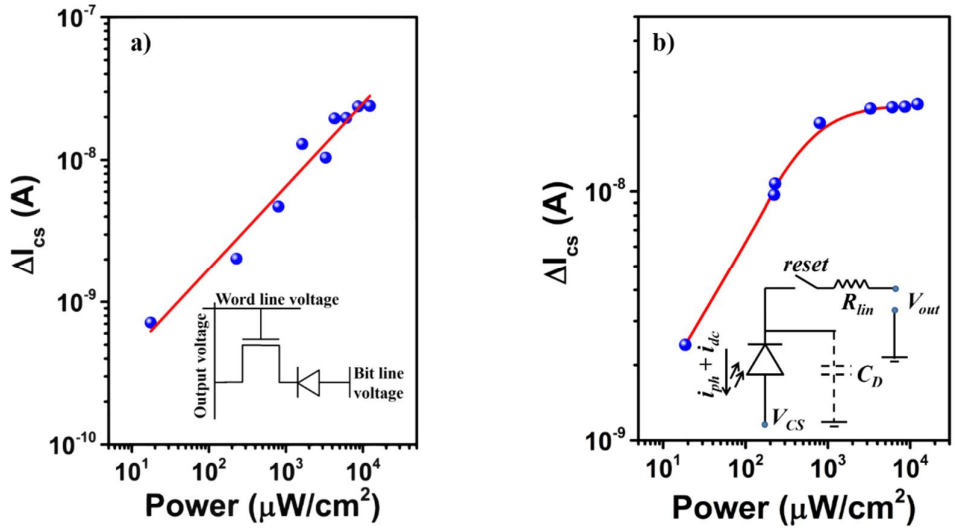

Figure 4.5: LDR of the integrated structure for (a) Pixel1 and (b) Pixel2. Inset of (a) shows the circuit diagram of the integrated pixel and inset of (b) shows the RC equivalent circuit. R_{lin} is the triode resistance of the PFET and C_D is the dynamic capacitance of the OPD.

Figures 4.5(a) and 4.5(b) show the light intensity-dependence of the pixels incorporating BHJs of the two thicknesses discussed above. The low intensity range of operation of Pixel1 (d=200 nm) is ≈17 μW/cm^2, which can be improved by increasing the thickness of the OPD as seen from Pixel2 (d=500 nm) where the resolvable signal is ≈10 μW/cm^2. It is also possible to extend this limit and access the noise equivalent power (NEP) of the OPD by using amplification schemes in the read-out circuit. In the higher intensity regime, Pixel1 exhibits linearity up to the measured intensity of ≈12 mW/cm^2.

The above observations show that the OPD response characteristics determined by the active material and interface parameters clearly affect the overall sensor features also. This outcome is studied further in detail. The analysis of the storage mode of the OPD in series with a PFET is derived from the current balance

equation: $C_v \frac{dV}{dt} = -(I_{dark} + I_{photo})$, where, C_v is the photovoltage dependent capacitance (dynamic capacitance). Upon substituting for the dark current and photo-generated current based on the diode equations, the time dependent voltage is obtained as $V(t) = [V_0^{2/3} - \frac{2}{3} I_0 H (\frac{12}{qa\varepsilon^2})^2 t]^{3/2}$ where, V_0 is the initial reverse bias voltage applied to the OPD, I_0 is the photosensitivity of the OPD, H is the illumination intensity and a is the carrier concentration in dark[23]. The equation states that the rate at which the photovoltage decays depends on the illumination intensity and photosensitivity of the OPD. Therefore, if the photosensitivity of the OPD is low, the read-out times are larger as the photovoltage takes longer time to decay.

The photosensitivity is directly related to the quantum efficiency of the OPD by the relation: $I_{ph} = e\eta\lambda P_0 / hc$ where, η is the external quantum efficiency (EQE) of the OPD and P_0 is the incident light power. From the above equation we obtain a comparison between the two OPDs based on their EQE value. The EQE graph at 0.4 V reverse bias of the OPD for the two thicknesses of the BHJ is shown in Figure 4.2(b). Despite the higher absorption for thicker BHJ layers, the EQE value is lower due to losses arising from charge carrier trapping and/or charge carrier recombination thereby resulting in an overall increase in series resistance. As seen by previous studies, the magnitude of extracted current shows a gradual decrease with increasing thickness[23], especially in organic materials, which are prone to low mobility-lifetime ($\mu\tau$) products. Consequently, we see an overall decrease in EQE which explains the narrowing of the linear mode operation of the sensor. The effect of the OPD thickness is observed in the read-out time of the PPS also. The read-out times for Pixel1 and Pixel2 as obtained from the fit of the I_{CS} decay transient are 0.7 ms and 0.9 ms respectively. The difference in the read-out time is related to the reduced dynamic capacitance for the thicker OPD. However, the decay time constant is large due to overall low specific capacitance (C_s) of the pixel, a common shortcoming of PPS. C_s can be reduced by placing a storage capacitor parallel to the

OPD or by employing the active pixel structure which isolates the line capacitance from the circuit[24].

4.5 A Self-Assembled PPS

OPDs, in particular, bulk heterojunction (BHJ) blends of donor and acceptor polymers are most efficient as the photo-responsive element in the PPS. They exhibit absorption coefficients of the order of $10^5/cm$[25] and signal response times in nanoseconds[26]. Large linear responses encompassing 8 orders of magnitude for BHJ based photodiodes before the sub-linear bimolecular recombination mechanisms take over at AM 1.5 levels can be utilized, in principle, to extend the LDR in these pixels[16]. Similarly, one of the many possible ways to decrease the response time of the OPD is studied by fabricating stratified hetero-structures of alternating donor and acceptor layers where the thickness of each layer is of the order of the diffusion length of the charge carriers. This architecture leads to more efficient charge separation and faster charge extraction which enabled a response time of 720 ps[27]. A previous study from our lab noted that by utilizing a thin layer of the acceptor above the electron buffer layer in a solar cell, charge extraction was improved which increased the short circuit current density and subsequently, the efficiency of the solar cell[28]. Similarly, a previous report showed that the solar cell efficiency can also be increased in a ternary blend of P3HT:$PC_{71}BM$ and DPP-DTT due to higher hole mobility of DPP-DTT which enables balanced charge carrier extraction[29]. Most commonly, two or more polymer donors in a mixture with a $PC_{71}BM$ acceptor have the inherent property to partially phase segregate when cast into a film due to surface energy variations and varying degree of solubility in a common solvent[14]. By combining the above two properties, we have tuned the pixel architecture to obtain a monolithic solution processed PPS. Casting the BHJ blend on a thin layer of high molecular weight DPP-DTT creates an energetically favorable landscape for the donor polymer (P3HT) to mix with the underlying DPP-DTT layer. As a result, a ternary blend and a graded junction combining the PFET channel and the photo-

responsive layer respectively, is generated. The schematic of the PPS is shown in Figure 4.6(a).

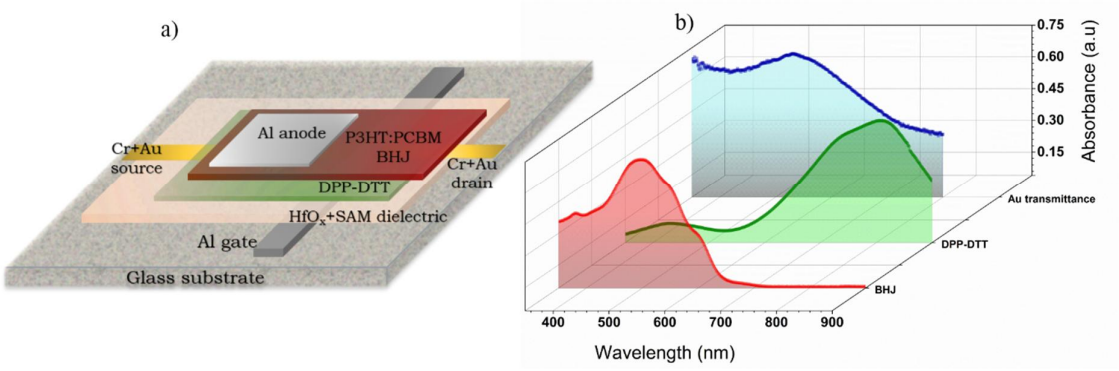

Figure 4.6: a) Monolithic image sensor pixel architecture, and b) Absorbance of the P3HT:PC_{71}BM BHJ blend film, pristine DPP-DTT film and the transmittance of a 20 nm semi-transparent Cr+Au electrode with the DPP-DTT film coated over it.

DPP-DTT in the blend improves charge extraction and the pristine underlying layer functions as the channel for charges in the PFET of the sensor. DPP-DTT is an ideal candidate to realize a blended OPD cum PFET due to its complementary absorption spectrum as compared to the BHJ components. This ensures that DPP-DTT participates only in charge transport which minimizes variations in PFET operation when incorporated into an array. As shown in Figure 4.6(b), DPP-DTT absorbs in the near-infrared region and does not have a significant peak at the photopic maximum of the spectrum. The P3HT:PC_{71}BM BHJ layer has an absorption maximum at 555 nm which is ideal for the photoactive layer of the sensor. The Cr+Au electrode which acts as the anode cum PFET drain electrode exhibits nearly 75% transmittance in the visible region with a drop from 700 nm due to the presence of the DPP-DTT layer.

4.5.1 Device Fabrication

Bottom-contact PFETs were fabricated using the HfO_x/SAM hybrid dielectric and p-type polymer DPP-DTT as described in detail in Chapter 3. Semi-transparent Cr+Au S-D electrodes (thickness=20 nm) was coated by PVD to allow the incident

light to penetrate the PFET and get absorbed in the OPD active layer. The P3HT:$PC_{71}BM$ blend was spin-coated over the DPP-DTT layer from a 35 mg/ml chlorobenzene solution. MoO_x+Ag was coated as the cathode of the OPD by patterned deposition only above the source of the PFET (Figure 4.6(a)).

4.5.2 PPS Characterization

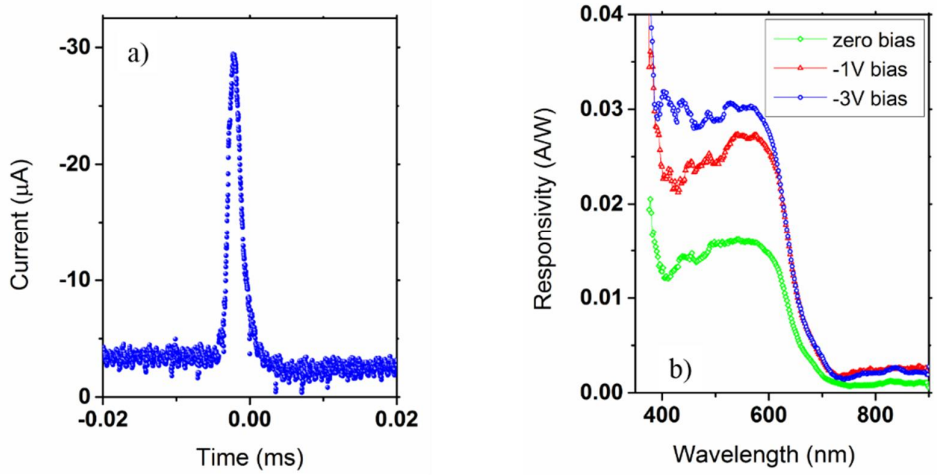

Figure 4.7: a) Photocurrent response transient of the OPD when it is illuminated with a 10 ns, 532 nm laser pulse showing a single exponential decay with a time constant of 1 μs, and b) Responsivity of the OPD as a function of reverse bias.

Excellent output and transfer characteristics are obtained from the PFET (Chapter 3) with an average hole mobility of 0.8±0.1 cm^2/V.s and a maximum ON-OFF ratio of 10^6. The decay transient obtained from the OPD fabricated above the FET is of the order of 1 μs (fall time) with 0.03 A/W responsivity in the photoconductive mode as shown in Figure 4.7(a) and (b) respectively. The fall time forms a crucial parameter in image sensor performance as it determines the rate at which charges can be transferred after one light exposure. These values correspond to a bandwidth $1/2\pi\tau$ of 160 kHz which is excellent even for high speed video recording.

Light response measurements were performed on the integrated structure with a 532 nm CW laser along with suitable aligned optics. As explained in the

previous section, a similar pulsed technique was used to observe the PFET output during multiple exposure-scan cycles of the incident illumination. A clear photoinduced signal signifying the buildup and decay of charges is observed across the integrated circuit with the two components as shown in Figure 4.8.

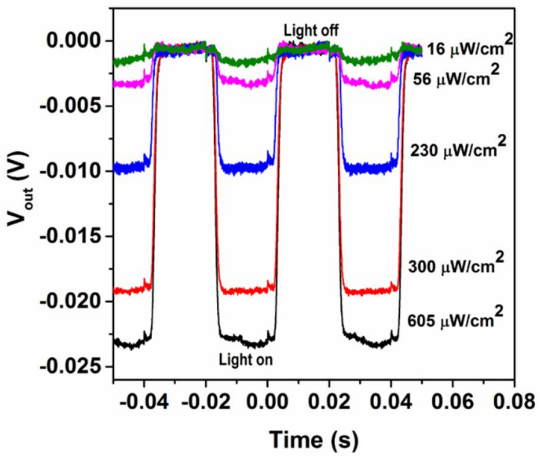

Figure 4.8: Photocurrent transients of the image sensor pixel at different intensities (white LED source).

4.6 Device Simulations

4.6.1 Operation of the Sensor

The working of the proposed PPS architecture was simulated using the Silvaco Atlas 2D TCAD package. Figure 4.9 shows the device structure of the simulated image sensor pixel. An aluminum gate of length 60 μm was chosen to match with experimental dimensions. HfO_x was used as the dielectric with dielectric constant ≈ 22. All the parameters chosen for the simulation are displayed in Table 4.1 below. DPP-DTT was used as the active layer in a bottom contact FET structure with gold S-D electrodes placed with no gate overlap to minimize stray capacitance. A 1 μm thick P3HT:$PC_{71}BM$ layer was defined throughout the FET as the photoactive layer of the OPD, with the cathode of the OPD constructed in alignment with the drain electrode (also the anode of the OPD) of the FET. The simulation code is shown in Appendix A.

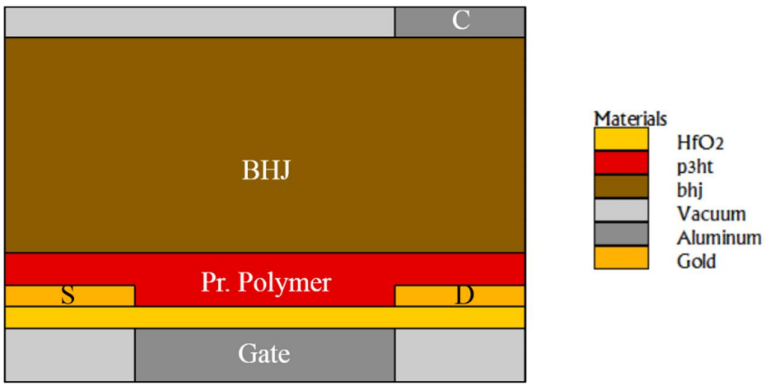

Figure 4.9: Structure of the image sensor pixel as simulated in Atlas.

Charge transport in the FET is characterized by the Poole-Frenkel mobility model whose implications for transport in organic materials has been proved in many studies[30-32]. The presence of sub-gap states due to the disordered nature of the material has led to many important observations especially for the photo-response of the device[33]. Since the simulation deals with the optoelectronic characterization of the PFET and OPD, we take into account the consequence of defect levels by considering an exponential density of states (DOS)[34,35] whose nature is shown in Figure 4.11(b). The defect levels are characterized by a specific trap temperature and density[36]. Similarly, the OPD is characterized using the scheme presented by Koster *et. al.*[37]. The BHJ is considered as a single layer with the difference in the LUMO energy of the acceptor and the HOMO energy of the donor material considered as the bandgap of the composite material. Recombination mechanisms are taken into account using the Langevin theory[38]. Light incidence is simulated by the transfer matrix approach (TMM)[39] which is a 1D method utilizing the interference effects of all the layers where the electromagnetic field amplitudes of the reflected and transmitted wave are directly related to the incident wave amplitude. TMM gives the exact nature of the photon absorption and exciton generation rate can be determined as a function of the BHJ thickness[40].

Table 4.1: Parameters used for Atlas 2D TCAD simulations.

Name of the parameter	Value
N_c, N_v of the DPP-DTT layer	$2.5x10^{19}$ cm^{-3}
N_c, N_v of the BHJ layer	$2.5x10^{19}cm^{-3}$
Bandgap, affinity of the DPP-DTT layer	1.7 eV, 3.5 eV
Bandgap, affinity of the BHJ layer	1.1 eV, 4.0 eV
Zero field hole and electron mobility	$4x10^{-4}$ $cm^2/V.s$
Field dependent mobility parameter (hole and electron)	0.1 $cm^{0.5}$ $V^{-0.5}$
Exciton binding energy	0.28 eV
Characteristic trap temperature	600 K
Total trap density	10^{18} cm^{-3}
Permittivity of the organic layers	3

The image sensor pixel is characterized for its photo-response by including the individual models of charge transport for the PFET and the OPD. Initially, the OPD is reverse biased in dark to a small negative value. Under this condition, the light is switched on for an integration time t_{int}. A photocurrent transient is observed due to separation of charge carriers in the BHJ layer as shown in Figure 4.10(a). The photogenerated charges drift under the influence of the externally applied field with clear increase in the hole concentration close to the PFET channel (Figure 4.10(c)) and increase in electron concentration near the cathode (Figure 4.10(d)). The accumulated charges are extracted after the light is turned off when a gate voltage is applied to drive the PFET into operation (Figure 4.10(b)). The integrated current in the channel of the PFET gives a signature of the intensity of light that was incident on the OPD during one exposure cycle. The decay transient fitted to a single exponential with time constant is equal to 1μs which is in perfect agreement to our experimentally observed OPD transfer rate. However, many other influences such as stray capacitance and line noise can yield a lower limit of the transfer rate in actual devices when the OPD is connected serially to the PFET.

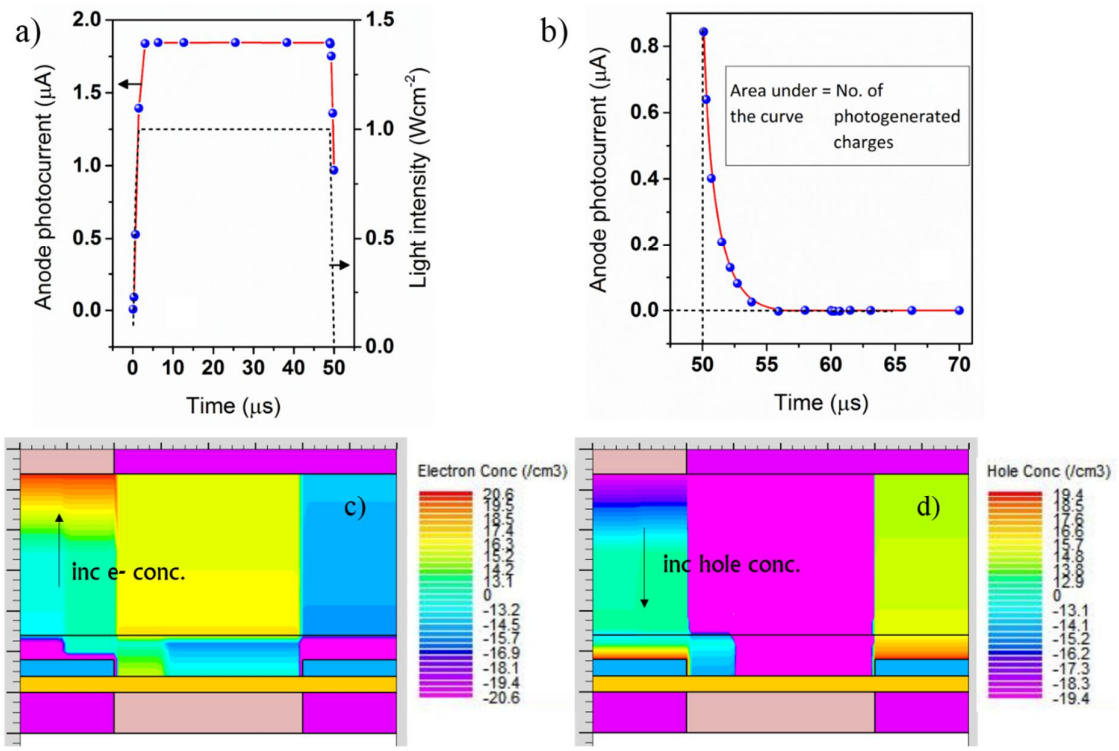

Figure 4.10: a) Photocurrent transient simulated in Atlas, b) Extraction of charges after light exposure, c) and d) electron and hole separation in the BHJ layer during light exposure.

4.6.2 Dark Current Measurements

Various sources of noise distort the signal at especially low light levels which decreases the signal to noise ratio and therefore the LDR of the image sensor. Given a single pixel, the major source of noise is the temporal noise which results due to time dependent signal fluctuations in the PFET channel. This sets a fundamental limit for read-out time as a function of light intensity. The temporal charge fluctuations can be measured in the dark by recording the increase in the number of charge carriers in the FET channel as a function of time. Figure 4.11(a) shows the hole carrier concentration in the FET channel as a function of time when the OPD is reverse biased to 1V in dark. At ambient temperature, the number of charge carriers in the channel is low up to 4 ms after which time it increases rapidly. This rise puts an upper limit for extraction time beyond which the noise dominates. A temperature dependence of the charge accumulation is also presented in Figure

4.11(a). It is observed that when the image sensor is cooled to temperatures reaching 150 K, the time taken for the fluctuations to dominate the signal current is longer and of the order of 0.1 s. On the other hand, the maximum charge transfer time is reduced when the image sensor is operated at 400 K. Due to the inherent disorder in organic materials, charge transport is predominantly of a hopping nature where the charges have to overcome an energetic barrier in order to constitute current[41]. At high temperatures, the thermal barrier for charges is overcome by kT which leads to large carrier fluctuations in the FET channel at small sample times. Cooling the sensor implies high activation for the charge carriers to move thereby decreasing charge fluctuations and increasing the sensitivity of the device.

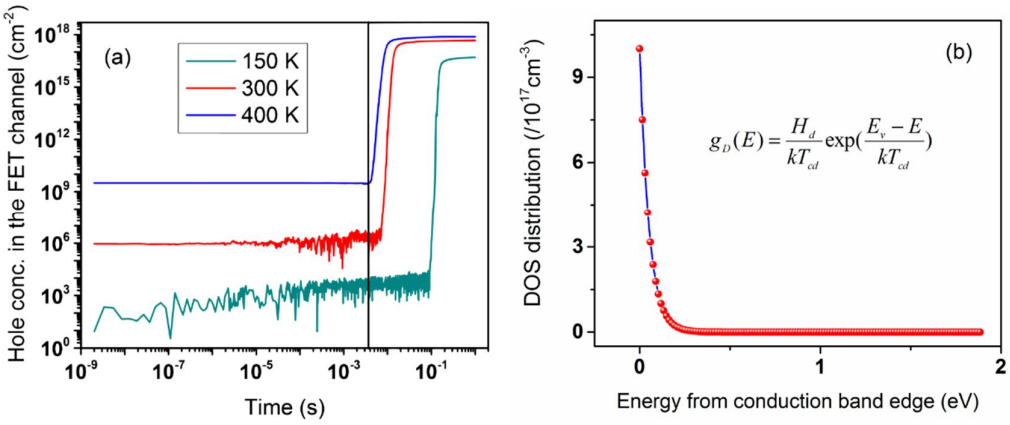

Figure 4.11: a) Charge accumulation in the PFET channel during read-out as a function of temperature, and b) the nature of trap distribution at the semiconductor-dielectric interface.

4.7 Summary

The present studies of a solution processed image sensor pixel demonstrate the suitability of using organic semiconductors to realize applications on non-rigid substrates. The pixel design and fabrication process are relatively simple and exhibits reasonable characteristics. Our observations and results can serve as a good example where the interdependency of the materials, device design, and circuit parameters for image sensor pixel is established, and forms the initial crucial step for fabricating a large area image sensing array with solution processed active layers.

Secondly, graded junctions with a gradual energy change can be formed by facile solubility governed chemistry to improve the efficiency of charge extraction in the photoactive layer of the OPD. An in-depth understanding of the processes during one exposure-read cycle of the novel image sensor pixel architecture is presented using 2D TCAD device simulations. Dark current charge accumulation calculations show that charge transport processes affect the temporal noise of the sensor significantly. The feasibility of synthesizing wavelength specific polymers and their easy processing makes the organic image sensor suitable for low density, high fill-factor imaging applications. However, arrays incorporating these pixels will give a better insight into the various properties of the sensor such as pixel pitch, pixel densities and noise sources for incorporating them into next generation sensor applications.

4.8 References

1 Yasue, T. *et al.* A 1.7-in, 33-Mpixel, 120-frames/s CMOS Image Sensor With Depletion-Mode MOS Capacitor-Based 14-b Two-Stage Cyclic A/D Converters. *IEEE Transactions on Electron Devices* **63**, 153 (2016).

2 Aihara, S. *et al.* Stacked image sensor with green-and red-sensitive organic photoconductive films applying zinc oxide thin-film transistors to a signal readout circuit. *IEEE Transactions on Electron Devices* **56**, 2570 (2009).

3 Jeong, S. W. *et al.* The vertically stacked organic sensor-transistor on a flexible substrate. *Applied Physics Letters* **97**, 253309 (2010).

4 Tong, X. & Forrest, S. R. An integrated organic passive pixel sensor. *Organic Electronics* **12**, 1822 (2011).

5 Someya, T. *et al.* Integration of organic FETs with organic photodiodes for a large area, flexible, and lightweight sheet image scanners. *IEEE Transactions on Electron Devices* **52**, 2502 (2005).

6 Nau, S., Wolf, C., Sax, S. & List-Kratochvil, E. J. W. Organic Non-Volatile Resistive Photo-Switches for Flexible Image Detector Arrays. *Advanced Materials* **27**, 1048 (2015).

7 Yu, G., Wang, J., McElvain, J. & Heeger, A. J. Large-area, full-color image sensors made with semiconducting polymers. *Advanced Materials* **10**, 1431 (1998).

8 Wang, H. *et al.* Three-Component Integrated Ultrathin Organic Photosensors for Plastic Optoelectronics. *Advanced Materials* **28**, 624 (2015).

9 Yoo, G. *et al.* Hemispherical thin-film transistor passive pixel sensors. *Sensors and Actuators A: Physical* **158**, 280 (2010).

10 Baierl, D. *et al.* A hybrid CMOS-imager with a solution-processable polymer as photoactive layer. *Nature communications* **3**, 1175 (2012).

11 Weckler, G. P. Operation of pn junction photodetectors in a photon flux integrating mode. *IEEE Journal of Solid-State Circuits* **2**, 65 (1967).

12 Prevot, P.-H., Alvares, D., Micolich, A., Lovell, N. & Ladouceur, F. An all-organic active pixel photosensor featuring ion-gel transistors. *Journal of Organic Semiconductors* **3**, 8-13 (2015).

13 Takahashi, T. *et al.* Carbon nanotube active-matrix backplanes for mechanically flexible visible light and X-ray imagers. *Nano letters* **13**, 5425 (2013).

14 Loiudice, A. *et al.* Graded vertical phase separation of donor/acceptor species for polymer solar cells. *Solar Energy Materials and Solar Cells* **100**, 147 (2012).

15 Senanayak, S. P. *et al.* Self-Assembled Nanodielectrics for High-Speed, Low-Voltage Solution-Processed Polymer Logic Circuits. *Advanced Electronic Materials* **1**, 1500226 (2015).

16 Stolterfoht, M. *et al.* Photocarrier drift distance in organic solar cells and photodetectors. *Scientific Reports* **5**, 9949 (2015).

17 Kirchartz, T., Agostinelli, T., Campoy-Quiles, M., Gong, W. & Nelson, J. Understanding the thickness-dependent performance of organic bulk heterojunction solar cells: the influence of mobility, lifetime, and space charge. *The Journal of Physical Chemistry Letters* **3**, 3470 (2012).

18 Li, G., Shrotriya, V., Yao, Y. & Yang, Y. Investigation of annealing effects and film thickness dependence of polymer solar cells based on poly (3-hexylthiophene). *Journal of Applied Physics* **98**, 043704 (2005).

19 Chamberlain, S. G. & Lee, J. P. A novel wide dynamic range silicon photodetector and linear imaging array. *Solid-State Circuits, IEEE Journal of* **19**, 41-48 (1984).

20 Natali, D. & Sampietro, M. Field-dependent mobility from space-charge-limited current–voltage curves. *Journal of applied physics* **92**, 5310-5318 (2002).

21 Hecht, K. Zum Mechanismus des lichtelektrischen Primärstromes in isolierenden Kristallen. *Zeitschrift für Physik* **77**, 235 (1932).

22 Shakoor, Z. *Monte Carlo Simulation of Charge Transport in Amorphous Selenium Photoconductors* Master of Science thesis, University of Saskatchewan, (2006).

23 Sievers, D. W., Shrotriya, V. & Yang, Y. Modeling optical effects and thickness dependent current in polymer bulk-heterojunction solar cells. *Journal of Applied Physics* **100**, 114509 (2006).

24 Tedde, S., Zaus, E. S., Fürst, J., Henseler, D. & Lugli, P. Active pixel concept combined with organic photodiode for imaging devices. *IEEE Electron Device Letters* **28**, 893 (2007).

25 Erb, T. *et al.* Correlation between structural and optical properties of composite polymer/fullerene films for organic solar cells. *Advanced Functional Materials* **15**, 1193-1196 (2005).

26 Ohmori, Y., Hamasaki, T., Kajii, H. & Morimune, T. in *SPIE Europe Optics+ Optoelectronics.* 73560W-73560W-73568 (International Society for Optics and Photonics).

27 Peumans, P., Bulović, V. & Forrest, S. R. Efficient, high-bandwidth organic multilayer photodetectors. *Applied Physics Letters* **76**, 3855-3857 (2000).

28 Shivanna, R., Rajaram, S. & Narayan, K. Interface engineering for efficient fullerene-free organic solar cells. *Applied Physics Letters* **106**, 123301 (2015).

29 Liu, S. *et al.* Enhanced efficiency of polymer solar cells by adding a high-mobility conjugated polymer. *Energy & Environmental Science* **8**, 1463-1470 (2015).

30 Bässler, H. Charge transport in disordered organic photoconductors a Monte Carlo simulation study. *physica status solidi (b)* **175**, 15-56 (1993).

31 Blom, P., De Jong, M. & Van Munster, M. Electric-field and temperature dependence of the hole mobility in poly (p-phenylene vinylene). *Physical Review B* **55**, R656 (1997).

32 Novikov, S., Dunlap, D., Kenkre, V., Parris, P. & Vannikov, A. Essential role of correlations in governing charge transport in disordered organic materials. *Physical Review Letters* **81**, 4472 (1998).

33 Narayan, K. & Kumar, N. Light responsive polymer field-effect transistor. *Applied Physics Letters* **79**, 1891-1893 (2001).

34 Salleo, A. *et al.* Intrinsic hole mobility and trapping in a regioregular poly (thiophene). *Physical Review B* **70**, 115311 (2004).

35 Mehraeen, S., Coropceanu, V. & Brédas, J.-L. Role of band states and trap states in the electrical properties of organic semiconductors: Hopping versus mobility edge model. *Physical Review B* **87**, 195209 (2013).

36 Kim, C. H. *Physics-based compact modeling of organic electronic devices*, Ecole Polytechnique X, (2013).

37 Koster, L., Smits, E., Mihailetchi, V. & Blom, P. Device model for the operation of polymer/fullerene bulk heterojunction solar cells. *Physical Review B* **72**, 085205 (2005).

38 Langevin, P. Recombinaison et mobilites des ions dans les gaz. *Ann. Chim. Phys* **28**, 122 (1903).

39 Pettersson, L. A., Roman, L. S. & Inganäs, O. Modeling photocurrent action spectra of photovoltaic devices based on organic thin films. *Journal of Applied Physics* **86**, 487-496 (1999).

40 Harrison, M., Grüner, J. & Spencer, G. Analysis of the photocurrent action spectra of MEH-PPV polymer photodiodes. *Physical Review B* **55**, 7831 (1997).

41 Sirringhaus, H. Device physics of solution-processed organic field-effect transistors. *Advanced Materials* **17**, 2411-2425 (2005).

Porous Alumina Based Organic Nano-Triode Arrays

Chapter 5

5.1 Introduction

Advancement in the field of organic electronic devices has led to their incorporation in mainstream integrated circuits mainly for flexible electronic applications[1,2]. In the quest for miniaturizing electronic devices for denser circuitry, the vertical transistor geometry offers seamless packing density with output characteristics in par with traditional organic field effect transistor (OFET) counterparts. Large strides have been made to enhance the OFET performance characteristics by increasing carrier mobility and improving transport pathways via rational designing of molecules and interfaces[3,4]. Progress in dielectric materials and surface treatments have also led to lowering the threshold voltage of operation[5,6]. However, as growing applications demand higher density of FETs, conventional solution deposition and printing methods may fall short of the requirement criteria. The combination of prerequisites for high performing OFETs involve high on-off ratio, low operating voltage and high switching speed without resorting to complex fabrication processes which pose challenges to the growth and usage of solution processible electronics[7]. In this regard, the vertical organic transistor (VOT) provides a paradigm shift to keep up with the technological requirements in this field. VOTs can overcome short channel limitations[8,9] as well as enable 3D integration of devices thereby reducing the areal footprint of processing electronics in integrated circuits. In VOTs, the semiconductor thickness which is equivalent to the channel length can be accurately controlled to the nanometer scale in a facile manner. As a result, VOT operation can yield large current densities at low voltages along with precise gate voltage control. Several other advantages and large-scale requirements which can be fulfilled by VOTs has resulted in the study of novel architectures to fabricate 3D three terminal devices to obtain transistor-like characteristics[10-19]. To achieve vertical current conduction, nearly all the classes of VOTs employ a perforated source electrode with nanometer-sized pore dimensions. To obtain porosity in the source electrode, the device fabrication involves a direct or indirect lithography step[20] which

ultimately makes the process non-scalable. The organic permeable base transistor (OPBT) is limited by low current amplification β which results in large base recombination currents due to the absence of a perfect blocking contact[21,22]. The vertical field effect transistor (VFETs) geometry reduced off currents by isolating the gate from a perforated source via the dielectric layer[23]. However, most of the gate induced field is shielded by the source metal on the dielectric which increases the operation voltage of the VFETs. The above examples imply that issues in the utilization of VOTs remain. A few of them are: random source electrode porosity which results in unsteady ON currents, complex source patterning and high OFF currents which are due to gate electrode independent pathways between the source and the drain.

The availability of well-defined, large-area mesoporous alumina templates[24] provides an inherently scalable architecture to implement vertical conduction in the form of an organic nano-triode array (ONTA). Through-hole circular pores which are obtained by standard anodization and etching techniques[25,26] provide an ideal template to form an array of nano-devices with densities as high as 10^9 pores/cm^2 (Figure 5.2(a)). Alumina also takes up the role of a dielectric which isolates neighboring conducting channels without resorting to complex lithography processes. This technique avoids the complexity associated with polystyrene-based lithography[27] which has been the most reliable method for obtaining the surround barrier layer in vertical transistors. This chapter describes the fabrication and working principle of the ONTA using commercially available anodized aluminum oxide (AAO) membranes as the template for a porous base (gate-equivalent) electrode. The output characteristics of the fabricated device are analyzed and the underlying working principle is explained as a function of design parameters using 2D finite element simulations to identify key factors affecting device performance. Subsequently, we demonstrate single pore conductivity and basic switching characteristics in the ONTA device for applications in logic and driving circuits.

5.2 Device Fabrication

A patterned indium tin oxide (ITO) on a glass substrate was used as the collector (drain-equivalent) electrode. The ITO coated substrate was cleaned using standard glass cleaning protocol as mentioned in Chapter 3. After RCA cleaning, the substrates were exposed to mild air plasma for 60 seconds to remove organic contaminants. A clean, hydrophilic surface improves AAO adhesion to the ITO. Through-hole AAO membranes were purchased from TopMembranes technology ltd. and utilized without further modification. The base support of PMMA in the AAO membranes was separated from the AAO sheet by gripping the membrane with the ITO substrate using tweezers and dipping the substrate in an acetone bath. The transferred AAO membrane was annealed at 50°C for 5-6 hours to remove any residual acetone. The schematic of the AAO transfer process is shown in Figure 5.1 below.

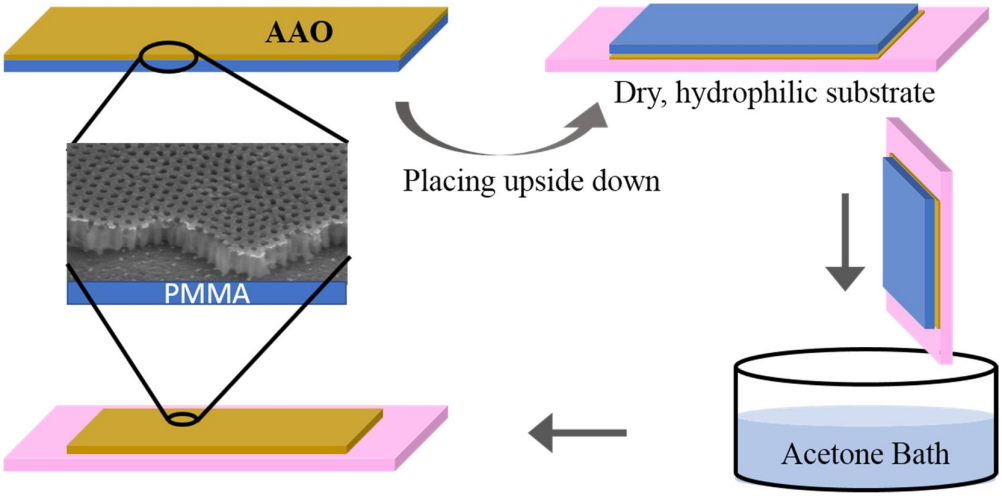

Figure 5.1: Schematic of the procedure of AAO membrane transfer onto a patterned ITO substrate.

The transferred AAO membranes exhibit large-scale pore uniformity as shown in Figures 5.2(b), (c) and (d) and are known to be robust over a wide temperature and solvent range[26-28]. A thin layer of aluminum (~20 nm) was thermally evaporated at 10^{-6} mbar pressure as the base electrode over the AAO. It conforms to the AAO porous structure, thereby resulting in a porous electrode naturally. The sample holder

was placed exactly above the sublimation source in the PVD to ensure that the aluminum does not coat the inner pore walls of the membrane. Along with this condition, the ratio of the pore height to the thickness of the coated aluminum also determined the extent of the coating on the inner walls of the barrier. This is illustrated in Figure 5.3(a) and (b) from which an optimized thickness of 20 nm was chosen for a barrier height of 100 nm to obtain an Al coating without conductivity with the bottom electrode. A control I(V) graph given in Figure 5.3(c) for the optimized conditions shows negligible current between the ITO and Al electrodes in the absence of P3HT filled in the pores. To reduce the base recombination current and the reverse collector-emitter current, the substrates were exposed to an oxygen plasma for 30 minutes to increase the thickness of the nascent oxide layer on the aluminum.

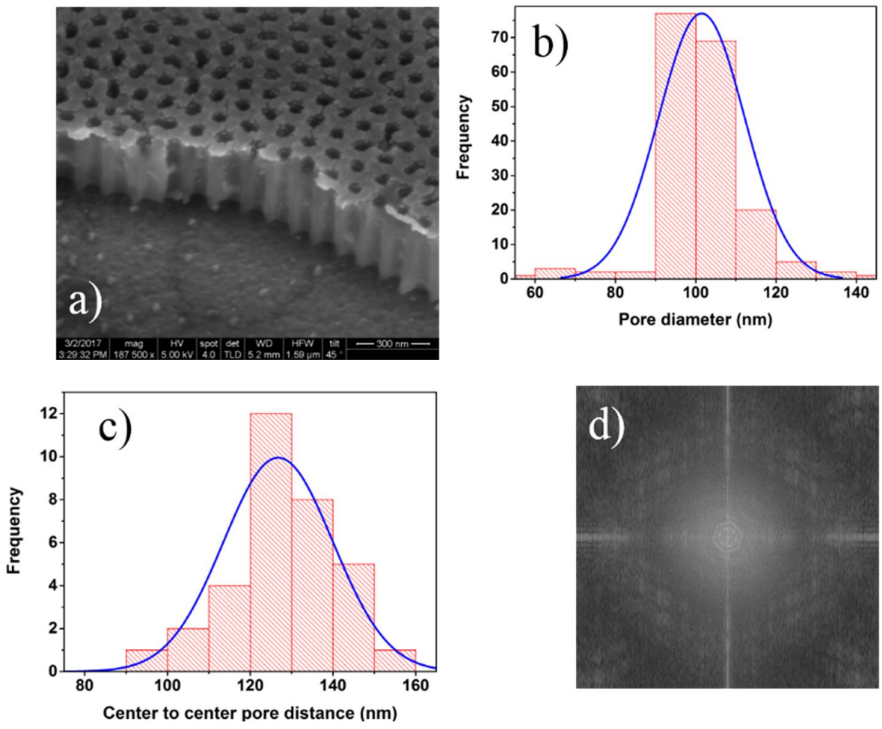

Figure 5.2: a) SEM image of a 300 nm thick the AAO porous membrane coated with 20 nm aluminum and filled with P3HT, b) pore diameter, and c) center to center pore distance statistics showing an average of 100 nm and 125 nm respectively, and d) FFT of the pore structure showing hexagonal packing.

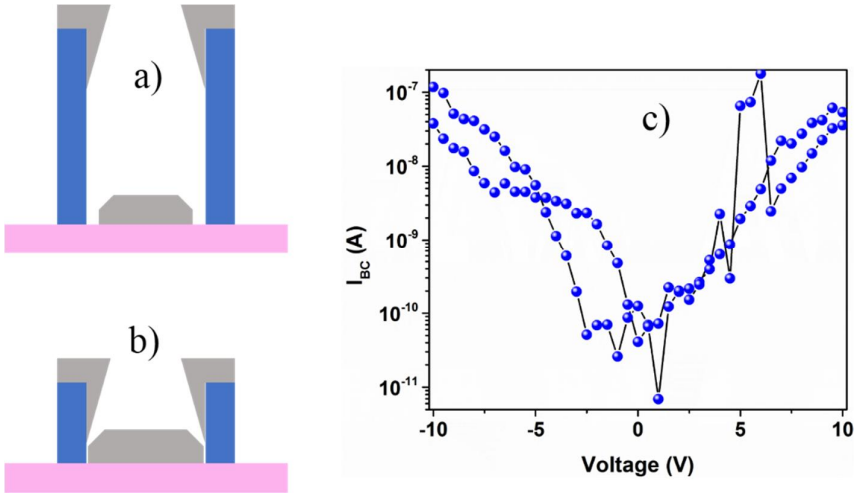

Figure 5.3: a) and b) show aspect ratio dependent aluminum coating, c) I(V) response between Al and ITO electrode prior to filling P3HT in the pores.

Semiconducting p-type polymers such as P3HT and DPP-DTT were used as the active layer, cast either through dip-coating (for AFM measurements) or drop-casting (for transistor measurements) in a N_2-filled glove box from a 20 mg/ml solution in chlorobenzene and annealed at 140˚C for 1 hour to form the active channel inside and above the pores. In effect, the polymer film extends from the collector-bottom of the pore to the emitter (>100 nm above the base electrode), where thermally deposited gold forms the emitter (source-equivalent) electrode, to complete the nano-triode device. An illustration of the side view of the completed device is shown in Figure 5.4. An individual organic nano-triode comprises of a porous metal base forming a Schottky contact, an emitter which forms an injecting ohmic contact and a collector electrode for charge extraction.

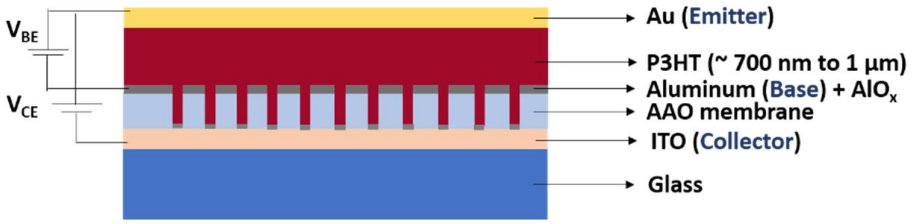

Figure 5.4: Illustration of the side view of the ONTA structure showing the different layers.

5.3 Device Characterization

5.3.1 Experimental Characterization

All measurements were performed in inert atmosphere using a customized device holder chamber. Devices were stored in an inert atmosphere in between measurements.

Current-Voltage Measurements: J(V) characteristics, transistor and diode curves were measured using a Keithley 4200 semiconductor parameter analyzer. Switching measurements were performed by applying a pulsed voltage of ΔV_{BE} = -1 V to the base electrode while maintaining V_{CE} = -2 V. The output voltage was measured across an external series resistor using a Tektronix MDO3024 200 MHz oscilloscope. Time of Flight (TOF) measurements were performed using a 532 nm pulsed excitation from a nanosecond laser, and the output transient was measured using a 50 Ω coupling in the oscilloscope.

Atomic Force Microscopy: Topography and conducting AFM (C-AFM) measurement of the ONTA device was recorded using JPK Nanowizard 3 atomic force microscope. Topography and C-AFM were simultaneously recorded in contact mode using a Si cantilever coated with Cr/Au having resonance frequency of 13 kHz and force constant of 0.2 N/m.

5.3.2 Device Simulations

The mechanism of operation of an ONTA was studied by performing 2D device simulation using Atlas, Silvaco Inc. Organic semiconductor transport properties were used for the simulation by employing the 'Organic Display' module. P3HT properties were incorporated by taking values from literature[29]. An exponential density of states was considered at the band edge to introduce defect energy levels close to the HOMO level as seen in previously reported studies[30,31]. The simulation code along with the material parameters for the different regions of single pore ONTA is given in Appendix B.

5.4 Working Principle of ONTA

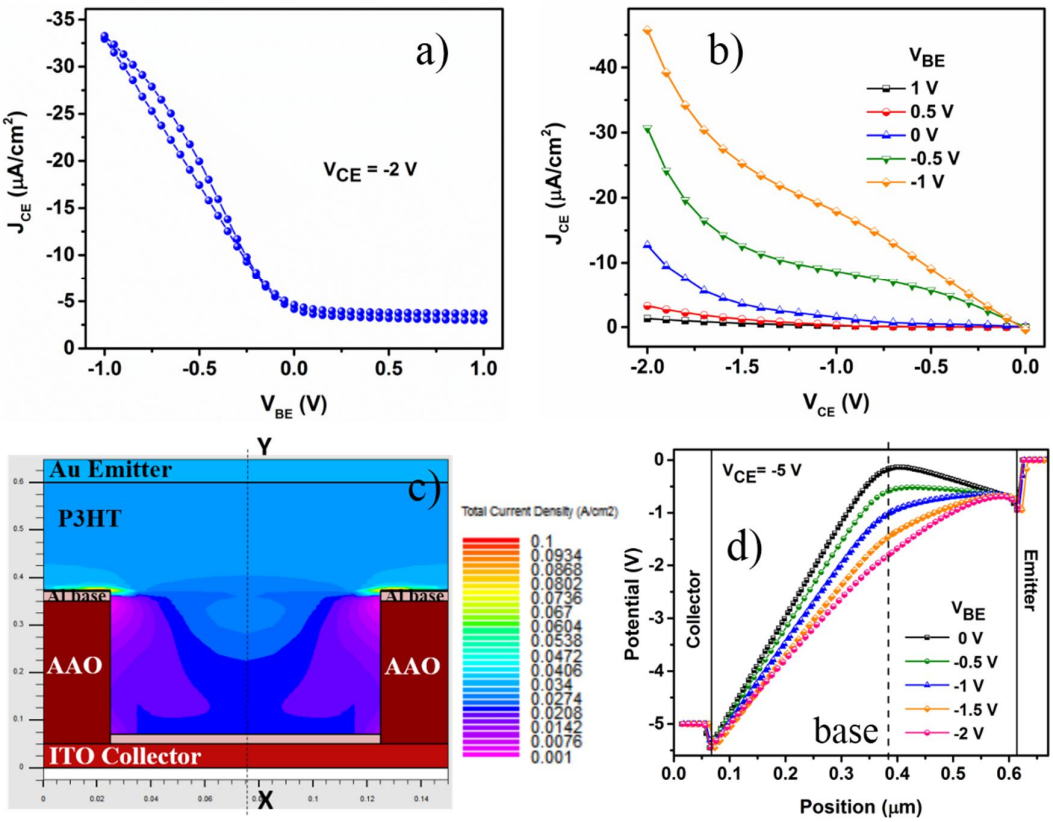

Figure 5.5: a) Transfer, and b) output characteristics of a fabricated ONTA device of area ≈1 mm^2, c) a single pore of the ONTA as simulated in Atlas. 2D current density distribution is shown in the pore, and d) line scan of the simulated potential landscape in the vertical channel of the pore which shows base modulation as the V_{BE} is increased in the forward bias.

Conventional vacuum triodes consist of a p+ base region and an n-channel region for charge transport when a finite forward collector-emitter bias (V_{CE}) is applied at zero base bias. As the base is reverse biased (V_{BE}), a depletion region is created around it. Subsequently, increasing the bias widens the depletion width, pinches off the channel and switches off the transistor[32,33]. One of the features of triode-like VOTs is the realization of normally OFF transistors. V_{CE} causes the flow of collector-emitter current (I_{CE}) through the P3HT in the pore. I_{CE} is primarily space-

charge limited and follows $J = \frac{9}{8}\varepsilon_0\varepsilon_r\mu\frac{V^2_{tot}}{d^3}$ where V_{tot} is the contribution of V_{CE} and V_{BE}. The I_{CE} in the forward bias ON state is higher than the base-emitter current (I_{BE}) due to the thin aluminum oxide blocking layer formed by plasma treatment which lowers the base recombination current. V_{BE} modulates the current in the P3HT as shown in the transfer (Figure 5.5(a)) and output characteristics (Figure 5.5(b)). The drastic reduction in the channel length in an ONTA leads to current densities that are nearly three orders of magnitude higher as compared with conventional P3HT FETs[34].

The mechanism of operation of the ONTA can be explained based on four regimes as shown in Figure 5.6 which is obtained from 2D simulation of a single pore (Figure 5.5(c)) and (d)). In this study, we use a common emitter configuration for the ONTA. In the first case, when V_{BE} = 0 V and V_{CE} = -5 V, I_{BE} is purely diffusion limited since the base and emitter are at equipotential. For a sufficiently thick P3HT layer, the overall current in the channel is low and vertically confined to the center of the pore (Figure 5.6(a)). The second regime of interest is the saturation regime when V_{BE} = -2 V, V_{CE} = -5 V. Since $V_{CE} > V_{BE}$, charges injected at the emitter are transmitted to the collector under a drift of the CE diode bias. In other words, an overall decrease in the barrier height at the base results in a smooth flow of charges towards the collector thereby giving rise to high I_{CE} (Figure 5.6(b)). To ascertain the role of the base in modulating the I_{CE}, we consider a third regime wherein V_{BE} = -2 V, V_{CE} = -1 V. At this bias, the base is at a lower potential than the collector and the BE field lines point toward the base which causes most of the current from the emitter to recombine at the base. As shown in Figure 5.6(c), although there is hole injection at the emitter, recombination at the base is high which ultimately results in low I_{CE}. Finally, we consider the region of complete pinch-off which happens for $V_{BE} \geq 0$ V. When V_{BE} = 1 V, the BE, and CE field lines are anti-parallel, so the possibility of the base rather than the emitter injecting holes is higher. However, the presence of a thin oxide layer around the base prevents any charge injection, therefore, resulting

in an overall reduction in I_{CE} (Figure 5.6(d)). In an organic ONTA, for any $V_{BE} > 0$ V, the channel is pinched off since $V_{BE} > V_{CE}$, implying that the threshold voltage (V_T) should be at/close to $V_{BE} = 0$ V which is seen in the transfer characteristics of the fabricated device in Figure 5.5(a). From the above description, we note that the base electrode is primarily responsible for the transistor-like operation in ONTAs. It has been shown from earlier reported results that V_{tot} in the SCLC equation is a linear combination of V_{CE} and V_{BE} with a geometrical perturbation factor (λ) associated with V_{BE} given by $V_{CE}+\lambda V_{BE}$[35]. Optimizing λ can yield better saturation behavior, lower off currents and high switching speed. We explore the influence of the geometrical parameters of the AAO template like pore diameter, pore height and base electrode thickness on the device characteristics by device simulation, which is consistent with the experimental trend.

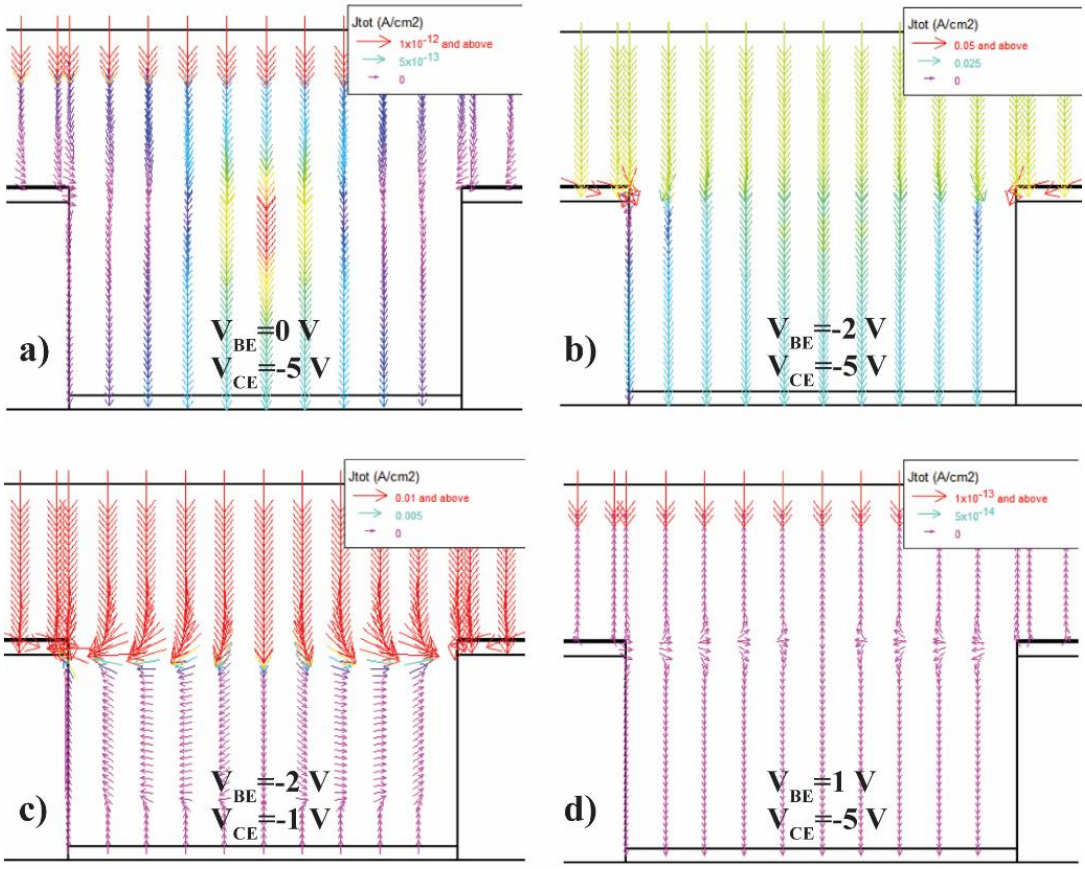

Figure 5.6: Simulated total current density in the active layer of a single organic nano-triode when a) V_{BE} = 0 V and V_{CE} = -5 V, b) V_{BE} = -2 V, V_{CE} = -5 V, c) V_{BE} = -2 V, V_{CE} = -1 V and d) V_{BE} = 1 V, V_{CE} = -5 V explaining different regimes of operation. The pore diameter is kept constant at 100 nm with a total P3HT thickness of 530 nm.

5.5 Optimizing Geometrical Parameters

5.5.1 Pore Width

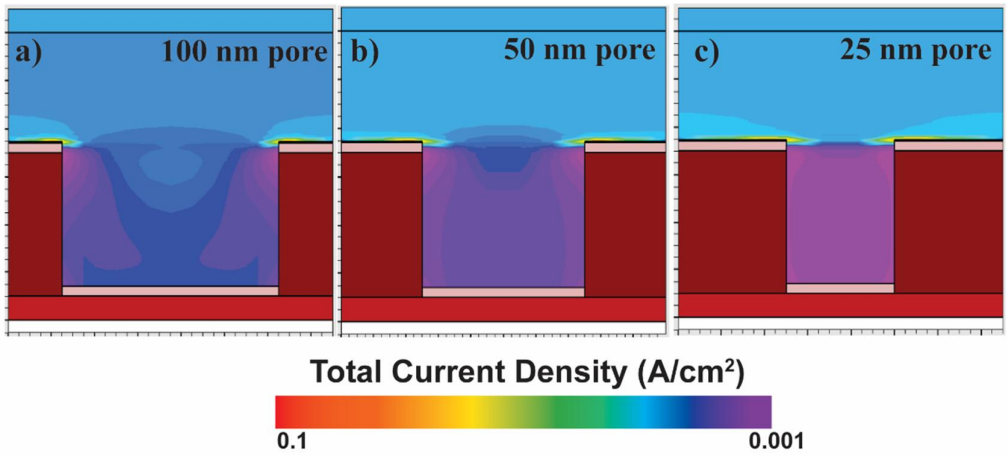

Figure 5.7: a,b,c) Simulated current density contours for three pore diameters at V_{BE}= -2 V, V_{CE}= -5 V.

The first parameter we consider is the AAO pore width. For p-type ONTA operation, at $V_{BE} = 0$ V and $V_{CE} < 0$ V, the channel for I_{CE} is not completely pinched-off, resulting in a small OFF current. A pinch-off voltage is obtained when the energy barrier exceeds the activation energy required for electrons to hop. Apart from the V_{BE}, the barrier height is also a function of the pore diameter. The low-charge density region extends beyond the base along the walls of the AAO and decreases radially. These features of the charge distribution determine the OFF current in the ONTA. As the pore diameter reduces from 100 nm to 25 nm, the low charge density region extends into the entire pore thereby reducing the magnitude of the OFF current (Figure 5.7(a), (b), (c)). However, the reduction in active channel area also reduces

the magnitude of saturation current. We fabricated ONTAs with two pore dimensions and observe that the J_{CE} of a 100 μm^2 device can be varied from 40 $\mu A/cm^2$ to 30 $\mu A/cm^2$ as the pore dimension changes from 100 nm to 50 nm.

5.5.2 Semiconductor Thickness

The second geometrical parameter considered is the thickness of the P3HT layer. In an SCLC diode, the internal electric field is non-uniform and strongly dependent on the thickness of the active layer[36]. The presence of a third electrode further modifies the potential landscape between the CE and BE diodes. The potential distribution can be divided into two regions: the BC potential gradient which varies linearly as a function of V_{CE} and is dependent on the pore depth and pore diameter of the AAO and the BE gradient which is a function of the P3HT layer thickness between the base and the emitter. Since the AAO membrane thickness is fixed, by changing the P3HT thickness between the base and the emitter, the transistor characteristics can be tailored to obtain saturation current. Figure 5.8(a) shows the vertical potential distribution for different P3HT layer thicknesses at a fixed bias. As the P3HT thickness between the BE diode increases, the slope of the BE potential gradient becomes more gradual. The bulk of V_{CE} drops across the BC region implying that as we sweep the V_{CE}, the BC gradient changes but there is negligible contribution from the BE diode. Consequently, a thicker semiconductor yields V_{CE} independent I_{CE} at saturation. A similar condition can be achieved by varying the aspect ratio of AAO to P3HT thickness thereby giving a figure of merit parameter to obtain low OFF currents along with high saturation $I_{CE.}$ The figure of merit parameter has been quantified in previous studies to obtain a high sub-threshold swing which is a crucial parameter for high-frequency switches[37].

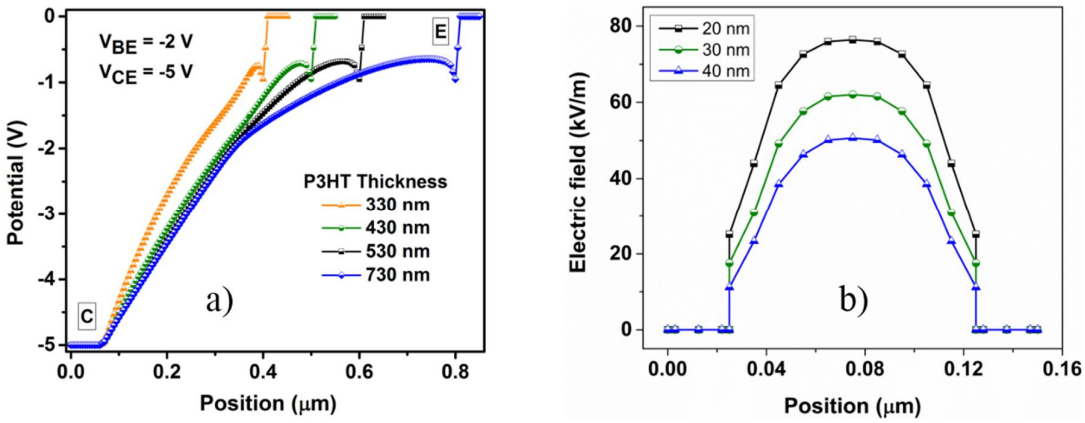

Figure 5.8: a) Simulated vertical potential in the P3HT for varying P3HT thicknesses, and b) base electrode thickness dependence in a 100 nm wide pore ONTA device. The horizontal electric field distribution is obtained at saturation I_{CE}.

5.5.3 Base Electrode Height

The third parameter considered is the effect of the base Al electrode thickness. In an ONTA, the aluminum oxide around the base creates a depletion region in the shape of a cylinder. The depletion capacitance can be subsequently calculated and is found to be inversely proportional to the base metal thickness[38]. Figure 5.8(b) shows the electric field profile for three different thicknesses of the base metal electrode for a pore diameter of 100 nm. As the base thickness increases (20–40 nm), the magnitude of the lateral electric field at the base in the P3HT decreases. As a result, the V_{BE} drift for the incoming holes from the emitter reduces, and the I_{CE} magnitude drops. The decrease in specific depletion capacitance also implies that the BE diode should be reverse biased further (due to leakage currents) to pinch off the channel thereby shifting the threshold voltage to more positive values.

5.6 Switching Characteristics

By implementing the design strategies from the above analyses, we study the applicability of an ONTA fabricated using AAO templates with 100 nm pore diameter and 300 nm AAO thickness for switching circuits. A square voltage pulse is applied

to the base electrode (ΔV_{BE} = -1 V) of the transistor operating in the saturation regime (V_{CE} = -2 V) as shown by a circuit diagram in Figure 5.9(a).

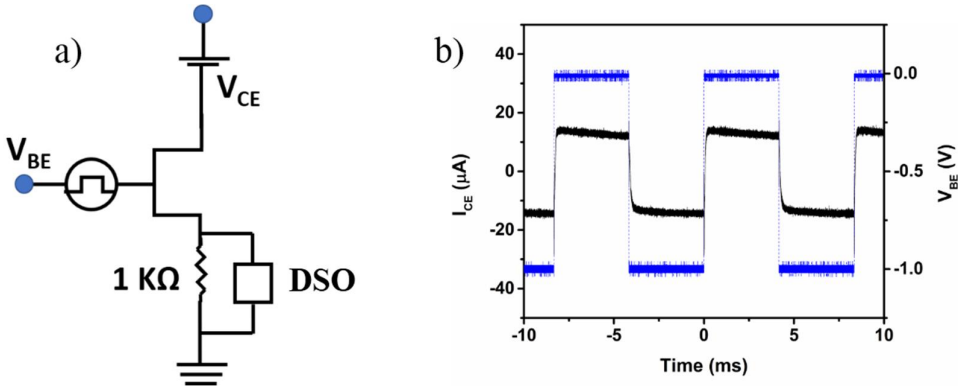

Figure 5.9: Switching characteristics in an ONTA. a) Circuit diagram of the setup used for obtaining switching behavior, and b) output signal for a 120 Hz pulsed V_{BE}= -1 V and V_{CE}= -2 V.

I_{CE} is measured using a linear current to voltage converter (1 kΩ load resistor connected across the CE diode). The response of the ONTA (Figure 5.9(b)) is obtained after correcting for the exponentially decaying background surge current which arises due to capacitance discharge at the emitter electrode. The switching time τ_{switch} which can be subsequently deduced from the rise time of the output signal is observed to be 87.8 μs for a pulse voltage duration of 5 ms. In the ONTA, three time constants need to be considered to determine the τ_{switch}. The first is the RC charging time τ_{RC}, where R is a sum of base resistance and channel resistance and C is the depletion capacitance. Capacitive effects due to the AAO walls (geometrical capacitance) are negligible as is seen from the simulation of barrier materials of different dielectric constant (Figure 5.10(a)) and can, therefore, be neglected. The second factor is the transit time of charge carriers between the emitter and collector. To estimate the transit time of the holes, time of flight (ToF) measurements are performed as a function of V_{CE}, while the V_{BE} is kept constant (typical ToF transient shown in the inset of Figure 5.10(b)). As we can see from Figure 5.10(b), the transit time of charge carriers decreases with increasing V_{CE} by the equation, $\tau_{tr} = d^2 / \mu V$, where d is the channel length and μ is

the space-charge mobility of P3HT. At V_{CE} = -2 V, V_{BE} = -0.5 V, the transit time is ≈1 µs which is of the order of the τ_{switch} of the device. The saturation current which is determined by the thickness of the semiconductor can be controlled at the nanometer level and gives us an accurate handle to tune the transit time. Finally, the dielectric relaxation time (τ_d) needs to be considered. The τ_d is intrinsic to the semiconductor material and is expressed as $\tau_d = \rho\epsilon$ where ε is the dielectric constant of the semiconductor implying that increasing the dielectric constant of the semiconductor can also increase the switching frequency. The role of τ_d on the ONTA performance is studied by fabricating devices based on a high mobility DPP-DTT polymer[3] (Figure 5.10(c)). The higher mobility of DPP-DTT translates to higher channel conductance. As expected, the magnitude of the saturation current in the ONTA increases, however, it is found that the ON-OFF ratio is less due to high channel off currents. From this discussion, it is understood that the above three time constants can be finely tuned by the device geometry and material choice. τ_{RC} can be reduced by maintaining a high aspect ratio of AAO to P3HT thickness and τ_{switch} can be further improved by reducing the charging/parasitic capacitance at the emitter which develops when the barrier height for charge carrier injection is more. Many other factors such as lowering the injection barrier using appropriate buffer layers, improved blocking layers around the base, etc. to name a few can improve the switching frequency further which can parallel the operation limits of inorganic FETs in the near future for next-generation integrated circuit requirements.

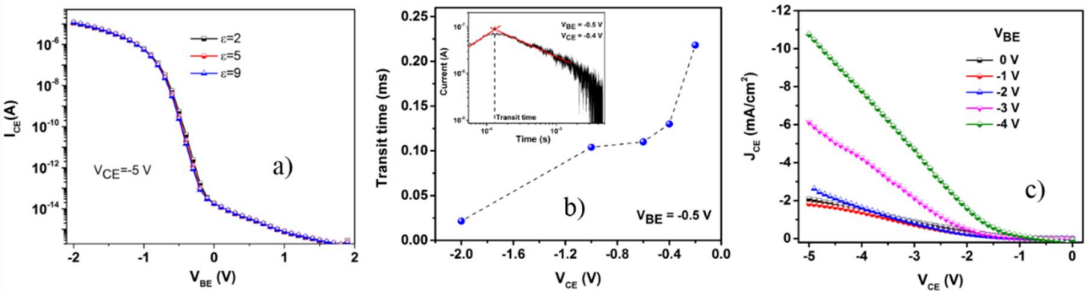

Figure 5.10: a) Transfer characteristics of a single pore for varying dielectric constants of AAO. This shows no contribution of geometrical capacitance to I_{CE}, b)

transit time dependence when V_{CE} is increased keeping V_{BE} constant at -0.5 V. Inset of b) shows a representative ToF signal obtained for 532 nm pulsed laser illumination, and c) output characteristics of an ONTA using high conductivity DPP-DTT polymer as the channel layer. Pore size is 100 nm with center to center pore distance ≈125 nm and thickness of the membrane is 300 nm.

5.7 Up-scaling Device Density

Finally, we emphasize the possibility of 3D integrated circuits at mesoscales by using individual nano-triodes and lateral patterning. We measure the performance of a single pore ONTA and observe current levels well above noise levels. In this pursuit, we also demonstrate the linear scaling of I_{CE} as a function of pore number by emitter electrode patterning. Figure 5.11(a) shows the topography of the porous AAO structure with P3HT filled in the pores recorded using atomic force microscopy. The conducting atomic force microscopy image of the same area is presented in Figure 5.11(b) and Figure 5.11(c) showing the uniformity of current throughout the pore which implies that P3HT completely wets the pore. For a forward V_{CE} = 5 V, a uniform current magnitude is observed in the pore while the AAO region acts as a barrier implying that each pore can perform as an individual device. The patterning of the emitter electrode enables the formation of miniature functional blocks of ONTAs that provide an accurate control on the signal magnitude. Figure 5.11(d) provides evidence for this approach and shows the I_{CE} dependence on emitter area for an ONTA operating at V_{CE} = -2 V, V_{BE} = -0.5 V. A linear relationship between pore density and current can be observed, however, larger device statistics need to be considered to confirm a clear trend.

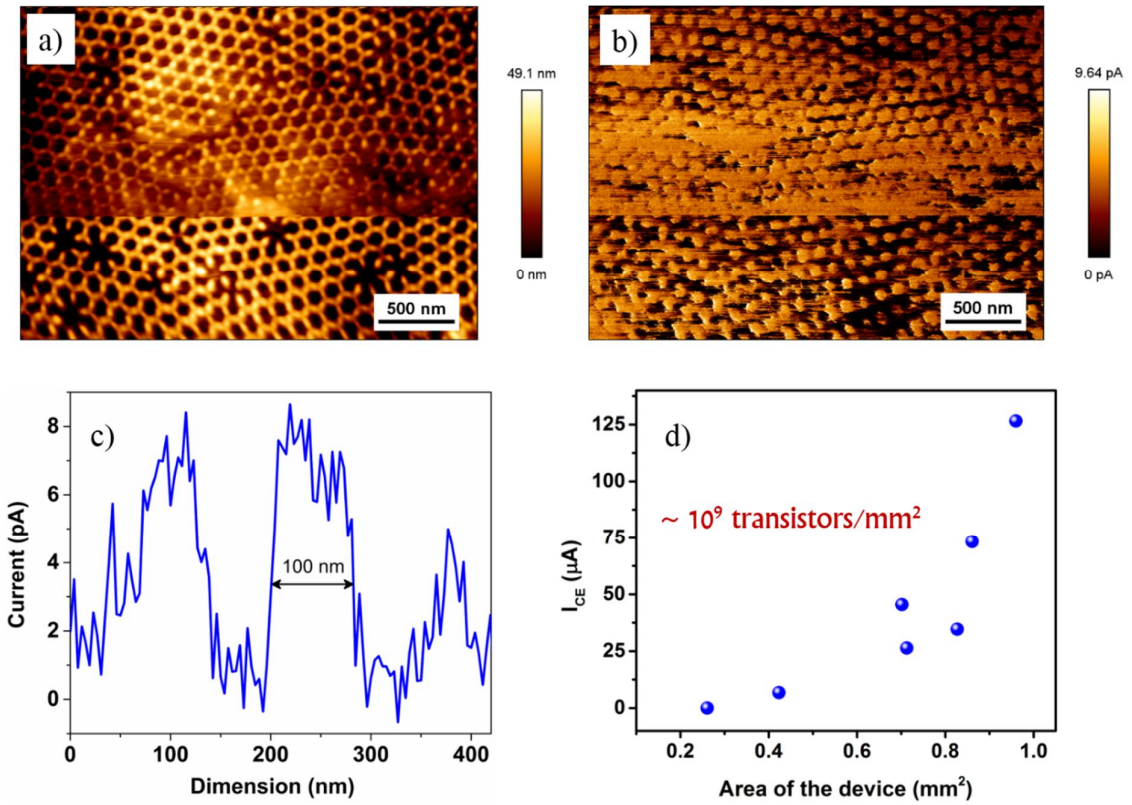

Figure 5.11: a) AFM image of the porous AAO membrane surface, b) Conductive AFM image shows current through the pores whereas the AAO walls act as barriers thereby isolating each pore, c) shows current uniformity in the pore of diameter 100 nm, and d) device density upscaling shown by plotting the I_{CE} in an ONTA as a function of device area for V_{BE}= -0.5 V, V_{CE}= -2 V.

5.8 Summary

In summary, porous alumina membranes provide the desired geometry and systematic quantification of I_{CE} over a large area for a nano-triode array which opens a facile route for device integration coupled with superior device performance. Simulations reveal that the aspect ratio of pore diameter to semiconducting polymer film thickness controls the I_{CE} saturation and OFF-current magnitude (ON-OFF ratio) for switching. It is interesting to note that the performance parameter criteria

of the device do not pose requirement constraints of high-mobility structurally ordered active layer materials. In the present ONTA design, the I_{BC} is nearly six orders lower than I_{CE} due to the presence of the AAO layer which reduces the BC diode contribution. All the salient advantages of an ONTA coupled with the facile fabrication techniques enabled us to test its applicability as a switch with a short rise time ≈ 87.8 μs and stable operation in kHz range.

5.9 References

1 Geier, M. L. *et al.* Solution-processed carbon nanotube thin-film complementary static random access memory. *Nature nanotechnology* **10**, 944-948 (2015).

2 Nathan, A. *et al.* Amorphous silicon thin film transistor circuit integration for organic LED displays on glass and plastic. *IEEE Journal of solid-state circuits* **39**, 1477-1486 (2004).

3 Li, J. *et al.* A stable solution-processed polymer semiconductor with record high-mobility for printed transistors. *Scientific reports* **2** (2012).

4 Klauk, H., Zschieschang, U., Pflaum, J. & Halik, M. Ultralow-power organic complementary circuits. *nature* **445**, 745 (2007).

5 Senanayak, S. P. *et al.* Self-Assembled Nanodielectrics for High-Speed, Low-Voltage Solution-Processed Polymer Logic Circuits. *Advanced Electronic Materials* **1** (2015).

6 Rajaram, S., Shivanna, R., Kandappa, S. K. & Narayan, K. Nonplanar perylene diimides as potential alternatives to fullerenes in organic solar cells. *The journal of physical chemistry letters* **3**, 2405-2408 (2012).

7 Risteska, A., Myny, K., Steudel, S., Nakamura, M. & Knipp, D. Scaling limits of organic digital circuits. *Organic Electronics* **15**, 461-469 (2014).

8 Bürgi, L., Richards, T., Friend, R. & Sirringhaus, H. Close look at charge carrier injection in polymer field-effect transistors. *Journal of Applied Physics* **94**, 6129-6137 (2003).

9 Natali, D. *et al.* Injection length in staggered organic thin film transistors: assessment and implications for device downscaling. *Advanced Electronic Materials* **2** (2016).

10 Chao, Y.-C. *et al.* Polymer hot-carrier transistor with low bandgap emitter. *Applied Physics Letters* **92**, 79 (2008).

11 Cheng, S. S. *et al.* Organic base modulation triodes and their inverters on flexible substrates. *Advanced Materials* **21**, 1860-1864 (2009).

12 Fujimoto, K., Hiroi, T., Kudo, K. & Nakamura, M. High-Performance, Vertical-Type Organic Transistors with Built-In Nanotriode Arrays. *Advanced Materials* **19**, 525-530 (2007).

13 Kwon, H. *et al.* Toward High-Output Organic Vertical Field Effect Transistors: Key Design Parameters. *Advanced Functional Materials* **26**, 6888-6895 (2016).

14 Ma, L. & Yang, Y. Unique architecture and concept for high-performance organic transistors. *Applied physics letters* **85**, 5084-5086 (2004).

15 Parashkov, R. *et al.* Vertical channel all-organic thin-film transistors. *Applied physics letters* **82**, 4579-4580 (2003).

16 Yutani, K., Nakayama, K.-i. & Yokoyama, M. Fabrication of vertical organic field effect transistor at the edge of patterned photoresist. *Molecular Crystals and Liquid Crystals* **444**, 197-202 (2006).

17 Baby, T. T. *et al.* Sub-50 nm Channel Vertical Field-Effect Transistors using Conventional Ink-Jet Printing. *Advanced Materials* **29** (2017).

18 Lüssem, B., Günther, A., Fischer, A., Kasemann, D. & Leo, K. Vertical organic transistors. *Journal of Physics: Condensed Matter* **27**, 443003 (2015).

19 Johnston, D. E., Yager, K. G., Nam, C.-Y., Ocko, B. M. & Black, C. T. One-volt operation of high-current vertical channel polymer semiconductor field-effect transistors. *Nano letters* **12**, 4181-4186 (2012).

20 Ben-Sasson, A. J. *et al.* Patterned electrode vertical field effect transistor fabricated using block copolymer nanotemplates. *Applied Physics Letters* **95**, 302 (2009).

21 Ou, T.-M. *et al.* All-organic hot-carrier triodes with thin-film metal base. *Applied physics letters* **89**, 183508 (2006).

22 Cheng, S.-S. *et al.* Using metal/organic junction engineering to prepare an efficient organic base-modulation triode and its inverter. *Organic Electronics* **10**, 1636-1640 (2009).

23 Ben-Sasson, A. J. & Tessler, N. Patterned electrode vertical field effect transistor: Theory and experiment. *Journal of Applied Physics* **110**, 044501 (2011).

24 Sulka, G. D. Highly ordered anodic porous alumina formation by self-organized anodizing. *Nanostructured materials in electrochemistry* **1**, 1-116 (2008).

25 Li, A. P., Müller, F., Birner, A., Nielsch, K. & Gösele, U. Fabrication and Microstructuring of Hexagonally Ordered Two-Dimensional Nanopore Arrays in Anodic Alumina. *Advanced Materials* **11**, 483-487 (1999).

26 Li, F., Zhang, L. & Metzger, R. M. On the growth of highly ordered pores in anodized aluminum oxide. *Chemistry of materials* **10**, 2470-2480 (1998).

27 Yang, S. M., Jang, S. G., Choi, D. G., Kim, S. & Yu, H. K. Nanomachining by colloidal lithography. *small* **2**, 458-475 (2006).

28 Lee, W. & Park, S.-J. Porous anodic aluminum oxide: anodization and templated synthesis of functional nanostructures. *Chemical reviews* **114**, 7487-7556 (2014).

29 Scheinert, S. & Paasch, G. Interdependence of contact properties and field-and density-dependent mobility in organic field-effect transistors. *Journal of Applied Physics* **105**, 014509 (2009).

30 Tanase, C., Meijer, E., Blom, P. & De Leeuw, D. Unification of the hole transport in polymeric field-effect transistors and light-emitting diodes. *Physical Review Letters* **91**, 216601 (2003).

31 Blom, P. W., De Jong, M. & Vleggaar, J. Electron and hole transport in poly (p-phenylene vinylene) devices. *Applied Physics Letters* **68**, 3308-3310 (1996).

32 Ozawa, O. Electrical properties of a triode-like silicon vertical-channel JFET. *IEEE Transactions on Electron Devices* **27**, 2115-2123 (1980).

33 Shockley, W. A unipolar" field-effect" transistor. *Proceedings of the IRE* **40**, 1365-1376 (1952).

34 Sirringhaus, H., Tessler, N. & Friend, R. H. Integrated optoelectronic devices based on conjugated polymers. *Science* **280**, 1741-1744 (1998).

35 Lin, H.-C., Zan, H.-W., Chao, Y.-C., Chang, M.-Y. & Meng, H.-F. Review of a solution-processed vertical organic transistor as a solid-state vacuum tube. *Semiconductor Science and Technology* **30**, 054003 (2015).

36 Blom, P., De Jong, M. & Van Munster, M. Electric-field and temperature dependence of the hole mobility in poly (p-phenylene vinylene). *Physical Review B* **55**, R656 (1997).

37 Li, C.-H. *et al.* Achieving saturation in vertical organic transistors for organic light-emitting diode driving by nanorod channel geometric control. *Applied Physics Letters* **102**, 74 (2013).

38 Ozawa, O. & Aoki, K. A multi-channel FET with a new diffusion type structure. *Japanese Journal of Applied Physics* **15**, 171 (1976).

Summary and Outlook

Chapter 6

Summary and Outlook

Field-effect transistors are the building block of modern day electronics and research towards improving device performance is a continued goal in this technology. The underlying effort in this thesis was to achieve this in polymer devices by dielectric and device engineering using facile solution techniques and low temperature processing for scalable applications. Experimental methods of enhancing performance parameters of polymer transistors such as increasing switching speed, reducing the threshold voltage and power consumption and up-scaling device density were presented. An optical sensor utilizing a PFET with the improved characteristics was also demonstrated. Device simulations proved to be a useful tool to complement the results obtained for novel device architectures.

The possibility of low turn on voltage and low-power operation of OFETs opens of variety of sensor applications. The first outcome of the thesis was to achieve this goal by two dielectric engineering strategies. Firstly, an ultra-thin hybrid dielectric film was fabricated using a solution processed oxide layer (high-k) followed by a dense monolayer of a surfactant (low-k) which was formed by self-assembly. The monolayer reduced leakage in the dielectric without lowering the effective dielectric constant ($\varepsilon' \approx 11$) which resulted in a low-loss, high specific capacitance of 0.3 $\mu F/cm^2$ and PFETs fabricated using the hybrid dielectric operated under -2 V. In the second strategy, a new molecular dielectric TBD was utilized as a single step, solution processable dielectric layer for PFETs. The dielectric properties of a thin film of TBD revealed an $\varepsilon' \approx 6$ which lies in the mid-k region. Capacitors using TBD as the dielectric also exhibited a low loss tangent with a small dipolar relaxation time and low interfacial disorder. Under - 5 V operation was achieved in p-type PFETs with a mobility of 0.1 $cm^2/V.s$ using DPP-DTT as the active material layer. We also observed that when TBD is added in small concentrations in a P(VDF:TrFE) matrix, thin films exhibited enhanced ferroelectric properties. AFM, XRD and dielectric spectroscopy studies suggested improved packing of the P(VDF:TrFE) chains which resulted in

higher dipolar orientation in the presence of an external field. Simultaneously, capacitors utilizing the composite as the dielectric layer revealed a marginal increase in the effective dielectric constant ($\varepsilon' \approx 8$) and decrease in dielectric loss as compared to pristine TBD films. PFETs fabricated from the composite dielectric show one order higher mobility as compared to pristine P(VDF-TrFE) because of lowered interfacial disorder and dielectric loss.

In the following chapter, a functional circuit consisting of an OPD connected in series with the low voltage PFET was fabricated to study the PFET applicability in a pixel addressable optical sensor. A reasonable light dependence of up to four orders of incident power and a minimum sensitivity of 10 $\mu W/cm^2$ was obtained from photoresponse measurements of the integrated PFET-OPD structure and the output characteristics showed thickness and structure dependence. By utilizing the strongpoint of solution and low temperature processing of organic devices, a novel monolithic pixel architecture was also realized and studied for its photoresponse.

In the subsequent chapter, strategies to increase switching speed and device density and reduce operating voltage were studied by utilizing a vertical transistor architecture. A mesoporous alumina template was obtained and transistors were fabricated within each pore. Analogous to the vacuum triode structure, the P3HT based vertical transistor exhibited saturation current densities of the order of mA/cm^2 and an operating voltage of -2 V. An array of such transistors was feasible due to the ordered template structure and a device density of up to 10^9 transistors/mm^2 was achieved. This study was supported by device simulations which helped in identifying the key structural parameters to optimize the performance of the nano-triode array.

In summary, three main aspects of organic devices, specifically PFETs, were considered in this thesis to enhance device functionality. They were: reducing device power consumption, improving PFET mobility and increasing device density. As an immediate confirmation of device applicability, reliability tests are utmost important. Simultaneously, scalability techniques must be explored to implement solution

processing functional circuits for flexible and roll-to-roll applications. Detailed studies of the degradation and reliability of organic electronic devices also must be studied to increase their life-time and enable them as an emerging technology option.

In terms of practical device applications, the passive pixel sensor can be extended to an active matrix circuit to be utilized in image sensors and to drive display units. PFETs designed from the ultra-thin dielectrics can also be utilized for bio-sensing and mapping cellular potential which will pave the way for novel applications, generally believed to be unachievable with silicon electronics.

The porous alumina membrane provides an ordered template to study confinement induced transport phenomena in semiconducting polymers/ small molecule materials. Pore size dependent conductivity and photoresponse of semi-crystalline and amorphous polymers can reveal the mechanism prevailing in electrical charge transport in disordered systems

Appendices

Appendix A

A Self-Assembled Image Sensor Pixel Device Simulation

```
go atlas
title image sensor pixel characteristics

# ***********mesh definition**********

mesh width=1000

x.mesh location=0  spacing=1
x.mesh location=20  spacing=1
x.mesh location=60  spacing=1
x.mesh location=80  spacing=1

y.m l=-0.05 s=-0.025
y.m l=0 s=0.001
y.m l=0.02 s=0.001
y.m l=0.04 s=0.01
y.m l=0.07 s=0.01
y.m l=0.27 s=0.1
y.m l=0.30 s=0.1

# ***********region definition**********

region num=1 material=Hfo2 x.min=0 x.max=80 y.min=0 y.max=0.02
region  num=2  user.material=dpp  x.min=0  x.max=80  y.min=0.02
y.max=0.07
region  num=3  user.material=bhj  x.min=0  x.max=80  y.min=0.07
y.max=0.27
region  num=4  material=vacuum  x.min=0  x.max=20  y.min=-0.05
y.max=0
region  num=4  material=vacuum  x.min=60  x.max=80  y.min=-0.05
y.max=0
region  num=4  material=vacuum  x.min=20  x.max=80  y.min=0.27
y.max=0.30

# ***********electrode definition**********

electrode    num=1 name=gate   x.min=20   x.max=60   y.min=-0.05
y.max=0  material=aluminum
electrode    num=2 name=drain   x.min=0   x.max=20   y.min=0.02
y.max=0.04  material=gold
electrode    num=3 name=source  x.min=60  x.max=80  y.min=0.02
y.max=0.04  material=gold
electrode    num=4 name=cathode  x.min=0  x.max=20  y.min=0.27
y.max=0.30  material=aluminum
```

```
#*********contact definition*********

contact name=gate workfunc=4.1
contact name=source workfunction=5.2
contact name=drain workfunction=5.2
contact name=cathode workfunc=4.1

# We assign a resistivity to the aluminum and gold using the
RESISTIVITY
# parameter of the MATERIAL statement.

material material=aluminum      resistivity=1e-5
material material=gold   resistivity=1e-4

# ***********saving structure file**********

save outf=fet.str
tonyplot fet.str

#********parameters for all the regions********

material material=Hfo2 permittivity=22.0
material         material=dpp         user.group=semiconductor
user.default=organic   eg300=1.7   affinity=3.5   nc300=2.5e19
nv300=2.5e19 permittivity=3.0
#material         material=bhj         user.group=semiconductor
user.default=organic   eg300=1.1   affinity=4.0   nc300=2.5e19
nv300=2.5e19 permittivity=3.0


#************Bimolecular recombination and poole-frenkel
#parameters*********

material material=bhj knrs.exciton=1.82694e6 lds.exciton=0.01
taus.exciton=1.0e20 rst.exciton=1.0
material material=bhj a.singlet=1.32167 s.binding=0.28484
mobility   material=bhj   deltaen.pfmob=0.1   deltaep.pfmob=0.1
betan.pfmob=4e-4 betap.pfmob=4e-4 mun0=2.5e-3 mup0=3.0e-4

material material=dpp knrs.exciton=1.82694e6 lds.exciton=0.01
taus.exciton=1.0e20 rst.exciton=1.0
material material=dpp a.singlet=1.32167 s.binding=0.28484
mobility   material=dpp   deltaen.pfmob=0.1   deltaep.pfmob=0.1
betan.pfmob=4e-4 betap.pfmob=4e-4 mun0=1e-5 mup0=0.1

#**********dissociation parameters*********

material material=bhj qe.exciton=1

#************parameters for light source**********
```

```
material material=aluminum sopra=Al.nk
material material=bhj real.index=2.05 imag.index=0.49
material material=gold sopra=Au.nk
material material=dpp real.index=2.02 imag.index=0.84
material material=Hfo2 sopra=Hfo2.nk
material material=vacuum real.index=1 imag.index=0.1

#********defects statement**********

odefects  ha=1e18  hd=1e18  tcd=600  sigae=1e-14  sigah=1e-14
sigde=1e-14 sigdh=1e-14 numa=64 numd=128 \
         dfile=oddon.dat afile=odacc.dat

#********models statement********

models pfmob singlet langevin s.dissoc


#**********measure the characteristics**********

# First measure dark FET characteristics

method  newton trap
solve init
solve previous

# Un-Saturated D.C. IV Characteristics

solve vdrain=-0.02
solve vdrain=-0.1
log outfile=fet_1.log
solve vgate=1 vstep=-0.1 vfinal=-3 name=gate
log off

# Saturated D.C. IV Characteristics

solve init
solve previous
solve vdrain=-0.1
solve vdrain=-1.0
solve vdrain=-3.0
log outfile=fet_2.log
solve vgate=1 vstep=-0.1 vfinal=-3.0 name=gate

log off

# Save structure - in dark

save outf=fet.str
tonyplot fet.str
```

```
# Plot PFET Characteristics

tonyplot -overlay fet_1.log fet_2.log

# transient with green light

beam num=1 x.origin=10 y.origin=-1.0 min.window=0 max.window=20
angle=90 wavelength=0.532

method newton trap
solve init
solve prev

# Set vd to vdd

solve vdrain=-0.01
solve vdrain=-0.5
solve vdrain=-1.0
#solve vdrain=-2.0

# Float the drain

contact name=drain current

# Shine light

log outfile=light_opd.log
solve b1=0.001 ramp.lit ramptime=1e-6 dt=1e-7 tstop=49e-6

# Save structure - integration time t=0

save outfile=light_opd1.str
tonyplot light_opd1.str
solve b1=0 ramp.lit ramptime=1e-6 dt=1e-7 tstop=54e-6

# Save structure - end of integration time

save outfile=light_opd2.str
tonyplot light_opd2.str
tonyplot light_opd.log

# Transfer the charge to fet

solve vgate=-3 ramptime=1e-6 tstep=1e-7 tstop=80e-6

# Save structure - start of sampling time

save outfile=opd_fet1.str
tonyplot opd_fet1.str
solve vgate=0 ramptime=1e-6 tstep=1e-7 tstop=100e-6
```

```
# Save structure - end of sampling time

save outfile=opd_fet2.str
tonyplot opd_fet2.str
tonyplot light_opd.log

quit
```

Appendix B

Single Alumina Pore Nano-Triode Device Simulation

```
go atlas
title vertical transistor characteristics

#*****mesh definition*****

mesh width=0.025

x.mesh location=0 spacing=0.01
x.m l=0.003 s=0.01
x.m l=0.022 s=0.01
x.m l=0.025 s=0.01
x.m l=0.125 s=0.01
x.m l=0.128 s=0.01
x.m l=0.147 s=0.01
x.m l=0.15 s=0.01

y.m l=0 s=0.01
y.m l=0.05 s=0.01
y.m l=0.07 s=0.01
y.m l=0.35 s=0.01
y.m l=0.37 s=0.01
y.m l=0.374 s=0.01
y.m l=0.60 s=0.01
y.m l=0.65 s=0.01

#*****region definition*****

region num=1 x.min=0 x.max=0.025 y.min=0.05 y.max=0.35
material=al2o3
region num=2 x.min=0.025 x.max=0.125 y.min=0.07 y.max=0.374
user.material=P3HT
region num=1 x.min=0.125 x.max=0.15 y.min=0.05 y.max=0.35
material=al2o3
region num=1 x.min=0 x.max=0.025 y.min=0.37 y.max=0.374
material=al2o3

region num=1 x.min=0.125 x.max=0.15 y.min=0.37 y.max=0.374
material=al2o3
region num=2 x.min=0 x.max=0.15 y.min=0.374 y.max=0.6
user.material=P3HT

#*****electrode definition*****

electrode num=1 name=collector x.min=0 x.max=0.15 y.min=0
y.max=0.05 material=ito
electrode num=2 name=collector x.min=0.025 x.max=0.125
```

```
y.min=0.05 y.max=0.07 material=aluminum
electrode num=3 name=base x.min=0 x.max=0.025 y.min=0.35
y.max=0.37 material=aluminum
electrode num=3 name=base x.min=0.125 x.max=0.15 y.min=0.35
y.max=0.37 material=aluminum
electrode num=4 name=emitter x.min=0 x.max=0.15 y.min=0.60
y.max=0.65 material=gold

#*****contact definition*****

contact name=base workfunction=4.0
contact name=emitter workfunction=5.2
contact name=collector workfunction=4.2

#*****physical models*****

models pfmob print

#*****material specifications*****

material material=p3ht user.group=semiconductor
user.default=organic eg300=1.9 affinity=3.3 nc300=1e21
nv300=1e21 permittivity=3.3
material material=al2o3 permittivity=9.0
mobility material=p3ht deltaep.pfmob=0.1 betap.pfmob=4e-4
mup0=1e-3

#*****defects statement*****

odefects ha=1e18 hd=1e18 tcd=600 sigae=1e-14 sigah=1e-14
sigde=1e-14 sigdh=1e-14 \
        dfile=oddon.dat afile=odacc.dat

#*****mathematical methods*****

method carriers=1 holes

# Transfer characteristics

#*****solve parameters*****

solve init
solve prev

solve vemitter=0
solve vcollector=0 outf=tc_tmp1
solve vcollector=-1 outf=tc_tmp2
solve vcollector=-2 outf=tc_tmp3
solve vcollector=-3 outf=tc_tmp4
solve vcollector=-5 outf=tc_tmp5
```

```
#load in temporary files and ramp Vds

load infile=tc_tmp1
log outf=tc_0.log
solve vbase=2 vfinal=-2 vstep=-0.1 name=base
output e.field j.electron j.hole j.total
save outf=pore_100_tc_0.str

load infile=tc_tmp2
log outf=tc_0.5.log
solve vbase=2 vfinal=-2 vstep=-0.1 name=base
output e.field j.electron j.hole j.total
save outf=pore_100_tc_0.5.str

load infile=tc_tmp3
log outf=tc_1.log
solve vbase=2 vfinal=-2 vstep=-0.1 name=base
output e.field j.electron j.hole j.total
save outf=pore_100_tc_1.str

load infile=tc_tmp4
log outf=tc_1.5.log
solve vbase=2 vfinal=-2 vstep=-0.1 name=base
output e.field j.electron j.hole j.total
save outf=pore_100_tc_1.5.str

load infile=tc_tmp5
log outf=tc_2.log
solve vbase=2 vfinal=-2 vstep=-0.1 name=base

output e.field j.electron j.hole j.total
save outf=pore_100_tc_2.str
tonyplot pore_100_tc_2.str

#*****plot parameters*****

tonyplot  -overlay   tc_0.log  tc_0.5.log  tc_1.log  tc_1.5.log
tc_2.log

log off

# Output characteristics

#*****solve parameters*****

solve init
solve prev

solve vemitter=0

solve vbase=0 outf=oc_tmp1
```

```
solve vbase=-0.5 outf=oc_tmp2
solve vbase=-1 outf=oc_tmp3
solve vbase=-1.5 outf=oc_tmp4
solve vbase=-2 outf=oc_tmp5

probe name=potential x=0.04 y=0.085 potential

#load in temporary files and ramp Vds

load infile=oc_tmp1
log outf=oc_0.log
solve vcollector=0 vfinal=-5 vstep=-0.25 name=collector

output e.field j.electron j.hole j.total
save outf=pore_100_oc0.str

load infile=oc_tmp2
log outf=oc_0.5.log
solve vcollector=0 vfinal=-5 vstep=-0.25 name=collector

output e.field j.electron j.hole j.total
save outf=pore_100_oc0.5.str

load infile=oc_tmp3
log outf=oc_1.log
solve vcollector=0 vfinal=-5 vstep=-0.25 name=collector

output e.field j.electron j.hole j.total
save outf=pore_100_oc1.str

load infile=oc_tmp4
log outf=oc_1.5.log
solve vcollector=0 vfinal=-5 vstep=-0.25 name=collector

output e.field j.electron j.hole j.total
save outf=pore_100_oc1.5.str

load infile=oc_tmp5
log outf=oc_2.log
solve vcollector=0 vfinal=-5 vstep=-0.25 name=collector

#*****plot parameters*****

output e.field j.electron j.hole j.total
save outf=pore_100_oc2.str
tonyplot pore_100_oc2.str

tonyplot -overlay oc_0.log oc_0.5.log oc_1.log oc_1.5.log
oc_2.log

quit
```